

**Measurement of the vector boson
fusion production Higgs boson fiducial
cross-section observed in the
 $WW^* \rightarrow \ell\nu\ell\nu$ decay channel with the
ATLAS detector**

A Dissertation

Presented to
The Faculty of the Graduate School of Arts and Sciences
Brandeis University
Department of Physics
Professor Gabriella Sciolla, Advisor

In Partial Fulfillment
of the Requirements for the Degree
Doctor of Philosophy

by

Laura Bergsten

June, 2020

This dissertation, directed and approved by Laura Bergsten's committee, has been accepted and approved by the Graduate Faculty of Brandeis University in partial fulfillment of the requirements for the degree of:

DOCTOR OF PHILOSOPHY

Eric Chasalow, Dean of Arts and Sciences

Dissertation Committee:

Professor Gabriella Sciolla, Chair

Craig Blocker

Alessandro Tricoli

©Copyright by

Laura Bergsten

2020

Abstract

Measurement of the vector boson fusion production Higgs boson fiducial cross-section observed in the $WW^* \rightarrow \ell\nu\ell\nu$ decay channel with the ATLAS detector

A dissertation presented to the Faculty of
the Graduate School of Arts and Sciences of
Brandeis University, Waltham, Massachusetts

by Laura Bergsten

The Standard Model vector boson fusion Higgs boson fiducial cross-section is measured in the $H \rightarrow WW^* \rightarrow \ell\nu\ell\nu$ decay channel using 139 fb^{-1} of proton-proton collisions. Collisions from the Large Hadron Collider at $\sqrt{s} = 13 \text{ TeV}$ are recorded by the ATLAS detector. The fiducial cross-section measured to be --- .

Contents

Abstract	v
1 Introduction	1
2 Theory	3
2.1 Standard Model	3
2.2 LHC Physics/Phenomenology	19
2.3 Brief history of SM tests	26
2.4 Measurement motivation	31
3 The LHC and the ATLAS detector	33
3.1 ATLAS	36
3.2 The High-Luminosity LHC and Inner Tracker	38
4 Reconstruction of Physics Objects	40
4.1 Tracking	41
4.2 Electrons	42
4.3 Muons	46
4.4 Jets	56
4.5 Missing transverse energy	60
5 Event Selection	65
5.1 Data and Monte Carlo samples	65
5.2 Object definitions	68
5.3 Common Observables	73
5.4 Event selection	75
6 Backgrounds and Systematics	88
6.1 Backgrounds	88
6.2 Systematic uncertainties	118

CONTENTS

7	Results	130
7.1	Statistical analysis	130
7.2	Fiducial and inclusive cross sections	141
7.3	Differential cross-section measurements	145
7.4	Future results and measurements	147
8	Conclusions	150
A	Inner Tracker	163

Chapter 1

Introduction

The Standard Model describes particles and their interactions at fundamental scales and provides the theoretical tools to test the limits of that knowledge. No significant deviation has thus far been observed between Standard Model predictions and experimental results, but the search continues. Our observable universe shows evidence of physics beyond the current theory, and the search for evidence of what this new physics might be motivates continued measurements of Standard Model parameters. Chapter 2 describes the theoretical motivations for this thesis and the key experimental results that precede it.

The ATLAS detector precisely measures a wide-range of Standard Model parameters. Chapter 3 summarizes the design and performance of the ATLAS detector. This thesis uses prescriptions for reconstruction, identification, isolation and measurements of efficiency and scale from a number of dedicated ATLAS performance groups. Chapter 4 discusses methodology for these recommendations and their particular use in the final state of our measured decay mode.

This thesis focuses on the fiducial cross-section of vector boson fusion Higgs bosons in the WW^* decay channel. This decay channel has a final state that requires accurate recon-

CHAPTER 1. INTRODUCTION

struction of leptons and jets within the detector and greatly benefits from increased statistics available from the latest data. Chapter 5 summarizes the dataset, simulations and observables used in the cross-section measurement as well as the signal event selection. Chapter 6 describes each major background and uncertainty that affects the final measurement, and Chapter 7 details the statistical analysis and final results.

The $H \rightarrow WW^* \rightarrow \ell\nu\ell\nu$ cross-section measurement is the cornerstone of this thesis and has been my primary focus for the past two years. I also had the opportunity to work on detector upgrades and muon performance studies during my Ph.D. studies so these topics are described with particular attention in Chapters 3 and 4.

All measurements and studies included here were made possible through the advice and software programs from countless others. All figures contained in this thesis are cited from either publications or individuals unless I was the direct author.

Chapter 2

Theory

The measurement at the heart of this thesis can only be understood within the context of a vast amount of preceding theoretical and experimental work. I have tried to condense and summarize key concepts that will motivate the central measurement's strategy and results. This chapter begins with a brief summary of the Standard Model itself, first describing fundamental particles and their forces before delving into a succinct mathematical formulation. Next, the chapter discusses the history of the Standard Model and crucial tests of the theory up until current work at the Large Hadron Collider (LHC). The next section outlines some of the recent physics analyses at the LHC with a focus on Higgs boson measurements. Finally, I introduce my thesis' main focus, fiducial cross-section measurements of VBF Higgs bosons decaying into two W -bosons.

2.1 Standard Model

The Standard Model (SM) is one of the most successful scientific theories to date. Its predictions encompass all of the visible universe and continue to undergo careful testing.

CHAPTER 2. THEORY

The SM combines three forces—electromagnetic, weak, and strong—but it is not complete. One known force, gravity, is not included in the Standard Model and further questions, like dark matter and dark energy, remain.

2.1.1 Particles and forces

The particles we define in high energy physics are the most minute portions of observable matter. They are generally considered point-like, have no internal structure, and cannot be further split. Each particle we can define has a unique set of quantum numbers and its own anti-particle (with the same mass and spin, but opposite electrical charge and quantum numbers).

Particles can be sorted into two distinct groups: bosons, with integer spin, and fermions, with half-integer spin. Bosons are ‘force carriers’ meaning they are exchanged any time particles interact. Fermions are at the heart of all conventional matter and can be split further into two categories, leptons and quarks. Quarks have fractional charge (in units of the proton’s charge) and interact strongly, while leptons have integer charge and interact solely through the weak or electromagnetic forces. Both quarks and leptons are made of three generations of particles, each heavier than the previous. Charts showing quark/lepton families and their key quantum numbers are shown below in Figure 2.1. Each generation of quarks and leptons contains a particle doublet. Each lepton doublet contains a charged lepton and a neutrino while each quark doublet contains one $+2/3$ charged particle and one with a $-1/3$ charge. Each lepton and quark also has an anti-particle. All conventional, stable matter is made from the first generation of quarks and leptons.

There are four gauge bosons and one scalar boson predicted through the Standard Model. These correspond to three fundamental forces in nature (the fourth, gravity, is so small on the

CHAPTER 2. THEORY

scale of particle interactions as to not be considered). The strongest force on the subatomic scale works primarily to bind quarks together to form composite particles like protons or neutrons. The electromagnetic force is mediated by the photon. This force accounts for all electric interactions like that between an electron and an atomic nucleus. Finally, the weak force is mediated by exchange of massive W and Z bosons. The β -decay of nuclei (mediated by W bosons) is a weak interaction process. The final boson predicted by the Standard Model is the Higgs boson. The only scalar boson, it has no charge or intrinsic spin. The Higgs gives mass to all other particles through Spontaneous Symmetry Breaking, which will be described in later sections.

Standard Model of Elementary Particles

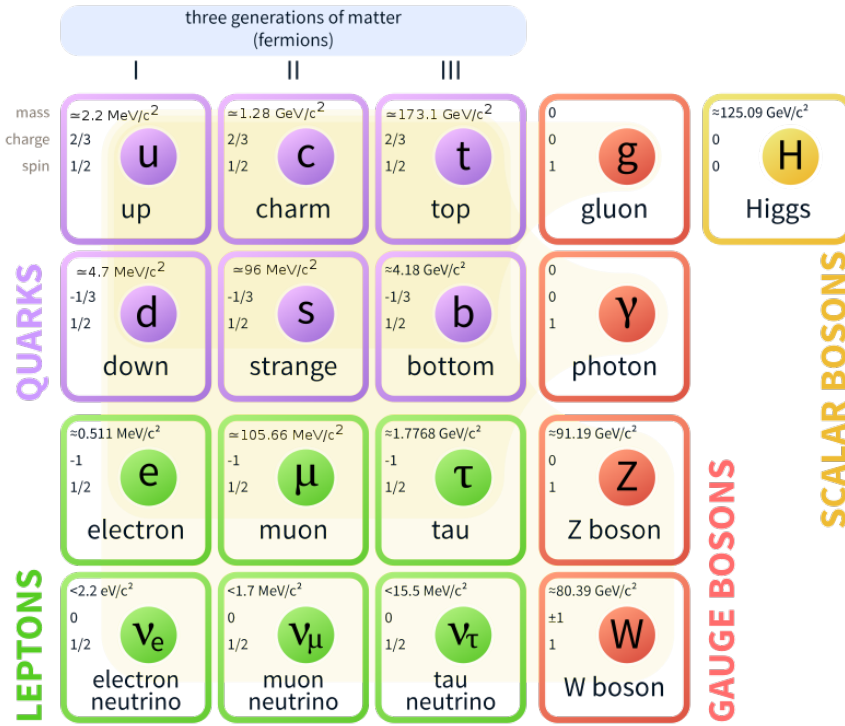


Figure 2.1: Three generations of quarks and leptons are shown along with all SM bosons [1]

Photons are massless, spin-1 particles and mediate all electromagnetic interactions. They

CHAPTER 2. THEORY

couple directly to any particle with electric charge, leptons and W bosons but not neutrinos. Since the photon is massless, the electromagnetic force can operate on infinitely long scales but its force decreases with $1/r^2$.

Gluons are massless particles with no electric charge and spin-1. They couple to color charges, which are a property only of quarks and gluons. Each quark has one of three colors (RGB). Colors are conserved ‘charges’ similar to electric charge. Quarks are never found alone as they couple so strongly to one another as to be confined in groups. These groups are “color-confined” meaning the quarks contain colors which add up to a color neutral sum. Gluons also have color charge and can thus couple to each other. This makes the strong force distinct from the electromagnetic and has implications for long-distance interactions.

The W and Z bosons, unlike gluons and photons, are massive. However, like their other gauge boson counterparts, they have spin-1 and mediate interactions. The W^\pm mediates charged-current interactions which can violate flavor conservation between quarks and/or leptons and their neutrinos. The Z mediates neutral-current interactions which conserve flavor. The W^\pm bosons contain electric charge so can interact through EM interactions, as well. In addition, W and Z bosons contain weak charge (as do all fermions) so can self-couple as well as couple with all fermions.

The Higgs boson will be further motivated and described in later sections but suffice to say it is a massive, spin-0 particle which couples to all particles with mass (including itself). It does not mediate any force but it is still an integral part of the Standard Model.

2.1.2 Gauge Invariance

According to Noether’s theorem, for every continuous transformation of a field that leaves the Lagrangian invariant, there is a conserved current. In other words, symmetries found

CHAPTER 2. THEORY

in physical theories lead to conservation laws (and vice-versa). The Standard Model is a gauge theory built on symmetries; all interactions between particles result from requiring the theory to be invariant under local gauge transformations. Each part of the Standard Model, from quantum electrodynamics (QED) to quantum chromodynamics (QCD), is a gauge theory on its own. Each part has gauge invariance symmetries. In this section I step through the basic mathematic formalism for QED, QCD, and the combined electro-weak theory to illustrate the physical ramifications of gauge invariance and set the stage for the Higgs mechanism. The following sections are written with guidance from [2].

Quantum Electrodynamics

Quantum electrodynamics (QED) is the first, and simplest, physical gauge theory, describing how light and matter interact even under relativistic conditions. The theory produces extremely good agreement with experiment due to the success of perturbative QED calculations. Entire textbooks are dedicated to QED formalism and predictions. Here I will highlight only the effects of its local gauge invariance symmetry and generating the full QED Lagrangian beginning with the Dirac Lagrangian of a free fermion.

The Dirac Lagrangian describes a free fermion of mass m

$$\mathcal{L} = i\psi\gamma^\mu\partial_\mu\psi - m\bar{\psi}\psi, \quad (2.1)$$

where ψ is a Dirac spinor and γ^μ represent the Dirac matrices. To demonstrate local gauge invariance we need to transform

$$\psi(x) \rightarrow e^{i\alpha(x)}\psi(x), \quad (2.2)$$

where $\alpha(x)$ depends on space and time arbitrarily. Directly substituting this into our La-

CHAPTER 2. THEORY

grangian shows that \mathcal{L} is not invariant, due to the ∂_μ term

$$\partial_\mu \psi \rightarrow e^{i\alpha(x)} \partial_\mu \psi + ie^{i\alpha(x)} \partial_\mu \alpha. \quad (2.3)$$

In order to mandate the theory is invariant we need to change this term to the “covariant derivative” D_μ which transforms

$$D_\mu \psi \rightarrow e^{i\alpha(x)} D_\mu \psi. \quad (2.4)$$

The “covariant derviative” must contain a vector field A_μ and this field must transform so as to cancel with the unwanted part of the transformed D_μ in order to transform as required by gauge invariance.

$$D_\mu \equiv \partial_\mu - ieA_\mu \quad (2.5)$$

where

$$A_\mu \rightarrow A_\mu + \frac{1}{e} \partial_\mu \alpha. \quad (2.6)$$

Now the original Dirac equation is replaced with the following:

$$\mathcal{L} = \bar{\psi}(i\gamma^\mu \partial_\mu - m)\psi + e\bar{\psi}\gamma^\mu \psi A_\mu. \quad (2.7)$$

By requiring local gauge invariance we have introduced a gauge field A_μ which couples to the Dirac particle just as the photon. In fact, if we take this as the photon gauge field and so add a kinetic energy term (which is also local gauge invariant!) we find the Lagrangian of QED:

$$\mathcal{L} = \bar{\psi}(i\gamma^\mu \partial_\mu - m)\psi + e\bar{\psi}\gamma^\mu \psi A_\mu - \frac{1}{4}F_{\mu\nu}F^{\mu\nu}. \quad (2.8)$$

One can also see that adding a mass term to the Lagrangian for the new field ($\frac{1}{2}m^2 A_\mu A^\mu$) would break gauge invariance, indicating the photon must be massless. From the free fermion

CHAPTER 2. THEORY

Lagrangian, imposing local gauge invariance leads to the full interacting field theory of QED. This is not a curiosity but an essential component of the theory, and the use of local gauge symmetry in deriving particle interactions does not end here.

Quantum chromodynamics

Quantum chromodynamics differs from QED in a few crucial ways. Since quark color fields exist, the QED $U(1)$ gauge group is replaced with $SU(3)$ and the free Lagrangian contains indices j to denote the three color fields:

$$\mathcal{L} = \bar{q}_j (i\gamma^\mu \partial_\mu - m) q_j. \quad (2.9)$$

QCD also carries three quark flavors, which will be ignored here for simplicity. The QCD group is non-Abelian since not all generators of the group commute with each other. These generators will be defined as T_a where $a = 1, \dots, 8$ and are linearly independent traceless 3×3 matrices (the Gell-Mann matrices λ_a are conventional). The local color phase transformation required is thus

$$q(x) \rightarrow e^{i\alpha_a(x)T_a} q(x). \quad (2.10)$$

We can consider an infinitesimal phase transformation as

$$\begin{aligned} q(x) &\rightarrow [1 + i\alpha_a(x)T_a]q(x), \\ \partial_u q &\rightarrow (1 + i\alpha_a T_a)\partial_\mu q + iT_a q \partial_\mu \alpha_a. \end{aligned} \quad (2.11)$$

Just as in the QED example, the last line breaks the invariance of \mathcal{L} , and we can proceed similarly by introducing a new gauge field (or in this case eight) called G_μ^a which transform as

$$G_\mu^a \rightarrow G_\mu^a - \frac{1}{g} \partial_\mu \alpha_a - f_{abc} \alpha_b G_\mu^c. \quad (2.12)$$

CHAPTER 2. THEORY

The last term added here is to cope with the non-Abelian nature of QCD.¹ Just as in QED this invariance forms a covariant derivative:

$$D_\mu = \partial_\mu + igT_a G_\mu^a. \quad (2.13)$$

Replacing the derivative in our Lagrangian and adding a gauge invariant energy term for each of the G_μ^a fields ($\frac{1}{4}G_{\mu\nu}^a G^{a\mu\nu}$) yields the final gauge invariant QCD Lagrangian:

$$\mathcal{L} = \bar{q}(i\gamma^\mu \partial_\mu - m)q - g(\bar{q}\gamma^\mu T_a q)G_\mu^a - \frac{1}{4}G_{\mu\nu}^a G^{a\mu\nu}. \quad (2.14)$$

Just as in the QED case, imposing local color phase invariance produced 8 new interacting fields with coupling g . These are the gluon fields and just like photons, local gauge invariance requires them to be massless. Unlike the QED case, this Lagrangian's new kinetic term includes self-interaction between the gauge bosons - another key feature of QCD that is mandated by local color phase invariance. Gluons themselves must carry color charge and therefore they self-couple. The structure of these self coupling terms and their single coupling strength g are uniquely determined by gauge invariance.

Electroweak unification

Thus far, I have summarized the theoretical backgrounds for symmetries (and so conserved quantities) in both quantum electrodynamics and chromodynamics. The weak force is the final Standard Model force and weak interactions are mediated by Z and W bosons. Unlike the gluons and photons of QCD and QED, these gauge bosons are massive. This is explained through spontaneous symmetry breaking of the electroweak force, which is outlined in the following section. Assuming that W/Z bosons are massive, the weak force can

¹Non-Abelian here means the generators T_a commute with each other.

CHAPTER 2. THEORY

be combined with QED and a central electroweak force (with its associated symmetries) can be described.

The weak neutral current J_μ^{NC} and weak charged currents (J_μ , J_μ^\dagger) can form a symmetry group for weak interactions. The charged currents correspond to the charged weak interaction through W^\pm bosons while the neutral current is associated with the Z boson:

$$\begin{aligned} J_\mu &= \bar{\nu}_L \gamma_\mu \nu_L, \\ J_\mu^\dagger &= \bar{e}_L \gamma_\mu \nu_L J_\mu^3 = \frac{1}{2} \bar{\nu}_L \gamma_\mu \nu_L - \frac{1}{2} \bar{e}_L \gamma_\mu e_L, \end{aligned} \quad (2.15)$$

where L denotes that these are left-handed spinors. The charged currents can be written as a doublet using the Pauli spin matrices τ_i where $\tau_\pm = \frac{1}{2}(\tau_1 \pm i\tau_2)$ and

$$\chi_L = \begin{bmatrix} \nu \\ e^- \end{bmatrix} \quad (2.16)$$

as

$$\begin{aligned} J_\mu^+(x) &= \bar{\chi}_L \gamma_\mu \tau_+ \chi_L, \\ J_\mu^-(x) &= \bar{\chi}_L \gamma_\mu \tau_- \chi_L, \\ J_\mu^3(x) &= \bar{\chi}_L \gamma_\mu \frac{1}{2} \tau_i \chi_L \text{ with } i = 1, 2, 3 \end{aligned} \quad (2.17)$$

The corresponding charge $T^i = \int J_0^i(x) d^3x$ can be introduced so we have an $SU(2)_L$ algebra

$$[T^i, T^j] = i\epsilon_{ijk}T^k. \quad (2.18)$$

Unfortunately while these currents create an $SU(2)$ group, they do not correspond with the weak neutral current symmetry in an obvious way. Unlike the charged currents, the neutral current has a right-handed component. One way to attain the expected symmetry is to add

CHAPTER 2. THEORY

in the electromagnetic current, as it is a neutral current with components

$$j_\mu^{em}(x) = -e_R \bar{\gamma}_\mu e_R - e_L \bar{\gamma}_\mu e_L \quad (2.19)$$

so the the electromagnetic current j_μ can be written using the coupling e

$$j_\mu = ej_\mu^{em} = e\bar{\psi}\gamma_\mu Q\psi \quad (2.20)$$

with Q the charge operator and generator of the $U(1)$ symmetry group of EM. In order to “save” the symmetry of the weak neutral current, we can define an electromagnetic current j_μ^Y , or the weak hypercharge current, that is unchanged by $SU(2)_L$ transformations. We define a weak hypercharge Y and its current j_μ^Y

$$\begin{aligned} Q &= T^3 + \frac{Y}{2}, \\ j_\mu^Y &= \bar{\psi}\gamma_\mu Y\psi. \end{aligned} \quad (2.21)$$

The combined current

$$j_\mu^{em} = J_\mu^3 + \frac{1}{2}j_\mu^Y \quad (2.22)$$

now generates the symmetry group $U(1)_\gamma$ and so the electromagnetic interaction and weak interaction are combined into one $SU(2)_L \times U(1)_\gamma$ group. While unified in this way, the two forces still have independent coupling strengths. This brief introduction into electroweak unification is not the complete picture—EM and weak *interactions* still have to be unified. In the Standard Model framework, electroweak currents just have to be coupled to vector bosons to complete unification. In the electroweak $SU(2)_L \times U(1)_\gamma$ group, there is an isotriplet of vector fields W_μ^i coupled with strength g to the weak isospin current J_μ^i , while a single vector field B_μ is coupled to the weak hypercharge current j_μ^Y with strength $g'/2$.

CHAPTER 2. THEORY

The electroweak Lagrangian interaction term can thus be defined:

$$-ig(J^i)^\mu W_\mu^i - i\frac{g'}{2}(j^Y)^\mu B_\mu. \quad (2.23)$$

This summary of the unified electroweak force will be the starting point for a derivation of the Higgs boson and an explanation for mass of the weak force's vector bosons (and all the fermions). The electroweak theory is unique in its calculability even at higher order scales. Consequently, theoretical uncertainties are relatively low and many deviations from theory could potentially be observed at current energy scales. The measurement central to my thesis probes for such discrepancies in electroweak theory. The mechanisms for this will be explained in the last section in this chapter.

Spontaneous Symmetry Breaking

Unlike QED and QCD, the weak force is mediated by massive gauge bosons. We therefore can not apply the same gauge invariance prescription that we did in the last sections. If a mass term is added to the Lagrangian, we break the gauge invariance we aimed to find. If we instead ignore the gauge invariance and add a mass term to the Lagrangian, all predictive power of the theory is lost due to unrenormalizable divergences. With “spontaneous symmetry breaking” we can gain massive gauge bosons while maintaining the integrity of the theory. In this section, I first describe the ”spontaneous symmetry breaking” mechanism in terms of an Abelian theory composed of complex scalar fields to illustrate the overall strategy. This mechanism is then applied to the non-Abelian electroweak theory to gain massive weak gauge bosons, W^\pm and Z , with the Higgs field appearing as a ‘spontaneous’ result.

CHAPTER 2. THEORY

The Lagrangian for a $U(1)$ gauge symmetry can be given as

$$\phi \rightarrow e^{i\alpha(x)}\phi. \quad (2.24)$$

As in the QED case, we introduce a gauge field A_μ and covariant derivative $D_\mu = \partial_\mu - ieA_\mu$ to obtain the gauge invariant Lagrangian,

$$\mathcal{L} = (\partial^\mu + ieA^\mu)\phi^*(\partial_\mu - ieA_\mu)\phi - \mu^2\phi^*\phi - \lambda(\phi^*\phi)^2 - \frac{1}{4}F_{\mu\nu}F^{\mu\nu}. \quad (2.25)$$

In this example if $\mu^2 > 0$ we gain back the QED Lagrangian for a charged scalar particle of mass μ with an additional self-interaction term. However, if we take $\mu^2 < 0$ the potential $V(\phi^*\phi) = \mu^2\phi^*\phi - \lambda(\phi^*\phi)^2$ acquires a non-zero vacuum expectation value (v.e.v.) and there is a set of equivalent minima shown in Figure 2.2. Choosing one of these minima spontaneously breaks the potential's rotational symmetry. We can perturbatively expand the field about a minimum through

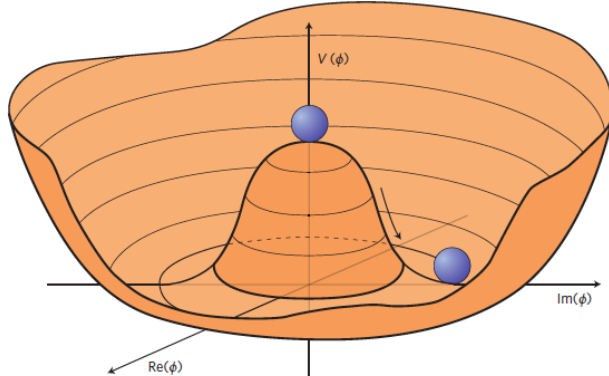


Figure 2.2: Higgs potential when $\mu^2 < 0$, choosing a minima spontaneously breaks the $U(1)$ rotational symmetry [3]

CHAPTER 2. THEORY

$$\phi(x) = \sqrt{\frac{1}{2}[\nu + \eta(x) + i\xi(x)]}. \quad (2.26)$$

We substitute this perturbation into the Lagrangian and gain

$$\mathcal{L}' = \frac{1}{2}(\partial_\mu \xi)^2 + \frac{1}{2}(\partial_\mu \eta)^2 - \nu^2 \lambda \eta^2 + \frac{1}{2}e^2 \nu_\mu^A A^\mu - e\nu A_\mu \partial^\mu \xi - \frac{1}{4}F_{\mu\nu} F^{\mu\nu} + \text{interaction terms.} \quad (2.27)$$

Three particles emerge here: a massless Goldstone boson ξ , a massive vector A_μ with $m_A = e\nu$, and a massive scalar η with $m_\eta = \sqrt{2\lambda\nu^2}$. However, the number of particles does not correspond to the expected polarization degrees of freedom expected. A longitudinal polarization was added, creating an unphysical field, and injecting extra degrees of freedom. To eliminate the unphysical field we can substitute a new set of fields:

$$\phi \rightarrow \sqrt{\frac{1}{2}(\nu + h(x))e^{i\theta(x)/\nu}} \quad (2.28)$$

and

$$A_\mu \rightarrow A_\mu + \frac{1}{e\nu} \partial_\mu \theta. \quad (2.29)$$

Introducing these substitutions, the Goldstone boson field disappears and the new Lagrangian becomes

$$\mathcal{L} = \frac{1}{2}(\partial_\mu h)^2 - \lambda \nu^2 h^2 + \frac{1}{2}e^2 \nu^2 A_\mu^2 - \lambda \nu h^3 - \frac{1}{4}\lambda h^4 + \frac{1}{2}e^2 A_\mu^2 h^2 + \nu e^2 A_\mu^2 h - \frac{1}{4}F_{\mu\nu} F^{\mu\nu}. \quad (2.30)$$

Here the degrees of freedom before our substitutions remains the same and a massive boson A_μ is preserved along with a massive scalar h . The “Higgs mechanism” applied to a scalar field succeeded in creating a massive boson and determined the existence of a massive scalar boson.

This same mechanism can be applied in the more complicated Standard Model elec-

CHAPTER 2. THEORY

Electroweak field. Through electroweak symmetry breaking, we not only gain massive gauge bosons and a massive scalar boson (the Higgs) but we also gain a way to calculate testable Standard Model predictions for many other quantities. We start with the $SU(2) \times U(1)$ gauge symmetry of electroweak interactions derived in the previous section. In order to gain masses for three gauge bosons and keep the photon massless, we need at least 3 degrees of freedom added, and a simple choice is to use the $SU(2)$ doublet of scalar fields ϕ , with four fields in an isospin doublet of weak hypercharge $Y = 1$:

$$\mathcal{L} = (D^\mu \phi)^\dagger (D_\mu \phi) - \mu^2 \phi^\dagger \phi - \lambda (\phi^\dagger \phi)^2, \quad (2.31)$$

where ϕ is a $SU(2)$ doublet of complex scalar fields

$$\phi = \sqrt{\frac{1}{2}} \begin{bmatrix} \phi_1 + i\phi_2 \\ \phi_3 + i\phi_4 \end{bmatrix}. \quad (2.32)$$

Local gauge invariance can be achieved just as in the $U(1)$ case with the covariant derivative, though now a bit more complex:

$$D_\mu = \partial_\mu + ig \frac{\tau_a}{2} W_\mu^a \quad (2.33)$$

with three gauge fields $W_\mu^a(x)$ and $a = 1, 2, 3$. An infinitesimal transformation is defined as

$$\phi(x) \rightarrow \phi'(x) = (1 + i\alpha(x) \cdot \tau/2)\phi(x) \quad (2.34)$$

and so the Lagrangian potential becomes

$$V(\phi) = \mu^2 \phi^\dagger \phi + \lambda (\phi^\dagger \phi)^2. \quad (2.35)$$

CHAPTER 2. THEORY

Once again if we choose the conditions $\mu^2 < 0$ and $\lambda > 0$ there is rotational symmetry in our choice of vacuum expectation value. In this case, the choice of v.e.v. is limited. For the photon to remain massless, the vacuum must be invariant under $U(1)$ (or electromagnetic) transformations, and not be charged in either direction (charge conservation). Thus the chosen minima to spontaneous break electroweak symmetry is

$$\phi_0 = \sqrt{\frac{1}{2}} \begin{bmatrix} 0 \\ \nu \end{bmatrix}. \quad (2.36)$$

Next, substituting the vacuum expectation value ϕ_0 for $\phi(x)$ and expanding perturbatively yields

$$\phi(x) \rightarrow \begin{bmatrix} 0 \\ \sqrt{\frac{1}{2}(\nu + H(x))} \end{bmatrix}. \quad (2.37)$$

Fully expanding this term in the Lagrangian gives a complex and illuminating result, the Goldstone bosons have been consumed and there is only a Higgs field ($H(x)$) remaining. Next, masses for the vector bosons are found from expanding one key parameter in the Lagrangian

$$|(-ig\frac{\tau}{2} \cdot W_\mu - i\frac{g'}{2}B_\mu)\phi|^2 = \frac{1}{8} \left| \begin{bmatrix} gW_\mu^3 + g'B_\mu & g(W_\mu^1 - iW_\mu^2) \\ g(W_\mu^1 + iW_\mu^2) & igW_\mu^3 + g'B_\mu \end{bmatrix} \begin{bmatrix} 0 \\ \nu \end{bmatrix} \right|^2. \quad (2.38)$$

Expanding further and substituting $W^\pm = (W^1 \pm iW^2)/\sqrt{2}$ gives the result

$$|(-ig\frac{\tau}{2} \cdot W_\mu - i\frac{g'}{2}B_\mu)\phi|^2 = (\frac{1}{2}\nu g)^2 W_\mu^+ W^{-\mu} + \frac{1}{8}(W_\mu^3, B_\mu) \begin{bmatrix} g^2 & -gg' \\ -gg' & g'^2 \end{bmatrix} \begin{bmatrix} W^{\mu 3} \\ B^\mu \end{bmatrix}. \quad (2.39)$$

It is immediately clear that there is a mass term for the W^\pm , $M_W = \frac{1}{2}\nu g$. Masses for the

CHAPTER 2. THEORY

photon and Z -boson are also apparent after expanding the last final term

$$\frac{1}{8}\nu^2(g^2(W_3^\mu)^2 - 2gg'W_\mu^3B^\mu + g'^2B_\mu^2) = \frac{1}{8}\nu^2(gW_\mu^3 - g'B_\mu)^2, \quad (2.40)$$

and using the substitutions

$$\begin{aligned} A_\mu &= \frac{g'W_\mu^3 + gB_\mu}{\sqrt{(g^2 + g'^2)}} \text{ with } M_A = 0, \text{ and} \\ Z_\mu &= \frac{gW_\mu^3 - g'B_\mu}{\sqrt{(g^2 + g'^2)}} \text{ with } M_Z = \frac{1}{2}\nu\sqrt{(g^2 + g'^2)}. \end{aligned} \quad (2.41)$$

Now the Higgs field exists just as in the previous example and the theory contains a massive scalar boson and three massive vector gauge fields—one for each of the W^\pm and Z bosons. The Goldstone bosons degrees of freedom were used to give mass to the vector bosons. Choosing a ground state and so breaking the gauge symmetry does not eliminate this symmetry altogether, since the theory is still renormalizable. Fermion masses can also be derived from their interactions with the Higgs boson using this Lagrangian. These derivations can be used to predict masses of bosons and fermions and couplings to the Higgs boson. It is important to note that the Higgs mechanism gives mass to all fermions and massive gauge bosons, but it does not determine what the Higgs mass ought to be. This is left as an empirical input to the theory that can then be used to calculate other observables.

The Standard Model has been proven over decades to be an incredibly robust theory. Since 2010, the Large Hadron Collider has become its key testing ground.

CHAPTER 2. THEORY

2.2 LHC Physics/Phenomenology

The Large Hadron Collider (LHC) is the foremost Standard Model testing ground, and the proton-proton collisions recorded with the ATLAS, CMS, ALICE, and LHCb detectors have demonstrated the breadth and accuracy of the theory. Fermion and gauge boson masses and couplings, including the mass of the Higgs boson, have been measured with high precision. In the next chapter, the mechanics of the LHC and ATLAS detector will be discussed. Here I will introduce the motivations and observations of LHC physics. This section will begin with the mechanics of proton-proton collisions and their decay products, then discuss the concept of decay cross-sections, and finally focus more closely on the Higgs boson and its properties.

One of the LHC’s central goal was to discover the missing Standard Model Higgs boson. The protons in the LHC collide at a center-of-mass energy of 13 TeV, but began at half that in 2010. The electroweak symmetry breaking scale was theoretically known to be between 100–1000 GeV, and so probing at 7 TeV provided near certainty of finding either the Higgs or an inconsistency in the Standard Model. The motivation for a proton collider was multifaceted. Foremost, using the tunnels built for the electron-positron detector LEP with protons allows the collider to reach higher energies, as protons do not lose as much energy to synchrotron radiation as electrons. However, proton collisions have added complexity from their component quarks. Each parton (quark or gluon in the proton) carries some fraction of the momentum of the proton described by parton distribution functions.

Figure 2.3 shows a proton-proton collision schematic. In this example the hard process comes from the up quark in each proton [4]. “Hardness” refers to the fraction of proton momentum involved in the collision. In contrast, “soft” collisions are those from remaining partons in each proton and usually involve low momentum transfer. These soft collisions

CHAPTER 2. THEORY

are considered the underlying event shown in the Figure 2.3. Parton scattering is the most common hard process at the LHC by far due to the high density of gluons in the proton and the scale of QCD couplings above electroweak coupling strength.

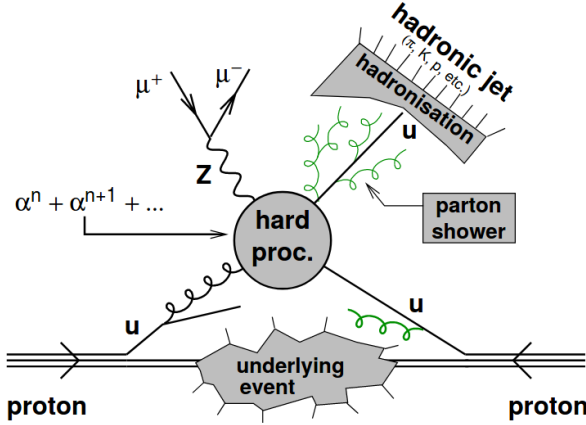


Figure 2.3: Example proton-proton collision with quark-gluon scattering and final state jet and Z-boson [4]

Quarks and gluons emitted from the high energy hard scatter do not appear in the detector directly. QCD, in one of its key differences to QED, becomes stronger with larger distances. As a parton reaches high enough energy, it will begin to radiate low-energy gluons until resultant partons are able to bind into color-neutral hadrons. These hadrons are seen collimated in groups in the detector, “jets”. The energy and momentum of jets are considered reflections of the initial scattered partons. Various “jet algorithms” can be used to determine initial parton properties as reproducibly and accurately as possible. The jet algorithm used in this analysis will be described in detail in Chapter 4. However, it is important to note that the algorithm used by all LHC experiments, anti- k_t , is collinear and infrared safe, unaffected by small angle and soft scatterings that occur in a parton shower. Without these qualities, perturbation theory applied to the parton shower would find infinities at high orders.

CHAPTER 2. THEORY

Cross-sections (denoted σ) measure the probability that a certain process will occur in the collision of two particles, in our case protons. In high energy physics, cross-sections are measured in femtobarns. A barn is the cross-sectional area of a typical nucleus, 10^{-28} m^2 , and was named to describe the large target area needed in order to have direct strikes on a nucleus. The name was inspired by the expression “could not hit the broad side of a barn”.²

Hard scattering cross-sections in hadron-hadron collisions can be calculated using the QCD factorization theorem, and to leading-order these calculations are relatively simple. In the factorization theorem, developed by Drell and Yan, deep inelastic scattering parton model processes could apply to hadron-hadron collisions. The Drell-Yan process is the production of a massive lepton pair by quark-antiquark annihilation. According to the factorization theorem, a hadronic cross-section $\sigma(ab \rightarrow \mu^+\mu^- + Y)$ could be calculated by rescaling the Drell-Yan sub-process cross-section $\hat{\sigma}$ for $\bar{q}q \rightarrow \mu^+\mu^-$ with parton distribution functions $f_{q/A}(x)$ from deep inelastic scattering [5]:

$$\sigma_{AB} = \int dx_a dx_b f_{a/A}(x_a) f_{b/B}(x_b) \hat{\sigma} ab \rightarrow X, \quad (2.42)$$

where X represents the two resulting leptons and ab the two annihilated quarks. This parton model provides good agreement with measured cross-sections and so allows understanding of particular hard scattering processes. Predictions for some key Standard Model processes are shown in Figure 2.4. Noting the logarithmic scales, it is clear that the Higgs boson of mass 125 GeV is over an order of magnitude more numerous at the LHC than the Tevatron and that certain high mass particles like the b quark and W/Z bosons are abundantly produced at the LHC [5]. In addition, the plot shows cross-sections of particular Higgs decay modes. These will be discussed next.

²Inverse femtobarns (10^{15} inverse barns) are used to measure the number of particle collision events per femtobarn area of a target and quantifies time-integrated luminosity.

CHAPTER 2. THEORY

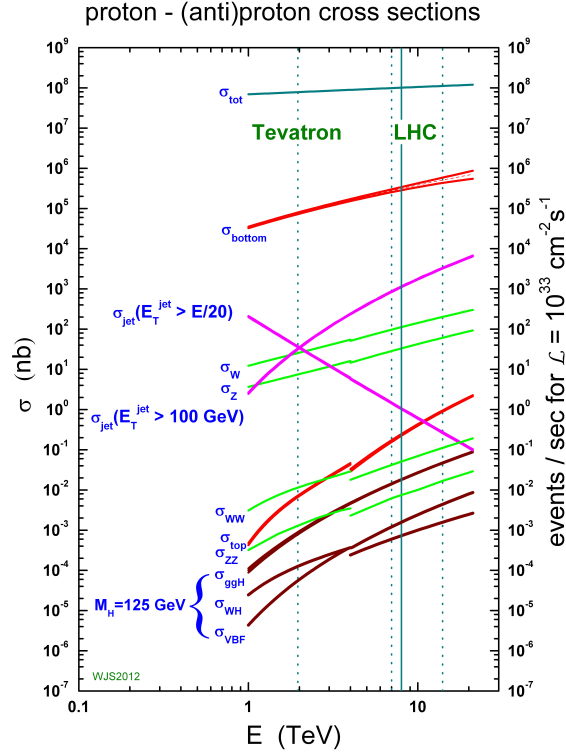


Figure 2.4: Predicted Standard Model cross-sections for the Tevatron and LHC [6].

Higgs production at the LHC occurs via four main processes: gluon-gluon fusion (ggF), vector-boson fusion, associated production with W/Z bosons, and associated production with top or bottom quarks. The Feynman diagrams for these processes are shown in Figure 2.5.

CHAPTER 2. THEORY

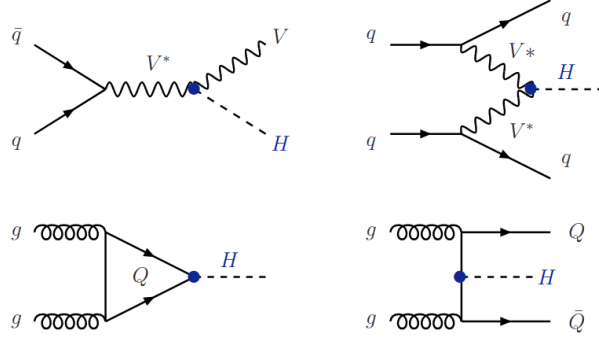


Figure 2.5: Feynman diagrams for the leading Higgs boson production modes at the LHC [7].

The LHC Cross-section Working Group produces predictions on cross-sections, branching ratios, and pseudo-observables for the Higgs boson. Four CERN reports bring together Higgs prescriptions for current and planned LHC efforts [8]. Figure 2.6 shows the Higgs cross-section for the main production modes as a function of the Higgs mass and the collision center-of-mass energy. The Standard Model does not predict the Higgs mass, but experimentally we know that $m_H \approx 125$ GeV. Examining cross-section as a function of center-of-mass demonstrates the increase in statistics for events of interest that running the detector at higher energy levels can accomplish. Figure 2.6 also shows that gluon-gluon fusion Higgs production is the leading production mechanism by far. The Higgs production cross-section is currently known at next-to-next-to-leading-order (NNLO) in QCD with next-to-leading-order (NLO) EW corrections.

The second highest production cross-section is from vector boson fusion. As seen in the Feynman diagram, two outgoing quarks are produced in the interaction. These quarks produce two hard jets in the forward region with the Higgs boson appearing between them. To leading order, VBF Higgs production is solely electroweak, and QCD corrections (calculated at NLO) have a smaller impact than in ggF. NLO EW corrections are also applied. As a

CHAPTER 2. THEORY

result, VBF theoretical uncertainties are smaller than those on ggF. Vector boson associated Higgs production through a W/Z boson are less common than VBF but also dominated by electroweak processes with a small QCD correction (NNLO). Finally, associated production with top and bottom quarks is shown, though these are quite rare and have high NLO and NNLO QCD corrections.

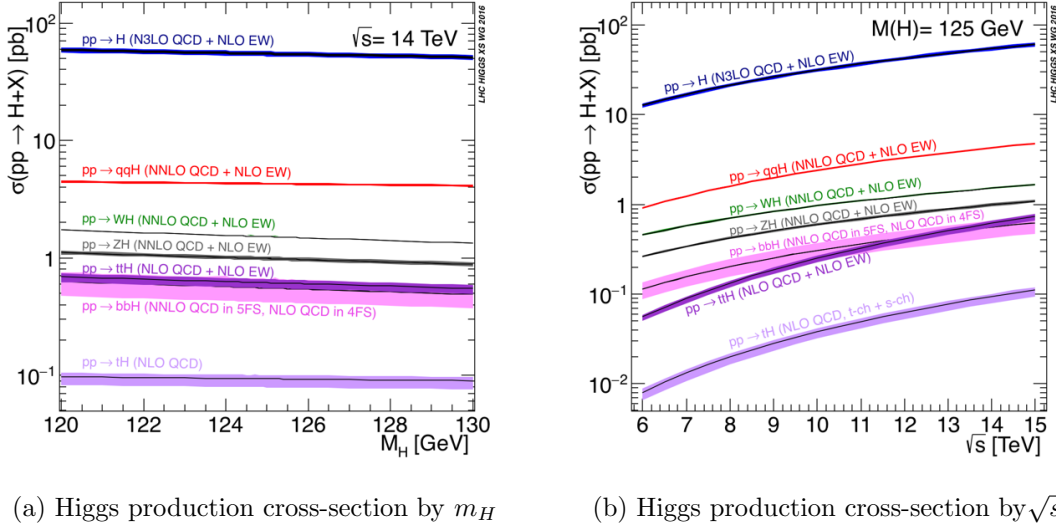


Figure 2.6: Higgs production cross-sections over Higgs mass at center-of-mass energy 14 TeV (left) and over center-of-mass energy for a Higgs mass of 125 GeV (right)[8]

Theoretical uncertainties shown as colored bars in 2.6 are calculated from choice of PDFs and renormalization and factorization scales. Parton distribution functions (PDFs) are described in more detail by the PDF4LHC working group [9]. This group performs studies of PDFs and their predictions at the LHC and makes recommendations for methods of estimating PDF uncertainties.

CHAPTER 2. THEORY

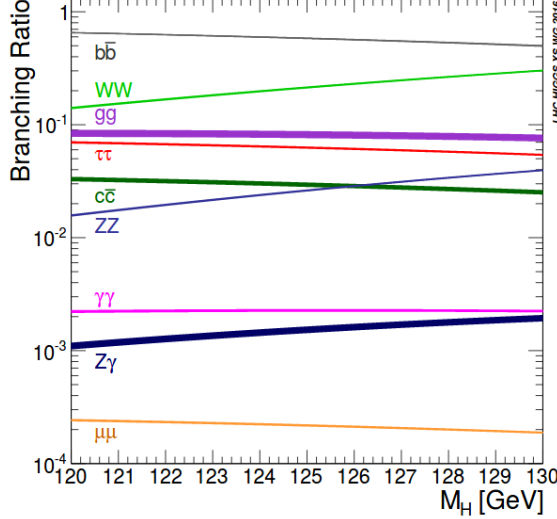


Figure 2.7: Predicted branching ratios for the Higgs boson at the LHC as a function of Higgs mass [8].

Since the Higgs boson couplings are directly proportional to the masses of each particle, the Higgs decays most readily into the heaviest particles possible. Figure 2.7 shows key decay mode branching ratios near the experimentally known Higgs mass. While the branching ratios demonstrate the relative abundance of each Higgs decay, these do not translate directly into their ease of discovery or measurement. The current status of Higgs boson coupling and cross-section measurements for each decay mode will be detailed in the next section. The Higgs boson discovery was made through a combination of searches in many channels though dominated by $H \rightarrow ZZ^*$, $H \rightarrow \gamma\gamma$, and $H \rightarrow WW^*$ [10]. This is because though other decay branching ratios are higher, like $H \rightarrow b\bar{b}$, the backgrounds associated with this decay are much higher. As previously mentioned, proton-proton collisions create large amounts of QCD jets that are difficult to discern from target hard QCD processes. Because of this, Higgs decays to quarks and gluons are particularly difficult and those with decays to heavy and light bosons (ZZ decays to 4 leptons, decays directly to photons, and WW decays to two leptons and two neutrinos) are easier to reconstruct. As energy and integrated luminosity

CHAPTER 2. THEORY

increased during LHC data-taking, measurements of even rare and background-heavy Higgs decay channels could be made. This thesis focuses on the decay of $H \rightarrow W^+W^- \rightarrow \ell\nu\ell\nu$ through VBF production. In the last section of this chapter I will motivate the choice of these conditions for probing new physics beyond the SM.

2.3 Brief history of SM tests

Here I summarize key moments in the history of the development of the Standard Model and its experimental tests. I use both Refs. [11] and [12] as a guide.

The history of the Standard Model could start with any number of physicists well before the formalism of the theory itself. As far back as the fifth century B.C. philosophers posited that matter is composed of discrete “particles” in its most fundamental state. This idea was only tested beginning in the nineteenth century, when scientists were able to detect physical evidence of atoms and their structure. The first of the gauge theories, QED, was invented in the 1930s but only calculated to first order. Renormalization theory was invented simultaneously by Feynman, Schwinger, and Tomonaga in the 1940s. This made calculations of higher order QED results possible. Following this advancement, QED was verified experimentally with high precision.

Physicists next attempted to understand and formalize the other fundamental forces, strong and weak, in the same way. Symmetries for these theories were not as easy to find as that of QED, and in 1954 the first new gauge theory for QCD was proposed by Shaw, Yang, and Mills. Though ultimately incorrect, it led to proposals for a gauge theory of weak interactions by Schwinger in 1956 (unifying weak and electromagnetic interactions with photons and massive W^\pm bosons). Glashow added a fourth boson, Z , to the theory, but the problem of a broken symmetry necessary to give mass to the W/Z bosons remained.

CHAPTER 2. THEORY

Spontaneous symmetry breaking was a known and tested concept, but its use in the theory led to unwanted massless “Nambu-Goldstone” bosons. Some thought this problem was inevitable in using SSB in the gauge theory. In 1964 Englert and Brout, then Higgs, and a few months later Guralnik, Hagen, and Tribble all published papers with the same conclusion—the Goldstone theorem can be applied to gauge theories and massive bosons can “eat” the Nambu-Goldstone bosons to gain mass. This then creates a new scalar field whose particles are now termed Higgs bosons. A few years later Weinberg unified these ideas into the electroweak theory we recognize today. The theory was confirmed many times over at experiments over the next decades.

While electroweak symmetry breaking and its implications were being understood in the 1960s, QCD was gradually being assembled. Experimental discoveries of a host of new particles led to Gell-Man and Zweig’s development of a theory that these were all composed of the same three base particles, “quarks”. Han and Nambu understood that an octet of colored gauge bosons, “gluons”, mediated the strong force through color interactions. In 1973 Gross, Wilczek, and Politzer demonstrated the asymptotic freedom of QCD, its weakness at short distances which allows perturbation theory to calculate high energy interactions. The Standard Model, as it is composed of electroweak dynamics and QCD, has been remarkably predictive but there is much it does not explain, such as the existence of dark matter particles. While theoretical physicists work to expand the Standard Model (or replace it entirely), experimentalists search for deviations from Standard Model predictions, which may be the next hint of entirely new physics.

Large amounts of experimental evidence for the predictive power of QED had amassed over time, and by the 1970s high energy accelerators at CERN, Fermilab, Brookhaven and SLAC began making first measurements of predicted electroweak and QCD observables. In 1969 physicists at SLAC collided electrons and protons and found that electron scattering

CHAPTER 2. THEORY

behaved as though the proton was made up of point-like particles, quarks. Electroweak theory's predicted neutral weak current interaction between quarks and leptons was discovered at CERN and then Fermilab in 1973, giving evidence to electroweak unification. The W and Z bosons predicted by the theory with masses ≈ 80 GeV were discovered at the SPS at CERN. This was the first proton-antiproton collider and with a center-of-mass energy of 540 GeV, it was then the highest energy collider ever built. The collider was built for the main purpose of finding the predicted W and Z bosons, and it succeeded in discovering both in 1983. Electron-positron colliders like LEP at CERN and SLC at SLAC were able to produce millions of Z bosons and so test electroweak predictions with high precision. The theory continued to prove extremely accurate. QCD remains more difficult to test precisely, as calculating QCD parameters theoretically is a computationally difficult task. However, evidence of QCD's accuracy has accumulated. In 1978, DESY was able to indirectly detect the first gluon. The electron-positron collider produced two quarks that formed two jets of particles with equal energy in opposite directions. QCD predicts that there would also be 3-jet events, where a gluon would be radiated from one of the scattered quarks and form a third. The strength of the strong interaction was first measured in 1978 and thereafter with more and more precision and has always followed QCD predictions. Quarks beyond the first generation (up, down) were discovered in order of increasing mass - strange first, followed by charm, then bottom, and finally in 1995 the top. Similarly, the muon was discovered well before the heavier tau-lepton which was not directly observed in the early 2000s. After these discoveries, the last Standard Model particle left undiscovered was the Higgs boson. Its mass is an input rather than a prediction to the Standard Model, but with the large amount of data taken at increasingly high energy colliders, experimentalists and theorists were confident that if it existed, its mass would be between 100 GeV and 1 TeV. In order to search for the Higgs boson, the Large Hadron Collider was planned and built at CERN.

CHAPTER 2. THEORY

The collider and its largest all-purpose detector, ATLAS, are discussed in the next chapter.

In 2012, the Higgs boson was discovered at the LHC in both the ATLAS and CMS detectors. After just one year of data-taking at a 7-8 TeV center-of-mass energy, combined searches in the $H \rightarrow ZZ^* \rightarrow \ell\ell\ell\ell$, $H \rightarrow \gamma\gamma$ and $H \rightarrow WW \rightarrow \ell\nu\ell\nu$ channels found a particle compatible with the Standard Model Higgs with a significance of 5.9 standard deviations at a mass close to 125 GeV. The LHC continued data-taking after the discovery with a new goal: measuring this new particle’s properties with accuracy and precision. In 2015, the center-of-mass energy increased to 13 TeV and more than 20 times the data used in the first discovery has now been recorded.

Measurements of the Higgs boson are now numerous and quite precise, but no deviations were observed from the theoretical expectation. While the Standard Model has proven a successful model of known interactions, there are many phenomena that it does not predict—from dark matter to neutrino masses. There must be physics beyond this theory. In continuing to probe new aspects of the model, the LHC may find deviations from the known forces or physics beyond the Standard Model.

The mass of the Higgs boson is measured through a combination of decay modes and in combination with CMS to be 125.10 ± 0.14 GeV [1]. The latest combined Higgs cross-section measurement from ATLAS uses data from 2015-2017 and finds the production cross-sections (normalized to their Standard Model predictions) as shown in Figure 2.8. Branching ratios of relevant decay modes are also measured and are shown in Figure 2.9 multiplied by their cross-sections in each relevant production mode. The differences in theoretical and systematic uncertainty for certain decays (QCD heavy VBF $H \rightarrow b\bar{b}$ in comparison to the leptonically decaying VBF $H \rightarrow WW^*$) show how discernable backgrounds play a major role in the viability of a measurement, even when the branching ratio is high [13].

CHAPTER 2. THEORY

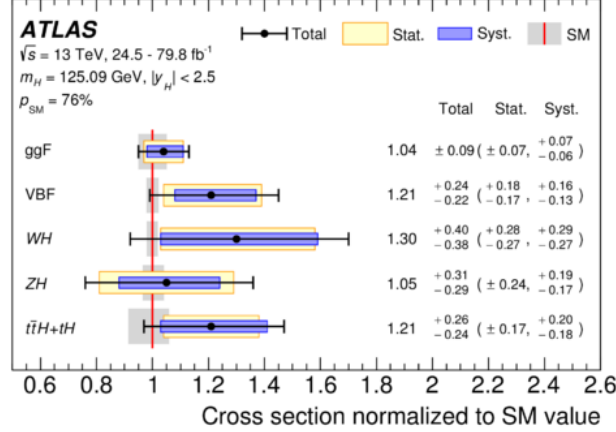


Figure 2.8: Production cross-sections for ggF, VBF, VH, and $t\bar{t}H + tH$ normalized to their SM predictions. Total, systematic, and statistical uncertainties are shown [13]

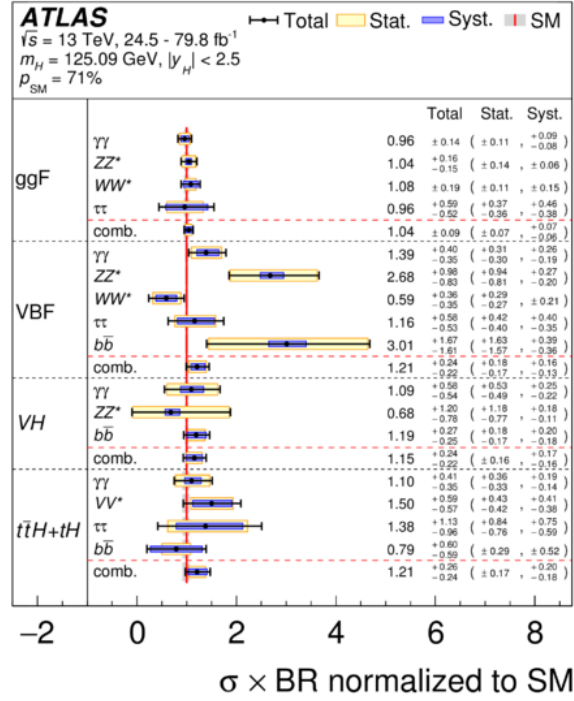


Figure 2.9: Branching ratios for measured Higgs decays normalized to their SM predictions. Total, systematic, and statistical uncertainties are shown [13]

CHAPTER 2. THEORY

This thesis details my work on the fiducial cross-section measurement of VBF $H \rightarrow WW^* \rightarrow \ell\nu\ell\nu$ decays. The clear sign of VBF Higgs production (2 jets recoiling in opposite high η directions, combined with the leptonically decaying W bosons) gives the decay a distinctive signature. This channel can be measured with high accuracy which may allow small deviations from theory to be visible. In addition, the measurement is made with the goal of eventual differential cross-section measurements, which can probe higher order perturbative contributions to QCD or EW. Details on the particular motivations for this thesis' analysis will be outlined in the next section. The last ATLAS $H \rightarrow WW^*$ differential measurement was published in 2016 with 20.3 fb^{-1} at center-of-mass energy 8 TeV and measured only ggF Higgs boson production differential cross-sections [14].

2.4 Measurement motivation

There are many reasons why the VBF $H \rightarrow \ell\nu\ell\nu$ channel is particularly interesting to investigate. Since the W bosons decay leptonically, they create a clear signal in the detector which allows for a precise reconstruction of the hard processes. Further, the VBF production mode has a similarly clear signal with the two jets accompanying the decaying W bosons with a high η separation. The pseudorapidity of these jets and the rapidity between them are particularly sensitive to the electroweak symmetry breaking mechanism, so a differential cross-section measurement over these variables (along with other detailed and motivated in further sections) tests the Higgs mechanism. In 2019, VBF $H \rightarrow WW^* \rightarrow \ell\nu\ell\nu$ cross-sections were measured in 2015-2016 data with an experimental uncertainty of $\approx 50\%$ [15]. This new measurement uses all data recorded from 2015-2018, with a factor of 3.9 times higher statistics. This VBF $H \rightarrow WW$ fiducial cross-section measurement uses new analysis techniques and improvements in theoretical calculations as well as higher statistics to make

CHAPTER 2. THEORY

an accurate probe of new physics within the electroweak symmetry breaking mechanism.

This thesis focuses on the VBF $H \rightarrow WW$ fiducial cross-section measurement, but this measurement is the first piece to a larger goal beyond the scope of my Ph.D. Our group plans to make a simultaneous measurement of VBF $H \rightarrow WW$ and VBF $W + \text{jets}$ fiducial and differential cross-sections. The VBF $W + jj$ production cross-section is sensitive to the WWV vertex. In vector boson scattering, we expect (with minimal assumptions) that new physics ought to be at a scale above the current experiment. Effects from this type of new physics would simultaneously affect HWW and WWV vertices. In particular, dimension-6 operators affect VBF Higgs mechanisms and VBF W production, while the interplay of VBF and VBS mechanisms allows for the probe of dimension-6 and dimension-8 operators. Measuring fiducial and differential cross-section ratios (of VBF Higgs and Wjj) enhances sensitivity to new physics because any new phenomena that simultaneously affect both vertices are suppressed and so sensitivity to the phenomena affecting just the WWV vertex (for example, anomalous quadruple-gauge couplings) is enhanced. VBF Higgs and Wjj productions are also characterized by final-states with two jets with similar kinematics. Because of this, the ratio of cross-sections measurement allows for the cancellations of correlated systematic uncertainties. As both process are characterized by large ($10\% - 20\%$) jet-related uncertainties, a reduction via the ratio cancellation would greatly improve the sensitivity to the VBF Higgs process and to the search for new phenomena. This VBF HWW measurement is the first part of the ratio of fiducial differential cross-sections for VBF HWW and Wjj , which will set limits on parameters, benefiting from enhanced sensitivity through the cancellation of correlated uncertainties.

Chapter 3

The LHC and the ATLAS detector

The Large Hadron Collider (LHC) is a proton-proton storage ring operating at CERN, and for its 9 years of operation, it has been the world's highest energy particle collider. During LHC operation thus far, protons have collided with increased center-of-mass approaching the design energy of 14 TeV. Instantaneous luminosity has also successively increased, surpassing design instantaneous luminosity of $1 \times 10^{34} \text{ cm}^{-2}\text{s}^{-1}$ in 2018 to reach $2 \times 10^{34} \text{ cm}^{-2}\text{s}^{-1}$ [16]. The overall data recorded in the ATLAS detector totals more than 10^{16} collisions. Operation of the LHC has led to the discovery of the Higgs boson and some of the most precise measurements of its properties including the coupling of the Higgs boson to bottom quarks [17], W and Z bosons [15, 18], photons [19] and tau leptons [20]. The LHC has also facilitated searches for new physics over a wide parameter space, setting confidence level exclusion limits on masses of supersymmetric particles like squarks, gluinos and neutralinos [21].

The LHC can run continuously for a few years before detector components need to be repaired and replaced. The schedule of data-taking consists of long periods of data accumulation (Run 1 and Run 2) paired with long shutdown periods. The LHC is set to begin Run 3, in which the design center-of-mass energy should be reached, in 2021. Following Run

CHAPTER 3. THE LHC AND THE ATLAS DETECTOR

3, detector upgrades will be installed during a long shutdown. Then the High-Luminosity LHC (HL-LHC) will begin colliding protons with unprecedented ($10\times$) luminosity in 2027 [22]. The HL-LHC and its goals will be explained further later in this chapter. Suffice to say LHC physics is progressing quickly and promises exciting developments in the near future.

In a brief explanation of the LHC operation, one could begin with the small volume of $\approx 10^{11}$ protons that are accelerated per bunch. Linac-2 is the primary accelerator for CERN colliders and has been since the early 1990s [23]. This injects protons at 50 MeV into the Proton Synchrotron Booster (PSB) where they are further accelerated to 1.4 GeV. In the the Proton Synchrotron (PS), the protons are separated into bunches with a spacing of 25 ns and are futher accelerated to 25 GeV before being extracted to the Super Proton Synchrotron (SPS), where they reach 450 GeV. Finally the bunches of protons enters the LHC, where they are accelerated to their final energy of 6.5 TeV. Linac 2, PSB, PS, and SPS were all operational accelerators before the LHC era though each had to be majorly upgraded to handle the energy and beam intensity required for LHC collisions [23].

The LHC layout mimics that of the Large Electron Positron collider (LEP) that was housed in the same tunnels. Figure 3.1 shows the positioning of each experiment at the LHC as well as injection systems and other features. Once proton bunches enter the LHC in two opposing beams, they are accelerated with radio frequency (RF) systems. Located at Point 4 in the LHC schematic, the system consists of 16 RF cavities operating at twice the frequency of the SPS injector. RF cavities are metallic chambers containing oscillating electromagnetic fields; in the LHC this oscillation frequency is 400 MHz. The tuning of this frequency ensures that protons of the ideal energy are not accelerated further and simply maintain their momentum while particles arriving in an RF cavity slightly before or after will be decelerated or accelerated toward the ideal proton energy. This acceleration process can also be used to split beams of protons into discrete bunches, and this is first done with

CHAPTER 3. THE LHC AND THE ATLAS DETECTOR

RF cavities in the PS. After proton bunches have circled the LHC approximately 1 million times (15 minutes), peak energy is reached and collisions can commence [24].

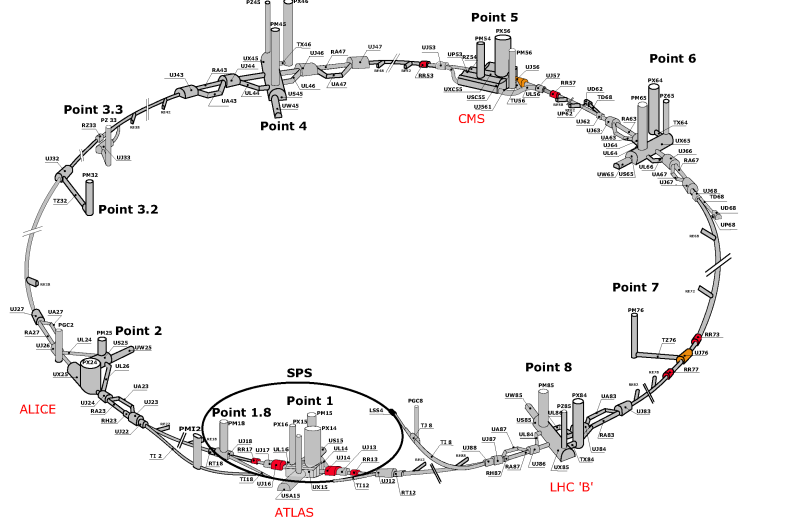


Figure 3.1: LHC layout [25]

Superconducting magnets in the LHC main dipoles create a magnetic field of ≈ 8 T to bend the proton beams into the circular path of the collider. Figure 3.2 shows the flux in a dipole cross-section. The opposing direction beamlines are shown centered and the flux is shown to be high (and directionally opposed) in the center of each beam. To maintain these fields, the magnets operate at below 1.9 K. Pressurized superfluid helium chosen for its low viscosity and high specific heat cools the dipole magnets. Once the two LHC rings are filled from the SPS, the center-of-mass energy of the beams increases until it reaches peak energy after about 28 minutes. Finally, proton bunches separated by 25 ns collide simultaneously in each detector.

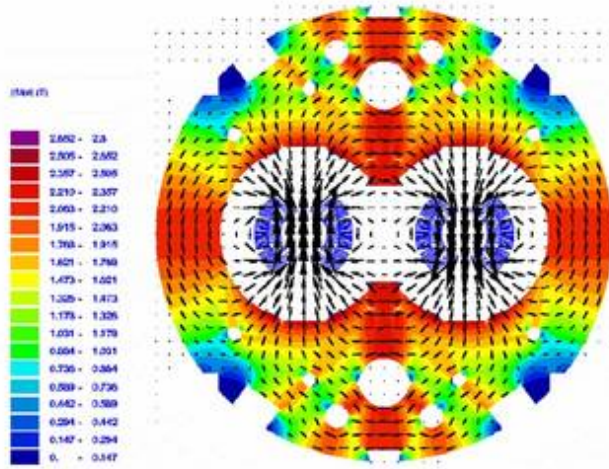


Figure 3.2: Flux within an LHC dipole cross-section [25]

3.1 ATLAS

The LHC creates proton-proton collisions at the rate and energy necessary for pushing the boundaries of particle physics, but identifying and reconstructing the tracks of such energetic particles is no mean feat. A Toroidal LHC ApparatuS (ATLAS) and the Compact Muon Solenoid (CMS) are multi-purpose detectors built to search for a wide range of particle interactions and the measurement of their properties. Both experiments measured a particle consistent with the Higgs boson in 2012, and their agreement was a key verification of the discovery. The following sections describe each major component of the ATLAS detector, shown in Figure 3.3, so to highlight their role in the measurement of $H \rightarrow WW \rightarrow \ell\nu\ell\nu$.

ATLAS utilizes a coordinate system with its origin at the center of the detector (the “interaction point”) and z-axis along the beam pipe. The x-axis points from the interaction point to the center of the LHC ring, and the y-axis points upward. The experiment uses cylindrical coordinates (r, ϕ) where ϕ is the azimuthal angle around the beam pipe. The pseudorapidity and the transverse momentum are defined in terms of the polar angle θ as

CHAPTER 3. THE LHC AND THE ATLAS DETECTOR

$\eta = -\ln(\tan(\theta/2))$ and $p_T = p \sin \theta$, respectively.

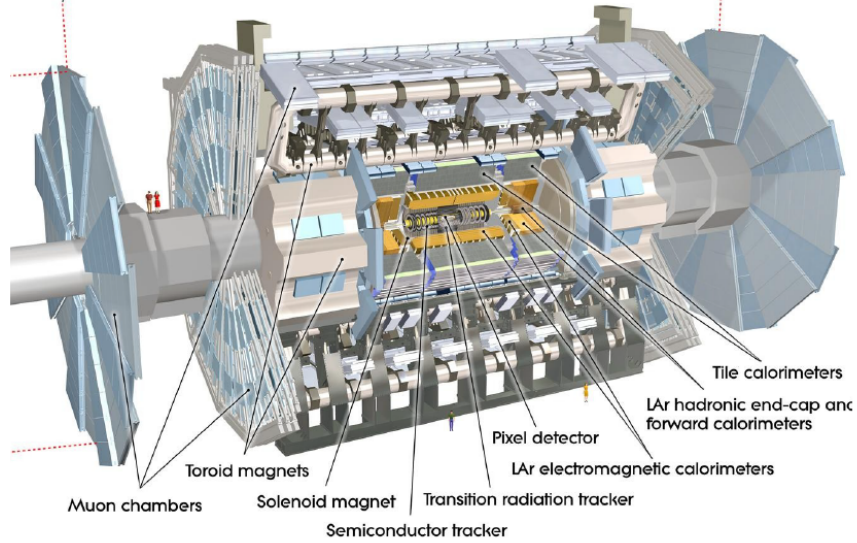


Figure 3.3: Computer-simulated ATLAS detector schematic [26]

The Inner Detector (ID) detects charged particles with $|\eta| < 2.5$ in a 2 T solenoidal field. It consists of 3 layers of pixel sensors, 4 layers of silicon strips, and 72 straw layers of transition radiation tracker modules. The ID describes particles closest to the interaction point and locates track parameters with great resolution due to its high granularity [26].

The ATLAS detector contains 3 superconducting magnet systems—the central solenoid, barrel toroid, and 2 endcap toroids. The central solenoid provides a magnetic field for the inner detector while the toroids create a strong magnetic field for the muon detector. These magnets were built to create the largest possible uniform magnetic field to maximize the momentum resolution on particle tracks. They also need to use as little material as possible so as to not unduly influence particles in the detector. The toroids in the barrel and endcap each have 8 coils and create a 4 T magnetic field while the central solenoid creates a 2 T magnetic field in the inner detector. Combined the magnet systems contain more than

CHAPTER 3. THE LHC AND THE ATLAS DETECTOR

100 km of superconducting wire which are cooled to working temperatures below 5 K [26].

The Muon Spectrometer (MS) precision chambers provide muon momentum measurements at a high resolution over a wide range of p_T . The MS consists of 3 layers of Monitored Drift Tube chambers covering $|\eta| < 2.7$ and an inner layer of Cathode Strip Chambers with $|\eta| > 2.0$ in the small wheel of the endcap. In addition, it includes trigger chambers that contain 3 layers of Resistive Plate Chambers ($|\eta| < 1.05$) and 3 layers of Thin Gap Chambers ($1.05 < |\eta| < 2.4$). As the outermost subdetector, the MS provides precise muon momentum measurements along the muon trajectory, and the muon chambers are located with a precision of under 60 μm . The MS also contains a system of three superconducting toroidal magnets each with eight coils providing a magnetic field with a bending integral of up to 6 Tm [26].

Calorimeters provide detailed information about the energy deposited as particles pass through. Electromagnetic calorimeters detect and halt the motion of electrons and photons while the hadronic do the same for hadrons. Muons and neutrinos are able to pass through the calorimeters to the MS [26].

3.2 The High-Luminosity LHC and Inner Tracker

The LHC attained its paramount design goal by discovering the Higgs boson in 2012. Its operation at higher energy and luminosity has led to rigorous measurements of Higgs boson properties as well as searches for new physics beyond the Standard Model. While more data collection is planned in Run 3 starting in 2021, new colliders and detectors take decades to design, develop and build, so the plans for upgrading the current detectors are well underway. The High Luminosity LHC will operate at 14 TeV starting in 2027. The HL-LHC will begin with 5–7 times the luminosity of the LHC and 10 times the design instantaneous luminosity

CHAPTER 3. THE LHC AND THE ATLAS DETECTOR

of the LHC, or $12.6 \times 10^{-34} \text{ cm}^{-2}\text{s}^{-1}$. This huge increase in number of collisions requires substantial upgrades to the LHC including new 11–12 T superconducting magnet systems, compact superconducting cavities for beam rotation and phase control, and new technology beam collimation [27].

Just as the LHC had to be re-designed, so do all the experiments to handle the much higher luminosity. The detectors must be built to withstand more radiation, as the increased collision rate also means a high radiation rate, especially closest to the beamline. They also need greater granularity to be able to reconstruct individual tracks with good resolution. Finally, they have to faster to deal with high numbers of collisions occurring in each proton bunch. When there is a large amount of pile-up it becomes difficult to trace which particle tracks come from the same interaction point. Finally, the increased data creates a complex problem for the trigger system, since it must quickly select and store the events that may hold interesting information.

Detectors for high energy colliders are not built often—expensive and time-consuming to design and test, so they are made to last at least a decade. I had the opportunity to work on ATLAS detector research and development during the 1.5 years I worked at Brookhaven National Laboratory. Though my thesis is not directly related to this work, it was formative and extremely interesting, so I touch on this in the next section. Because I worked on the new ATLAS Inner Detector, termed the Inner Tracker, for the HL-LHC, I discuss this sub-detector and the particular role I played in its assembly in Appendix A.

Chapter 4

Reconstruction of Physics Objects

The measurement of $H \rightarrow WW^* \rightarrow \ell\nu\ell\nu$ cross-sections relies on the accurate determination of a number of “physics objects” within the detector, primarily jets, missing transverse energy (E_T^{miss}), electrons, and muons. The final state particles of this interaction consist of one electron, one muon, and two neutrinos, which appear as missing transverse energy in the detector since they cannot be directly detected. The different flavored leptons are required in our final state to eliminate large contamination from Drell-Yan ($Z/\gamma^* \rightarrow ee/\mu\mu$) backgrounds. Drell-Yan backgrounds still play a role in our different flavor selection analysis but primarily come from far less numerous $Z/\gamma \rightarrow \tau\tau$ events which then decay to an electron and muon. Because our search focuses on VBF production Higgs bosons, we also require two jets in the final state. Each physics object has a dedicated performance group in ATLAS which is tasked with providing recommendations for reconstruction, identification, isolation and measurements of efficiency, scale, and resolution. Biases or omissions in any of these would severely impact the precision of our analysis. Understanding the uncertainties associated with each reconstructed object is critical. In this chapter I briefly outline the algorithms used for tracking and isolation to accurately determine the kinematics of electrons,

CHAPTER 4. RECONSTRUCTION OF PHYSICS OBJECTS

muons, jets and missing transverse energy. Particular attention will be paid to muons, as I spent a significant amount of time working in the Muon Performance Group applying and validating corrections to muon momentum scale and resolution.

4.1 Tracking

Track reconstruction is fundamental to accurately identifying and describing electrons, muons, and jets through information from the ID. Charged particles in the ID follow a circular trajectory because of the magnetic field from the central solenoid. They can be fully explained with a set of five parameters:

- q/p_T , the charged curvature where q is electric charge and p_T transverse momentum
- ϕ , the azimuthal angle
- θ , the polar angle
- d_0 , the transverse impact parameter or distance of closest approach of the beamspot position in the $x - y$ plane
- z_0 , the longitudinal impact parameter, or z coordinate of the track at the point of closest approach.

Track reconstruction calculates these descriptive parameters for each located track through an initial *inside-out* procedure and second *outside-in* method [28]. First, track seeds are built from three hits in the silicon detectors, required to be in different silicon detector layers. Hits are then added to seeds moving away from the interaction point. If the final number of hits exceeds a determined threshold a track candidate is created and if not, the hits are discarded. Next for the *outside-in* approach, segments are reconstructed in the TRT and silicon hits are

CHAPTER 4. RECONSTRUCTION OF PHYSICS OBJECTS

added through back-tracking. This approach finds tracks from secondary interactions which do not begin at the primary interaction point. Requirements on hits, holes (points where measurement is expected but not found), and outliers (hits that reduce track fit quality) reduce tracks which can not be matched to the primary vertex or secondary particles [29]. The ATLAS Tracking Performance group determines reconstruction performance for tracks and measure their robustness to potential fake track candidates and pile-up. Reconstructed tracks are used as input for the identification and measurement of kinematic variables for each of the physics objects that are described in this chapter.

4.2 Electrons

Accurate reconstruction and calibration of electrons within the ATLAS detector is integral to precision measurements, including the $H \rightarrow WW$ measurements in which an electron is required in the final state. Reconstruction, identification, and energy measurements of electrons and photons are the goals of the Electron and Photon Performance group. This section will summarize each of these calibration processes and their performances with a focus on electrons.

Electrons are defined through energy deposited in the calorimeter, the superclusters, each with a matching track from the ID. Photons are defined strictly through a calorimeter cluster. Figure 4.1 shows the procedure for electron and photon reconstruction. First, topo-clusters in the EM calorimeter and tracks in the ID are selected and matched together. Topo-clusters are defined based on signal to noise significance in calorimeter cells and calorimeter cell proximity. Standard reconstruction takes place in the ID and potential tracks are assigned to topo-clusters if their positions are within a region-of-interest compatible with that topo-clusters EM shower. Next, super-clusters are built from track-matched topo-clusters. Topo-

CHAPTER 4. RECONSTRUCTION OF PHYSICS OBJECTS

clusters are tested for use as seed cluster candidates which begin super-clusters. Remaining topo-clusters are tested for compatibility as satellite clusters to each seed candidate. The resultant combination of seed and satellite clusters form super-clusters which are defined independently for photons and electrons. Finally, tracks are added to super-clusters, energy calibration and position corrections are applied, and analysis-level electrons and photons are created. Reconstruction efficiency for electrons is quite high, approaching the tracking efficiency at high p_T . Photon reconstruction efficiency is significantly lower due to their dependence solely on calorimeter clusters [30].

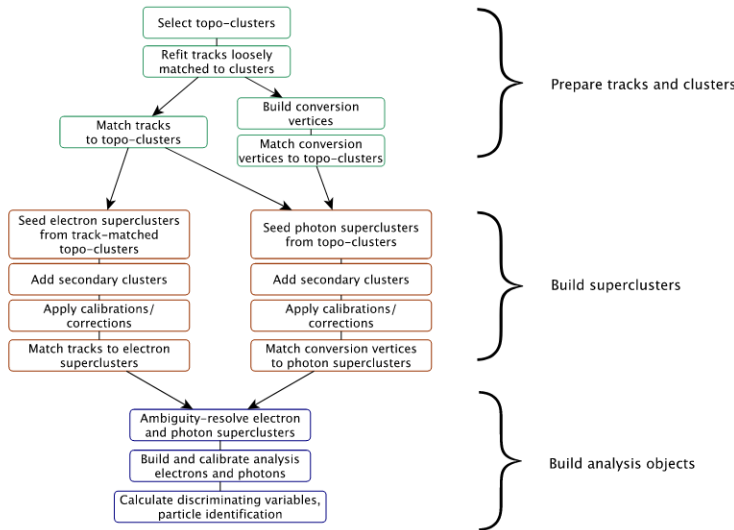


Figure 4.1: Electron and photon reconstruction algorithm [30]

Electron and photon energy resolution is determined from EM calorimeter showers and is optimized with multivariate regression algorithms. Electron and photon scale is also corrected using calibrations derived from $Z \rightarrow ee$ decays and verified with other Z -boson decays. Similarly, these calibrations are calculated for photons using $Z \rightarrow \ell\ell\gamma$. Systematic uncertainties that effect these calibrations include passive material between the interaction point and the EM calorimeter and pile-up [30].

CHAPTER 4. RECONSTRUCTION OF PHYSICS OBJECTS

Further ‘identification’ selections are used to improve electron and photon purity. Prompt electrons are identified with a likelihood discriminant which takes into account track parameters and electromagnetic shower properties. The primary electron track must stretch into the two inner pixel layers and hit multiple points in the silicon-strip detector. The likelihood discriminant is calculated from probability density functions formed by smoothing histograms of 13 discriminating variables with an adaptive kernel density estimator. These are calculated separately for both the likelihood that an event reconstructs a prompt electron (signal) or that it does not (background). These likelihoods are derived from $Z \rightarrow ee$ and $J/\psi \rightarrow ee$ events recorded in Run 2. A tag-and-probe method is used to evaluate this likelihood. One electron in each decay must satisfy strict Run 1 likelihood discriminant requirements while the other serves as a probe of the new likelihood discriminant. Three electron working points are derived, Loose, Medium, and Tight, each with lower efficiency and higher purity than the previous. Physics analyses use the working points optimized for their analysis. For the $H \rightarrow WW$ measurement we use ‘Medium’ reconstructed electrons. Figure 4.2 shows electron identification efficiency for each of the working points in a sample of $Z \rightarrow ee$ events where efficiency is calculated through comparisons to MC simulated $Z \rightarrow ee$ and $J/\Psi \rightarrow ee$ events. The average efficiencies for electroweak processes are 93%, 88% and 80%, respectively, for the Loose, Medium, and Tight operating points and gradually increase at high E_T [30].

Track hits and calorimeter deposits near reconstructed electrons and muons can bias energy, momentum, and position measurements. Isolation performance is defined for calorimeter clusters by E_T^{cone} , the sum of transverse energy within a cone ΔR , defined as $\sqrt{\Delta\eta^2 + \Delta\phi^2}$, near a photon or electron cluster after correcting for leakage and pile-up effects. Track isolation p_T^{cone} is defined as a sum of the transverse momentum of tracks within a cone about the electron track or interpolated photon track. For electrons the distance between nearby

CHAPTER 4. RECONSTRUCTION OF PHYSICS OBJECTS

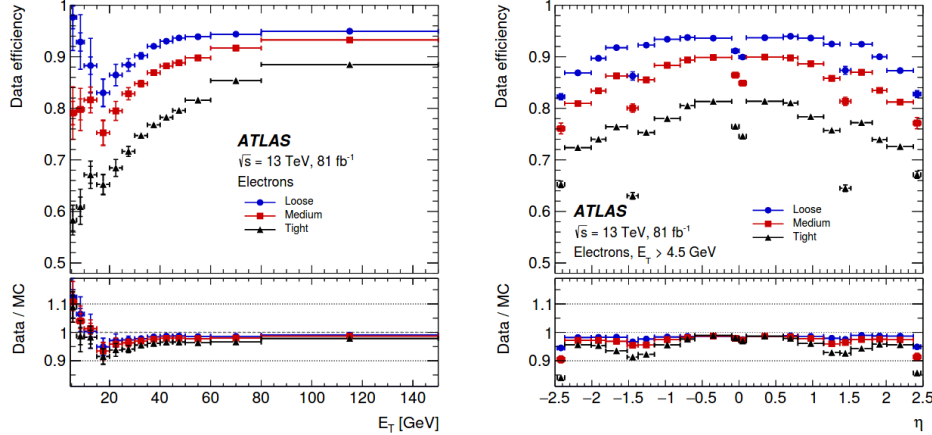


Figure 4.2: Electron reconstruction efficiency as a function of E_T (left) and η (right) in $Z \rightarrow ee$ events for Losse, Medium, and Tight electrons [30]

decay products is directly related to electron p_T so a variable cone size can be used such that

$$\Delta R = \min\left(\frac{10}{p_T}, \Delta R_{max}\right), \quad (4.1)$$

where ΔR_{max} is typically 0.2. Isolation working points strike a balance between efficiency and rejection of misidentified prompt electrons. Electron isolation for the $H \rightarrow WW^*$ analysis uses two different selections based on electron track p_T . The *IsoGradient* working point is used for $p_T > 25$ GeV. This requires calorimeter and track isolation about cones of $\Delta R = 0.2$ (*topoetcone20*, *ptvarcone20*). Electron isolation is changed to the fixed cut track cone isolation for $p_T < 25$ GeV to further eliminate fake background contributions. High efficiency at each working point requires cuts on E_T^{cone20} and $p_T^{varcone20}$ derived from $J\psi \rightarrow ee$ and $Z \rightarrow ee$ MC simulations. Isolation efficiencies for electrons are shown in Figure 4.3 for Medium identified electrons in $Z \rightarrow ee$ events. The Gradient working point delivers efficiency that is stable across η and is coupled with high background rejection of misidentified electrons [30].

Photon isolation is solely calorimeter-based. $Z \rightarrow \ell\ell\gamma$ events are used for photon isolation

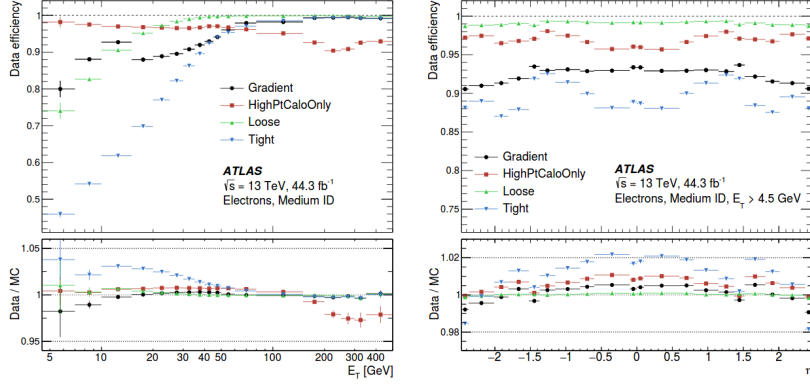


Figure 4.3: Electron isolation efficiency shown for four working points in $Z \rightarrow ee$ events as a function of E_T and η [30]

efficiency measurements and three working points are available which balance efficiency and background rejection just as in the electron case.

Electron reconstruction, calibration, identification, and isolation are all integral for the $H \rightarrow WW$ analysis in order to accurately identify electrons in the final state of candidate Higgs events. Systematic uncertainties from electron identification and isolation efficiency will be discussed further in later chapters and play a significant role in $H \rightarrow WW$ cross-section measurements.

4.3 Muons

Muons contribute to some of the most interesting physics analyses by the ATLAS collaboration including $H \rightarrow WW \rightarrow \ell\nu\ell\nu$ measurements, which require a muon in the final state. The Muon Combined Performance group (MCP) is tasked with producing the most accurate muon calibrations for physics analyses. This includes defining muon identification and isolation criteria and measuring efficiency as well as muon momentum scales and resolutions. Their goal is to create a number of “working points” tailored to different types of

CHAPTER 4. RECONSTRUCTION OF PHYSICS OBJECTS

physics analyses. The working points are continuously updated and improved before being tested and implemented on different analyses. My work with the MCP group has focused on applying corrections necessary for muon momentum scale and resolutionin simulation to match the data.

Muon reconstruction is performed independently using tracks reconstructed in the ID and MS and for combined tracks. This section will focus on reconstruction in the MS, which is particular to muons and the combined reconstruction, which uses information from both the ID and MS.

Muon reconstruction begins with a search for hit patterns in each MS subdetector, which are called segments. The middle of the MS typically exhibits the largest number of trigger hits, therefore tracks are built by working out from the center of the MS and connecting segments layer-by-layer. Criteria such as hit multiplicity and fit quality determine track acceptance. At least two segments are needed to build a track. Hits associated with each track candidate are fitted using a global χ^2 fit. A track candidate is accepted if it passes the selection criteria [29].

The combined ID-MS reconstruction uses different algorithms to find different *muon types*. There are four main types outlined below. When the same muon is reconstructed in more than one category, preference is given to Combined (CB), then Segment-tagged (ST), and finally Calorimeter Tagged (CT) muons. These algorithms have been continuously improved to increase precision, speed, and robustness against misidentification [31].

- **Combined muons (CB):** They combine tracks from the ID and MS detectors using a global refit on all hits (some may be removed or added to improve quality). Most muons are reconstructed using an outside-in method.
- **Segment-tagged muons (ST):** ST muons are assigned an ID track that is associated

CHAPTER 4. RECONSTRUCTION OF PHYSICS OBJECTS

with at least one local MDT or CSC track after extrapolation. These are used when muons cross only one layer of the MS because of low p_T or regions beyond most MS layer boundaries.

- **Calorimeter-tagged muons (CT):** These muons are identified by an ID track that can be matched to a minimum ionizing particle energy deposited in the calorimeter. They have the lowest purity but are optimized for $|\eta| < 0.1$ and $1.5 < p_T < 100$ GeV where the MS is only partially instrumented.
- **Extrapolated muons (ME):** They are reconstructed in the MS with the addition of silicon points and with a loose requirement that the muon track originated at the interaction point. In general, these muons are required to traverse $2 - 3$ layers of MS chambers. These are mainly used to extend acceptance in the region $2.5 < |\eta| < 2.7$, which is not covered by the ID.

In order to distinguish muons from other particles (like backgrounds from pion and kaon decays) strict quality requirements must be set to select prompt muons with high efficiency. Reconstruction targets W and Z decays (as opposed to light-hadron decays) which originate from the interaction point. We use the following variables to identify such muons:

- q/p significance, the absolute value of the difference between the ratio of the charge and momentum of muons in the ID and MS divided by the sum in quadrature of their corresponding uncertainties,
- ρ' , the absolute value of the difference between the p_T measurements in the ID and MS divided by the p_T of the combined components,
- χ^2 , the normalized fit parameter of the combined components

CHAPTER 4. RECONSTRUCTION OF PHYSICS OBJECTS

Specific requirements on the number of hits in the ID and MS assure that inefficiencies are as expected and momentum measurements are robust. There are four muon identification selections that each addresses specific needs of physics analyses [31].

- **Loose Muons:** The *Loose* criteria maximizes the reconstruction efficiency, losing very few potential muons, while providing satisfactory tracks. All muon types are used in this criteria.
- **Medium Muons:** *Medium* is the default selection for muons in ATLAS because it minimizes systematic uncertainties associated with reconstruction and calibration. Only CB and ME tracks are used with requirements for over 3 hits in at least two MDT layers in most regions. All *Medium* muons are included in the *Loose* criteria.
- **Tight Muons:** *Tight* selects muons with the highest purity but sacrifices efficiency. All *Tight* muons are included in the *Medium* selection, but only CB muons with at least two hits in the MS are considered, and the χ^2 value must be less than 8.
- **High- p_T Muons:** *High- p_T* muons have good momentum resolution for tracks with $p_T > 100$ GeV. This is beneficial to searches for high-mass Z' and W' resonances. CB muons in the *Medium* selection with at least 3 hits in 3 MS stations are included.

The $H \rightarrow WW$ analysis uses Tight muons with the added condition that $p_T > 15$ GeV and $\eta < 2.5$ to gain the highest purity possible and eliminate background from misidentified leptons, which constitute a significant background even with this selection.

We measure the muon reconstruction efficiency in two different ways in the regions $|\eta| < 2.5$ and $2.5 < |\eta| < 2.7$. First, in the barrel region, we use the tag-and-probe method. In this method we select an almost-pure sample of J/ψ and Z decays and require the leading

CHAPTER 4. RECONSTRUCTION OF PHYSICS OBJECTS

muon to be a *Medium* muon labeled the tag. The subleading muon, the probe, must be reconstructed independently. There are three types of probes:

- **ID track:** Allows measurement of MS efficiency and of tracks not accessible to CT muons.
- **CT tracks:** Allows measurement of MS efficiency and has powerful rejection of background (especially at low p_T). This is the most commonly used probe.
- **MS tracks:** Allows measurement of ID and CT efficiency.

To find the overall efficiency of *Medium*, *Tight*, or *High- p_T* muons, we multiply the efficiencies associated with each type of probe. The efficiency $\epsilon(X|CT)$ ($X = Medium / Tight / High-p_T$) of reconstructing these muons assuming a reconstructed ID track is measured using a CT muon as probe. This result is corrected by the efficiency $\epsilon(ID|MS)$ of the ID track reconstruction measured using MS probes.

$$\epsilon(X|ID) \cdot \epsilon(ID) = \epsilon(X|CT) \cdot \epsilon(ID|MS) \quad (X = Medium/Tight/High-p_T) \quad (4.2)$$

The ID track reconstruction efficiency must be independent from the muon spectrometer track reconstruction ($\epsilon(ID) = \epsilon(ID|MS)$). In addition, the use of a CT muon as a probe instead of an ID track must not affect the probability for *Medium*, *Tight*, or *High- p_T* reconstruction ($\epsilon(X|ID) = \epsilon(X|CT)$). These assumptions are largely true with simulations showing some small deviations. These deviations are taken into account when calculating systematic uncertainties.

The reconstruction efficiency of *Loose* muons is measured separately for CT muons within $|\eta| < 0.1$ and all other *Loose* types. The CT muon efficiency is measured using MS probe tracks, and the efficiency of other muons is evaluated similarly to the *Medium*, *Tight*, and

CHAPTER 4. RECONSTRUCTION OF PHYSICS OBJECTS

High- p_T muons using CT probe muons [31]. For $|\eta| > 2.5$, the efficiency is calculated using the ME muons in the **Loose** and **Medium** selections. The number of muons observed in this region is normalized to the number of muons observed in the region $2.2 < |\eta| < 2.5$. A more detailed discussion of the efficiency measurement in this region can be found in Ref. [32].

Scale factors are defined as the ratios between the efficiency of data and the efficiency of Monte Carlo simulations. They are used to describe the deviation between simulated and real detector behavior and are used in physics analyses to correct simulations.

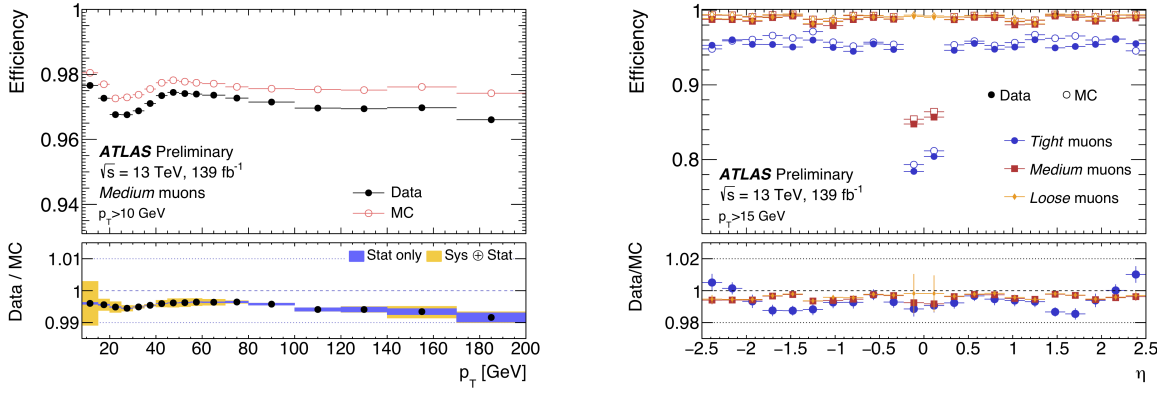


Figure 4.4: On the left, reconstruction efficiency for $Tight$ muons from $Z \rightarrow \mu\mu$ events is displayed as a function of the p_T of the muon in the region $0.1 < |\eta| < 2.5$ with systematic and statistical uncertainties. On the right, muon reconstruction efficiency is shown as a function of η in $Z \rightarrow \mu\mu$ events for muons with $p_T > 15$ GeV for *Medium*, *Loose* and *Tight* muons. In both plots the full 139 fb^{-1} Run 2 dataset is used [33].

Figure 4.4 displays reconstruction efficiency for *Medium* muons over a range of p_T and all other working plotted over η . While *Medium* muons have a higher efficiency than the *Tight* selection used in this analysis, both have an efficiency above 95% for a large range of η and p_T . The J/ψ decays probe low p_T muons while Z decays probe muons of a higher p_T allowing a large range to be defined. MC simulations match data within 1 – 2%. The only significant loss of efficiency is seen at extremely low η due to criteria excluding ID muons. Overall, the default *Tight* muon selection demonstrates reconstruction efficiency around 95%

CHAPTER 4. RECONSTRUCTION OF PHYSICS OBJECTS

for muons in our selection p_T range.

Isolation distinguishes muons from W/Z decays from those produced in the decay of b and c mesons. When heavy particles like W , Z , and Higgs bosons decay they often produce muons in isolation. Semileptonic decays of b and c hadrons, on the other hand, typically produce muons embedded in jets.

The MCP group uses two muon isolation variables: a track-based variable ($p_T^{varcone30}$) and a calorimeter-based variable ($E_T^{topocone20}$). The variable $p_T^{varcone30}$ is defined as the scalar sum of the transverse momenta of tracks with $p_T > 1$ GeV in a cone around the muon of transverse momentum p_T excluding the muon track itself. The cone size is p_T -dependent to improve the performance for muons produced in decays with a large transverse momentum. The variable $E_T^{topocone20}$ is defined as the sum of the transverse energy of topological clusters in a cone around the muon after subtracting the contribution from the deposited energy of the muon itself and correcting for pile-up effects [34].

Table 4.1 defines seven isolation selection criteria, called “isolation working points”, that optimize different physics analyses. The *LooseTrackOnly* and *FixedCutTightTrackOnly* working points are defined by cuts on the relative track-based isolation variable. All other working points are defined by cuts applied separately on both relative isolation variables. All cuts are tuned as a function of the η and p_T of the muon to obtain a uniform performance. The target efficiencies of the different working points are also described in Table ???. The efficiencies for the seven isolation working points are measured in data and simulation using the tag-and-probe method described previously. Figure 4.5 shows the isolation efficiency measured for *Medium* muons in data and simulation as a function of the muon p_T for two different working points. In both the *GradientLoose* and *FixedCutTightTrackOnly* working points, the efficiency is above 90% and matches simulation well within uncertainties for higher p_T muons. In the *HWW* analysis, fixed isolation cuts are optimized independent of Muon Per-

CHAPTER 4. RECONSTRUCTION OF PHYSICS OBJECTS

formance working points. Only muons with $p_T > 15$ GeV are considered so the efficiency is optimized for muons which pass this and the *Tight* selection cuts.

Isolation WP	Discriminating variable(s)	Definition
<i>LooseTrackOnly</i>	$p_T^{\text{varcone}30}/p_T^\mu$	99% efficiency constant in η and p_T
<i>Loose</i>	$p_T^{\text{varcone}30}/p_T^\mu, E_T^{\text{topocone}20}/p_T^\mu$	99% efficiency constant in η and p_T
<i>Tight</i>	$p_T^{\text{varcone}30}/p_T^\mu, E_T^{\text{topocone}20}/p_T^\mu$	96% efficiency constant in η and p_T
<i>Gradient</i>	$p_T^{\text{varcone}30}/p_T^\mu, E_T^{\text{topocone}20}/p_T^\mu$	$\geq 90(99)\%$ efficiency at 25 (60) GeV
<i>GradientLoose</i>	$p_T^{\text{varcone}30}/p_T^\mu, E_T^{\text{topocone}20}/p_T^\mu$	$\geq 95(99)\%$ efficiency at 25 (60) GeV
<i>FixedCutTightTrackOnly</i>	$p_T^{\text{varcone}30}/p_T^\mu$	$p_T^{\text{varcone}30}/p_T^\mu < 0.06$
<i>FixedCutLoose</i>	$p_T^{\text{varcone}30}/p_T^\mu, E_T^{\text{topocone}20}/p_T^\mu$	$p_T^{\text{varcone}30}/p_T^\mu < 0.15, E_T^{\text{topocone}20}/p_T^\mu < 0.30$

Table 4.1: The seven isolation working points are described by their discriminating variables and defining criteria [31].

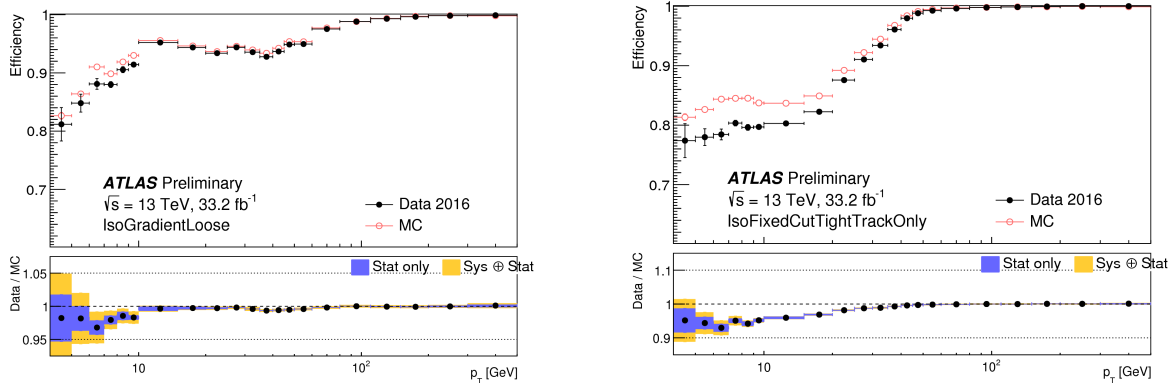


Figure 4.5: Isolation efficiency for the GradientLoose (left) and FixedCutTrackOnly (right) muon isolation working points. The efficiency is displayed as a function of p_T in $Z \rightarrow \mu\mu$ events. The black markers show efficiency measured in data samples while the red show MC simulations. The bottom panel shows the ratio of the efficiency between the two as well as both statistical and systematic uncertainties [35].

The isolation cuts used by the $H \rightarrow WW$ analysis are $p_T^{\text{varcone}30}/p_T < 0.06$ and $p_T^{\text{topocone}20}/p_T < 0.09$ which are relatively tight selections and designed to reduce misidentified lepton backgrounds.

CHAPTER 4. RECONSTRUCTION OF PHYSICS OBJECTS

The muon momentum scale and resolution are studied using Z and J/ψ decays. In order to obtain agreement between simulation and data in muon momentum scale on the order of 10^{-3} and in resolution to the percent level, we need to apply a set of corrections to the simulated muon momentum. After applying the corrections we validate them by comparing the muon momentum scale and resolution between simulation and data over η , ϕ , and p_T .

We extract the calibration parameters with the transverse momentum of the ID and MS components of a CB track. The corrected transverse momentum is described by the following equation:

$$p_T^{\text{Cor,Det}} = \frac{p_T^{\text{MC,Det}} + \sum_{n=0}^1 s_n^{\text{Det}}(\eta, \phi)(p_T^{\text{MC,Det}})^n}{1 + \sum_{m=0}^2 \Delta r_m^{\text{Det}}(\eta, \phi)(p_T^{\text{MC,Det}})^{m-1} g_m}. \quad (4.3)$$

Here the g_m terms are normally distributed random variables with zero mean and unit width. The Δr and s terms describe momentum resolution smearing and scale corrections applied in specific detector regions, respectively. Both the ID and MS are divided into 18 pseudorapidity regions and the MS is divided into two ϕ bins separating the large and small sectors. Each of these bins leverages different alignment techniques and has different material distributions.

There are two s terms that represent different types of corrections. The variable s_1 corrects for inaccuracy in the description of the magnetic field integral and the detector in the direction perpendicular to the magnetic field. The variable s_0 corrects for the inaccuracy in the simulation of energy loss in the calorimeter and other materials. Since this loss is negligible in the ID, it is only nonzero in the MS [31].

The denominator introduces momentum smearing which broadens the p_T resolution in

CHAPTER 4. RECONSTRUCTION OF PHYSICS OBJECTS

simulation. The parametrization of the smearing is defined as

$$\frac{\sigma(p_T)}{p_T} = r_0/p_T \oplus r_1 \oplus r_2 \cdot p_T. \quad (4.4)$$

In this equation r_0 is related to the fluctuations in energy loss in the traversed material, r_1 accounts for multiple scattering, local magnetic field inhomogeneities, and local radial displacements of hits, and r_2 describes intrinsic resolution effects caused by the spatial resolution of the hit measurements and by residual misalignment of the MS [31]. Correction parameters are extracted from data using a binned maximum-likelihood fit with templates derived from simulation which compares the invariant mass distributions for J/ψ and Z decay candidates in data and simulation. The muons are carefully selected to be compatible with tracks that start at the interaction point and penetrate both the ID and the MS. Muons are also selected to pass specific momentum and isolation criteria. The dimuon mass distribution of these tracks in data is fitted using a Crystal Ball function¹ convoluted with an exponential background distribution in the ID and MS fits. The background model and its normalization are then used in the template fit. The fits are performed in $\eta - \phi$ regions of fit (ROFs) which comprise regions with uniform features in the ID and MS [31].

From these fits, we can find the smearing terms across all η regions. Once the corrections are applied, the agreement between data and MC is excellent. This is shown in Figure 4.6. The parameter r_0 is set to zero across all η regions since energy loss is negligible in the ID. The parameters r_1 and r_2 increase as η increases since spatial resolution decreases and inhomogeneities increase as we move from the barrel to endcap regions of both the ID and MS. Muon momentum corrections are continuously studied during ATLAS runs to validate

¹The Crystal Ball function is a probability density function named for the Crystal Ball detector collaboration operating on the SPEAR accelerator. It is composed of a Gaussian core and power-law low-end tail [36].

CHAPTER 4. RECONSTRUCTION OF PHYSICS OBJECTS

muon calibration performance and account for discrepancies.

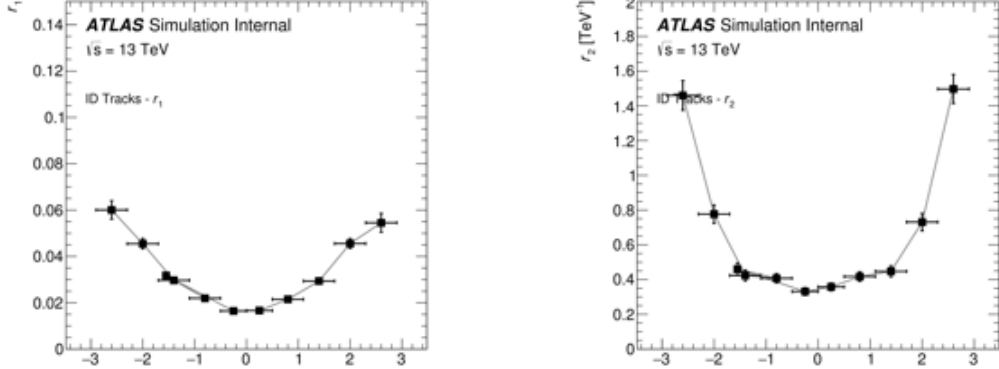


Figure 4.6: The r - values from each of 10 fits of resolution to p_T for ID muon simulations are shown. Each value corresponds to a particular ROF or η region. These plots show r_1 (left) and r_2 (right) as functions of leading muon η .

4.4 Jets

Quarks and gluons emitted from high-energy hard scattering do not appear in the detector directly. Quarks and gluons with high enough energye radiate low energy gluons until partons are able to bind into color-neutral hadrons. These hadrons are collimated in groups as “jets”. Jet energy and momentum are used in physics analyses as proxies for initial scattered partons. Pile-up presents the main difficulty in jet calibration as multiple interactions occuring in the detector at once create significant, often hadronic, background. The hard interaction of interest must be separated from pile-up background, which is most often soft. During Run 1, the ATLAS experiment reconstructed jets using either only the calorimeter or the tracker, though most often the calorimeter. Topological clusters of calorimeter cells (topo-clusters) were used to trace jet tracks. At the end of Run 1, the jet energy scale (JES) correction factor used to calibrate jets to the particle level was re-calculated using additional track

CHAPTER 4. RECONSTRUCTION OF PHYSICS OBJECTS

information from the Inner Detector and Muon Spectrometer, which greatly improved jet resolution [37].

In Run 2, a new algorithm for jet reconstruction took advantage of the improvements shown in Run 1 by including information from the tracker. ‘Particle flow’ uses the tracker’s higher momentum resolution for low-energy charged particles and its greater angular resolution of single charged particles. This is complemented by the calorimeter’s ability to reconstruct both charged and neutral particles and the calorimeter’s higher energy resolution for high energy physics objects. The calorimeter also has an extended acceptance so in the forward region only calorimeter topo-clusters are used. One potential difficulty with the ‘particle flow’ algorithm is the possibility for double counting particles if the jets reconstructed by the tracker are not properly matched with the corresponding calorimeter signals. This is avoided in the algorithm through the condition that if a particle’s track measurement is used, its corresponding energy must be subtracted from the calorimeter measurement. The success of the algorithm in removing only energy deposits from the tracked jet represents a key criteria for its overall performance [38].

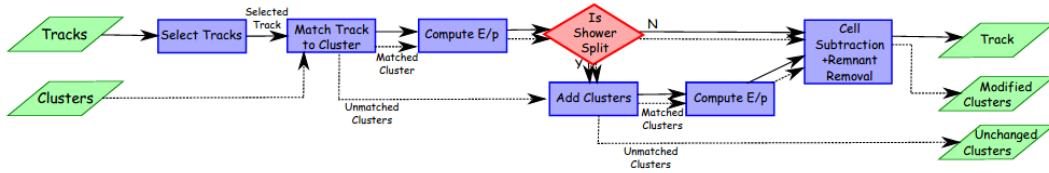


Figure 4.7: Flow chart of the particle flow algorithm beginning with track selection and ending with charged particles and changed/unchanged topo-clusters [38].

Topo-clusters are described by two main properties - ϵ , which represents the fraction of true energy deposited in the cluster out of the total true energy deposited in all topo-clusters for that object, and ρ , the fraction of a particle’s true energy which lies within the topo-cluster. High ρ , high ϵ topo-clusters allow contributions from different particles to be

CHAPTER 4. RECONSTRUCTION OF PHYSICS OBJECTS

distinguished and so are easier to apply hadronic shower subtraction [38].

Jet tracks need to meet strict criteria. In this analysis, tracks included in jets are required to satisfy the “tight” selection criteria, which includes requirements for at least nine hits in silicon detectors, no missing Pixel hits, $\eta < 2.5$, and $40 > p_T > 0.5$ GeV. High p_T tracks are excluded because of their poor isolation. In addition, tracks which are identified as electrons or muons are excluded [38].

With topo-clusters and tracks assembled, the algorithm matches each to one another. Topo-clusters are ranked through the distance metric

$$\Delta R' = \sqrt{\left(\frac{\Delta\phi}{\sigma_\phi}\right)^2 + \left(\frac{\Delta\eta}{\sigma_\eta}\right)^2}, \quad (4.5)$$

where σ_ϕ and σ_η denote angular topo-cluster widths. A requirement that $E^{clus}/p^{trk} > 0.1$ is applied so that the energy of the topo-cluster must contain a significant portion of the energy of the track. This requirement rejects about 30 – 40% of the incorrect topo-clusters at $p_T > 5$ GeV. The closest topo-cluster to each track in $\Delta R'$ is taken to be the correct match. If no topo-cluster is within a cone of $\Delta R' = 1.64$, it is assumed that the particle did not form a topo-cluster in the calorimeter [38].

Topo-clusters are thus matched to particle tracks, and the energy deposited by the particle is subtracted from the calorimeter energy. The average energy deposited by a particle with momentum p^{trk} is $\langle E_{dep} \rangle = p^{trk} \langle E_{ref}^{clus} / p_{ref}^{trk} \rangle$, where $\langle E_{ref}^{clus} / p_{ref}^{trk} \rangle$ is calculated using single-particle samples without pile-up by summing topo-cluster energies within $\Delta R = 0.4$ about the track position. These are calculated at varying p_T and η values to capture effects from detector geometry and shower development. Particles often split their energy between multiple topo-clusters and this split can be determined through the significance of the difference between expected energy and that of the matched topo-cluster. This new full set of

CHAPTER 4. RECONSTRUCTION OF PHYSICS OBJECTS

matched clusters is considered for energy subtraction [38].

Energy subtraction is performed cell-by-cell unless $\langle E_{dep} \rangle$ is greater than the energy of the total matched topo-clusters, in which case they are all removed. Rings are formed in (η, ϕ) about the extrapolated track and are one calorimeter cell wide. The average energy density in each ring is computed and the ring with the highest energy density is subtracted first. This continues to lower density rings until $\langle E_{dep} \rangle$ is reached. Finally, energy clusters from shower fluctuations are removed. Ideally now the sum of selected tracks and remaining topo-clusters together represent the reconstructed event without double counting. An example display of particle flow events is shown in Figure 4.8

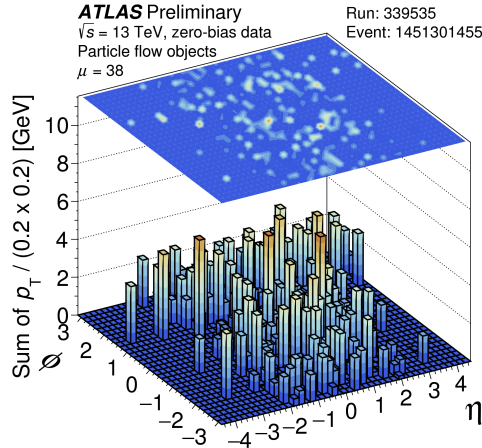


Figure 4.8: Sum of transverse momenta of neutral and charged particle flow objects in an area $\Delta\eta \times \Delta\phi = 0.2 \times 0.2$ from a 2017 event with mean number of interactions per beam crossing $\mu = 38$ [39]

Jet-finding algorithms aim to approximate the hadrons that generate calorimeter and track-based jets in the detector. They bridge the divide between observable jet objects and theoretical predictions from QCD. There are several jet algorithms in use currently and all are collinear and infrared safe. This means that neither splitting a jet collinearly nor soft emissions should change jet structure. Without these properties perturbation theory diverges

at high orders.

Anti- k_t is the jet algorithm used by ATLAS and is infrared collinear safe by construction and resilient to soft radiation [40].

Jet reconstruction and isolation does not end with particle flow and the anti- k_t algorithm. Further corrections have to be applied to improve the agreement between data and MC simulations. MC simulation are calibrated to better model pile-up and to improve jet angular resolution. Global sequential calibrations are calculated with MC using calorimeter, track, and muon chamber information to improve jet resolution. Data is used to constrain uncertainties with through known dijet samples. These calibrations lead to final measurements of jet energy scale (JES) and jet energy resolution (JER) and provide reconstructed jet events in MC and data as well as a number of recommended uncertainties for physics analyses. Figure 4.9 shows jet energy scale and resolution as a function of p_T for PFlow jets modeling with the anti- k_t algorithm after JES corrections are applied. Fully combined systematic uncertainties are also shown [41].

Jet reconstruction and calibration are crucial to this analysis and later chapters will detail how impactful jet energy scale and resolution uncertainties are to the overall precision of the $H \rightarrow WW$ cross-section measurement.

4.5 Missing transverse energy

Colliding protons in collider experiments like ATLAS have momentum solely in the plane of the beam. Conservation of momentum implies that in the plane transverse to the beam ($x - y$) the sum of momentum from all interaction by-products is zero. This is most often not the case and the non-zero transverse momentum from any interaction is termed E_T^{miss} . Missing transverse energy is a sign of final state neutrinos and could point to new particles

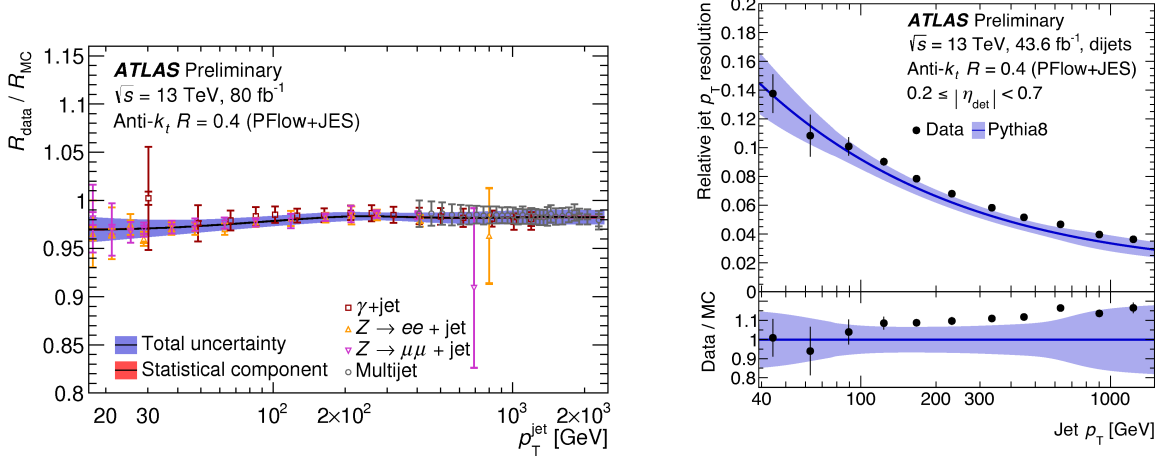


Figure 4.9: Left: data-to-simulation ratio for average jet p_T as a function of jet p_T . Three techniques shown as well as their their combination (black) and the combination total uncertainty. PFlow anti- k_t jets with $R=0.4$ and JES correction. Right: relative jet energy resolution as a function of p_T for anti- k_t Pflow jets with $R = 0.4$ in 2017. JES calibrations applied and compared to MC with full systematic uncertainties [39].

that cannot be directly detected, like neutralinos or dark matter particles. E_T^{miss} could also signify interacting particles which evade detection in ATLAS due to detector acceptance or poor reconstruction [42].

Missing transverse energy is determined using a combination of all reconstructed particles in an event. This is challenging because it involves all detector components and final particle types. The Jet/ E_T^{miss} performance group delivers calibrations for multiple E_T^{miss} variables that we use in the $H \rightarrow WW$ analysis. This section will discuss E_T^{miss} reconstruction and performance followed by definitions of a few additional E_T^{miss} observables. Reconstructed E_T^{miss} calculations take into account both *hard* and *soft* event signals. Hard-events are composed of fully reconstructed and calibrated particles like electrons, muons, photons, τ -leptons and jets. All other objects are considered *soft*. Reconstruction for all particle types happens independently, which means that the same signal may be used to identify two distinct particles. This double-counting is taken into account in the E_T^{miss} resolution

CHAPTER 4. RECONSTRUCTION OF PHYSICS OBJECTS

estimation. At its most basic, E_T^{miss} is defined:

$$E_{x(y)}^{miss} = - \sum_{i \in \text{hard objects}} p_{x(y),i} - \sum_{j \in \text{soft objects}} p_{x(y),j} \quad (4.6)$$

where overall E_T^{miss} is a vector composed of x, y components. In order to avoid double-counting the same detector signal in multiple particle reconstruction algorithms, hard objects are considered in order: electrons, photons, hadronically decaying τ -leptons, and then jets. Muons have little overlap since they are reconstructed using MS and ID tracks (and muons alone leave tracks in the MS). As particles are reconstructed in this sequence, signals used more than once are rejected to avoid overlap. Another key variable is $\sum E_T$ which is defined

$$\sum E_T = \sum_{\text{electrons}} p_T^e + \sum_{\text{photons}} p_T^\gamma + \sum_{\tau\text{-leptons}} p_T^\tau + \sum_{\text{muons}} p_T^\mu + \sum_{\text{jets}} p_T^{jet} - \sum_{\text{unused tracks}} p_T^{track} \quad (4.7)$$

The first five terms show the hard term while the last represents the soft-term. Selections are applied to reconstructed jets and particles to achieve optimal E_T^{miss} for a particular analysis [43]. In the context of $H \rightarrow WW$ we use a “tight” configuration for E_T^{miss} classified by strict conditions on accepted jets. This working point has the greatest pile-up rejection, which is integral to our analysis.

E_T^{miss} reconstruction contains the complexity of each of its component parts, and all their p_T resolutions affect the total E_T^{miss} resolution. Pile-up and total event activity also play a large role in E_T^{miss} performance. Validations for E_T^{miss} are performed on a variety of observables and MC modeling is compared to reconstructed data. Systematic uncertainties are derived from comparing the reproducibility of these observables and their successful modeling of data. Resolution for reconstructed jets and leptons are also propagated to overall E_T^{miss} uncertainty. E_T^{miss} performance is evaluated using $Z \rightarrow \mu\mu$, $Z \rightarrow e^-e^+$, and $W \rightarrow e\nu$ events, the first two with no genuine E_T^{miss} and the third with significant E_T^{miss} from neutrinos. After

CHAPTER 4. RECONSTRUCTION OF PHYSICS OBJECTS

specific event selection and E_T^{miss} reconstruction, E_T^{miss} for each of these samples is studied and data and MC are demonstrated to match within uncertainties. Selected performance observables are shown for the full Run 2 dataset in 4.10. Here $Z \rightarrow e^+e^-$ reconstructed track-based soft term E_T^{miss} and E_T^{miss} significance distributions are shown. Data and MC show good agreement.

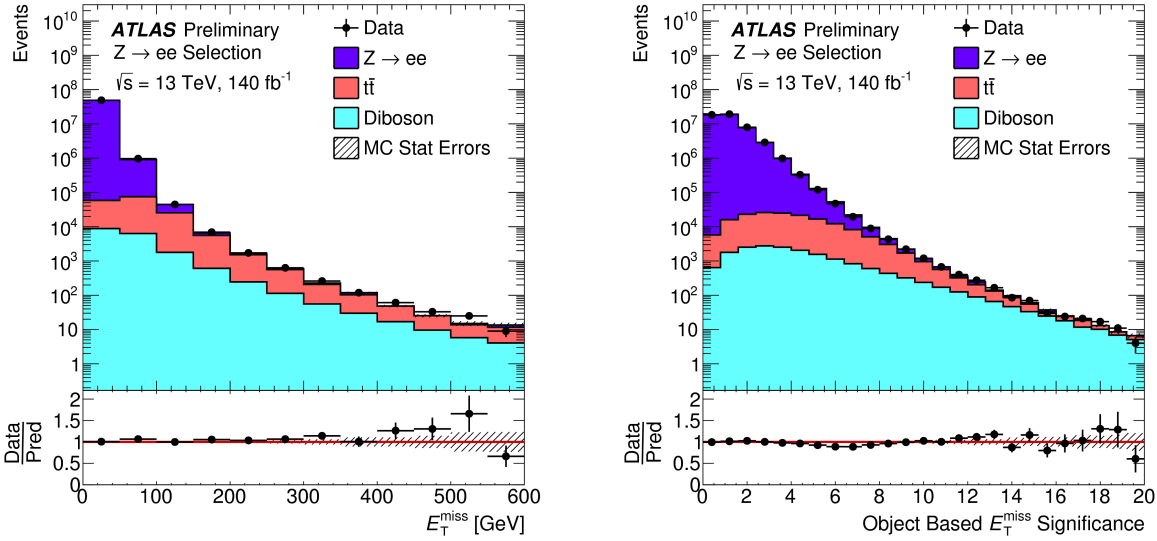


Figure 4.10: Left: Track-based Soft Term E_T^{miss} shown for the complete Run 2 dataset with an integrated luminosity of 140 fb^{-1} . Monte Carlo simulations are compared to data for the tight E_T^{miss} working point. Right: Track-based Soft Term E_T^{miss} significance modeling shown in the tight E_T^{miss} working point [39]

In this analysis, a number of E_T^{miss} variables are used. These variables are used to reject backgrounds particularly from $Z \rightarrow \tau\tau$ events. Some of the variables used for these selections include track-based E_T^{miss} , track-based soft term E_T^{miss} , $m_{\tau\tau}$, E_T^{miss} significance and p_T^{tot} . The E_T^{miss} soft term is composed of a track-based and calo-based component. The calorimeter-based component is highly dependent on pile-up and so using a track-based soft term reduces overall pile-up dependence. Track-based E_T^{miss} uses only reconstructed ID tracks from the primary vertex and in our analysis this has been just as powerful discriminant for isolating

CHAPTER 4. RECONSTRUCTION OF PHYSICS OBJECTS

$Z \rightarrow \tau\tau$ background events from the VBF signal as overall E_T^{miss} without the same pile-up dependence and correlation with other kinematic variables. The E_T^{miss} significance is a newly defined and recommended variable from the Jet/ E_T^{miss} group. Described further in Ref. [42], it discriminates real missing energy from momentum resolution effects using a calculated likelihood. Shown in Figure 4.10, the E_T^{miss} significance peaks at low values if E_T^{miss} likely comes from resolution effects and not from a real invisible particle in the event. Our analysis defines two additional variables based on E_T^{miss} : p_T^{tot} describes the total transverse momentum from all hard objects in the event, and $m_{\tau\tau}$, defined as

$$m_{\tau\tau} = \frac{m_{\ell\ell}}{\sqrt{x_1 x_2}}, \quad (4.8)$$

where

$$\begin{aligned} x_1 &= \frac{p_x^{\ell 0} p_y^{\ell 1} - p_y^{\ell 0} p_x^{\ell 1}}{p_y^{\ell 1} E_{Tx}^{miss} - p_x^{\ell 1} E_{Ty}^{miss} + p_x^{\ell 0} p_y^{\ell 1} - p_y^{\ell 0} p_x^{\ell 1}}, \text{ and} \\ x_2 &= \frac{p_x^{\ell 0} p_y^{\ell 1} - p_y^{\ell 0} p_x^{\ell 1}}{p_x^{\ell 1} E_{Ty}^{miss} - p_y^{\ell 0} E_{Tx}^{miss} + p_x^{\ell 0} p_y^{\ell 1} - p_y^{\ell 0} p_x^{\ell 1}} \end{aligned} \quad (4.9)$$

Each of these variables contributes to our signal region selection and elimination of background. A number of systematic uncertainties from reconstructed E_T^{miss} are defined and used in our analysis, though these are small compared to the uncertainties from jets and other final state particles.

In this chapter, I have outlined the procedures for building all the physics objects we use in the $H \rightarrow WW$ analysis. The next chapters will use these physics objects and their kinematic variables to understand our background and signal events.

Chapter 5

Event Selection

This chapter steps through some of the object definitions and inputs used in the analysis. First, the data and Monte Carlo simulations used for signal and background modeling are summarized. Then, the kinematic variables and observables used in event selection and later for the fiducial cross-section measurement are defined. Finally, the signal selection is outlined and its results shown. I played a primary role in testing and optimizing the analysis selection using reconstructed events.

5.1 Data and Monte Carlo samples

5.1.1 Data samples

The full Run 2 dataset containing all the proton-proton collision data collected from 2015–2018 at $\sqrt{s} = 13$ TeV with a 25 ns bunch spacing configuration are used.

In 2015, 2016, 2017, and 2018, 3.86 fb^{-1} , 35.6 fb^{-1} , 46.9 fb^{-1} , and 62.2 fb^{-1} of luminosity were recorded, respectively. Peak instantaneous luminosity increased from $5.0 \times 10^{33}\text{ cm}^{-2}\text{s}^{-1}$ in 2015 to $21.4 \times 10^{33}\text{ cm}^{-2}\text{s}^{-1}$ in 2018. Average (peak) pile-up also increased from $\langle\mu\rangle = 13.6$

(40.5) in 2015 to $\langle \mu \rangle = 37.0$ (90) in 2018. These pile-up distributions datasets are shown in Figure 5.1.

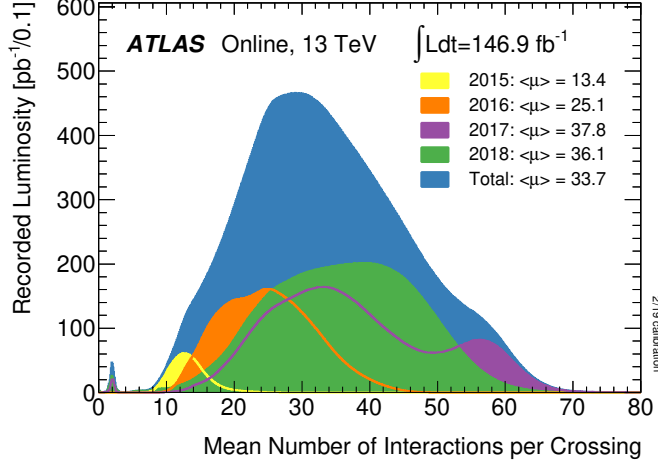


Figure 5.1: The luminosity-weighted distribution of the mean number of interactions per crossing is shown for Run 2 pp collision data [44].

Events are only used if all relevant detector components are operating normally. These events are part of the standard “All Good” Good Run List comprising a total integrated luminosity of 139 fb^{-1} and data quality efficiency of 91.5%.

Throughout Run 2, the instantaneous luminosity and pile-up changed over time. This is accounted for in our MC modeling, as described in the next section.

5.1.2 Monte Carlo samples

Monte Carlo samples are generated to compare to data in order to test Standard Model predictions and search for discrepancies. These simulations are also used to optimize the analysis selection criteria. Monte Carlo events are fully simulated using the ATLAS detector simulation in the GEANT4 framework [45] and reconstructed with standard ATLAS reconstruction software. Pile-up is simulated as additional pp interactions in a separate simulation

CHAPTER 5. EVENT SELECTION

step during digitization where minimum bias events are superimposed on the simulated signal events. These additional events are added based on that year’s recorded pile-up to account for dataset differences.

Separate programs are used to generate the hard scattering process and to model the parton showering (PS), hadronization, and the underlying event (UE). The next sections summarize the simulation techniques for our signal VBF samples, other Higgs production modes, and relevant backgrounds.

The data is split into three time-based categories. Data-taking conditions in 2015 and 2016 are averaged and described together as MC16a. The 2017 and 2018 data-taking conditions are considered separately as MC16d and MC16e, respectively.

Vector boson fusion Higgs samples

VBF Higgs events are generated through POWHEG [46] interfaced with PYTHIA8 with the PDF4LHC15 parton distribution function (PDF) set [9]. Cross-sections are calculated with full NLO QCD and EW corrections [47, 48] with an approximate NNLO QCD correction applied [49]. These cross-sections as well as associated branching ratios are calculated by the LHC Higgs Cross Section Working Group Yellow Report 4 [8]. Generated events are normalized to the calculated cross-sections.

Other production mode Higgs samples

Other Higgs production modes are considered in the analysis including gluon fusion (ggF), associated Higgs boson production (VH , $V = W, Z$), and Higgs boson production in association with a heavy quark pair (ttH). Though only ggF has an appreciable yield in the signal region, each of these are studied and considered in the analysis. As in VBF Higgs sample, ggF, VH , and ttH are produced with PYTHIA8 [50, 51] for decay, parton shower,

hadronization and multiple parton interactions.

Background samples

Standard Model backgrounds include events from production of dibosons, top-quark, Z +jets, W +jets and multijets. The WW samples are generated using SHERPA 2.2.2 interfaced with NNPDF3.0 NNLO PDFs. The production of Z +jets (or Drell-Yan) is simulated with SHERPA 2.2.1 using the NNPDF3.0 NNLO PDFs with dedicated parton shower tuning developed by Sherpa authors. Top-quark pair production ($t\bar{t}$) is simulated using POWHEG with the Powheg-Box framework using the NNPDF 3.0 PDFs and interfaced with PYTHIA 8 using NNPDF 2.3 PDFs for parton showering. Single top, mainly Wt , production is generated with POWHEG-Box 2.0 interfaced to PYTHIA 6.428 for parton showering. The productions of $Z\gamma$ and $W\gamma$ are modeled using SHERPA 2.2.2 at the NLO accuracy for 0- and 1-jet. The W +jets process modeling is based on a data-driven method described in the next chapter. MC samples (with the same MC generators for both W +jets and Z +jets samples) are used to validate the fake estimation and estimate sample composition uncertainties. These processes are generated with POWHEG MiNLO interfaced to PYTHIA 8 with the AZNLO tune.

5.2 Object definitions

This analysis utilizes a number of calibrated physics objects and the accurate use of each determines the precision of our $H \rightarrow WW$ cross-section measurement. Lepton, jet, and missing transverse energy reconstruction, isolation, and calibration were described in the Chapter 4. This chapter focuses on the particular parameters applied for these physics objects in this analysis. The object definitions are used in accordance with the $H \rightarrow WW$

CHAPTER 5. EVENT SELECTION

coupling analysis for consistency where optimization focussed on $H \rightarrow WW$ measurements at large. Finally, further observables used in event selection are defined and described here as well.

5.2.1 Lepton

Our choice of lepton identification algorithm impacts both the rejection of fake lepton backgrounds ($W+jets$) and QCD background. Tighter requirements on lepton identification decrease signal efficiency so the optimal criteria balance high signal efficiency and high background rejection.

Overall, all events must have at least two leptons tracks and each lepton track must have $p_T > 400$ MeV. Further, leptons are all required to originate at the hard-scatter primary vertex, which is defined as the primary vertex with the largest track $\sum p_T^2$. Leptons must pass two impact parameter selections to ensure they originate at the primary vertex. The longitudinal impact parameter of each lepton track is defined as $|z_0 \sin \theta|$ where z_0 is the impact parameter and θ the track angle. Each lepton longitudinal impact parameter must be less than 0.5 mm. The significance of the transverse impact parameter is calculated with respect to the beam line ($|d_0|/\sigma_{d_0}$) and has a requirement of three (five) for muons (electrons), as recommended by the Muon and E/ γ combined performance groups.

Electron

This analysis uses both the *Medium* and *Tight* identification selections which have 94% and 88% identification efficiency, respectively, for an electron with $E_T = 100$ GeV. Electrons with $E_T > 25$ GeV must pass the *Medium* identification while those with $15 < E_T < 25$ GeV are required to pass the *Tight* selection. This selection is the same used in the $H \rightarrow WW$

CHAPTER 5. EVENT SELECTION

coupling analysis where optimization studies demonstrated its impact on overall significance.

Electrons are identified in the range $|\eta| < 2.47$, where the transition region between barrel and endcaps in the LAr calorimeter ($1.37 < |\eta| < 1.52$) is excluded.

Electron isolation uses two different selections based on electron track p_T . The *IsoGradient* working point is used for $p_T > 25$ GeV. This requires calorimeter and track isolation about cones of $\Delta R = 0.2$ (*topoetcone20*, *ptvarcone20*). Electron isolation is changed to the fixed cut track cone isolation for $p_T < 25$ GeV to further eliminate fake background contributions. These require both track and calorimeter variables to fall below the p_T dependent $0.1143 \times p_T + 92.14$.

Table 5.1 summarizes electron selection criteria.

Table 5.1: Electron selections

p_T range	$ \eta $ range	Electron ID	Isolation	Impact parameter
< 25 GeV	0 – 1.37, 1.52 – 2.47	Tight	FixedCutTrackCone40	$ z_0 \sin \theta < 0.5$, $ d_0 /\sigma_{d_0} < 5$
> 25 GeV		Medium	IsoGradient	

Muon

As described previously, muons can be reconstructed using inner detector tracks, calorimeter deposits, and muon spectrometer tracks. Muons in this analysis must fit the *Tight* selection as well as pass $p_T > 15$ GeV and $|\eta| < 2.5$. Muon identification and isolation criteria match those used in the $H \rightarrow WW$ coupling analysis and optimize background rejection and signal efficiency. Muon isolation uses calorimeter and track isolation with a cone of $\Delta R = 0.2$ (*topoetcone20*, *ptvarcone20*). Muon selection criteria are summarized in Table 5.2.

CHAPTER 5. EVENT SELECTION

Table 5.2: Muon selections

p_T range	$ \eta $ range	Muon ID	Calo Isolation	Track Isolation	Impact parameter
$> 15 \text{ GeV}$	< 2.5	Tight	$E_T^{\text{cone}20}/p_T < 0.09$	$p_T^{\text{varcone}30}/p_T < 0.06$	$ z_0 \sin \theta < 0.5, d_0 /\sigma_{d_0} < 3$

5.2.2 Jets

Jets constitute an important part of the analysis both in their number and characteristics. Our signal region selection and most control regions require at least two jets. In order to estimate and reject ggF Higgs background events, regions with less than two jets are also studied. “Tagging” jets refer to those considered in our jet requirement, though others may be defined. As detailed in Section 4.4, jets reconstruction uses the anti- k_t algorithm to create jet tracks from calorimeter deposited energy within a cone of $R = 0.4$, and this analysis uses particle flow jet reconstruction.

Jets are required to have $p_T > 30 \text{ GeV}$ to eliminate high potential for pile-up jets in the full η range, $|\eta| < 4.5$. “Jet vertex tagger” variables suppress pile-up events through combinations of multiple variables into a single jet tagger. For jets with $p_T < 60 \text{ GeV}$ and $|\eta| < 2.4$, the JVT variable is required to be larger than 0.59. In the forward region, a designated tagger called “fJVT” ought to be applied. However, the current analysis does not include this requirement, leading to more jet pile-up than expected.

The VBF signal region contains an additional jet observable, the central jet veto (CJV), which rejects events with additional jets (other than the two “tagged” jets) with $p_T > 20 \text{ GeV}$ within the rapidity gap between two leading jets. This veto increases VBF sensitivity through removal of hadronic backgrounds.

***b*-tagged jet**

The Jet/ E_T^{miss} group provides tools to identify jets formed from bottom quarks. While the previous HWW analysis [15] used the MV2C10 jet tagging algorithm, the current analysis utilizes the DL1 tagger. Both tools use jet kinematics, impact parameters, and secondary vertex variables as input to machine learning classifiers. The DL1 tagger uses a neural network training method (the MV2C10 a boosted decision tree) trained with $t\bar{t}$ signal to discriminate b -quarks from light and c -quarks. The DL1 tagger shows greater b -veto efficiency in isolating top background events and so is used in this analysis.

5.2.3 Missing transverse energy

Missing transverse energy is used to both suppress background and build other variables used in signal selection like m_{tt} and p_T^{tot} . The E_T^{miss} definitions and calculations are explained in Section 4.5. This analysis uses the “Tight” E_T^{miss} working point which has proven the most robust against increasing pile-up.

5.2.4 Overlap removal

Overlap removal is applied to electrons, muons, and jets following the latest algorithm recommended by the Analysis Software Group (ASG). Current removal steps can be summarized as followed:

- If a muon and electron share an ID track the electron is removed and if a calo-tagged muon shares an ID track with an electron, the muon is removed.
- If $\Delta R(\text{jet}, e) < 0.2$ the jet is removed to eliminate overlap with the nearby electron. The electron is removed if $\Delta R(\text{jet}, e) < \min(0.4, 0.04 + 10 \text{ GeV}/p_T^e)$.

- If $\Delta R(\text{jet}, \mu) < 0.2$ and the jet has less than three associated tracks with $p_T > 500$ MeV the jet is removed. The jet is also removed if the p_T ratio of the muon and jet is larger than 0.5 and the ratio of the muon p_T and the sum of the p_T of all jet tracks with $p_T > 500$ GeV is larger than 0.7. The muon is removed if $\Delta R(\text{jet}, \mu) < \min(0.4, 0.04 + 10 \text{ GeV}/p_T^\mu)$ for any surviving jets.

5.3 Common Observables

Dedicated observables are used in this analysis to reject and isolate backgrounds as well as to enhance VBF signal strength. This section lists and describe key observables used in the analysis.

- $m_{\tau\tau}$: This is fully defined in Section 4.5. If charged leptons are the products of a pair of τ leptons, the neutrinos are assumed to be collinear with the charged leptons, and the neutrinos are the only source of the observed E_T^{miss} . Requirements on this variable target $Z \rightarrow \tau\tau$ events.
- N_{b-jet} : Defines the number of jets with $p_T > 20$ GeV identified as b -jets from the b -tagging algorithm (DL1) and is used to reject $t\bar{t}$ background.
- $\Delta\phi_{ll}$: The two leptons from HWW decays tend to be collimated especially compared to non-resonant WW backgrounds. This is due to the spin-zero initial state of the resonant process.
- m_{ll} : The invariant mass of the two leptons from the hard scattering interaction; this targets Drell-Yan events and requires $m_{ll} > 70$ GeV in the control region.

CHAPTER 5. EVENT SELECTION

- m_T : Transverse mass is used as a discriminant for the $Z+jets$ control region. It is defined as

$$m_T = \sqrt{(E_{ll} + E_T^{miss})^2 - |p_{ll} + E_T^{miss}|^2}, \quad (5.1)$$

where $E_{ll} = \sqrt{|p_{ll}|^2 + m_{ll}^2}$.

- p_T^{tot} : Total transverse momentum p_T^{tot} is defined in Section 4.5. This variable isolates events with significant soft gluon radiation but not high p_T jets.
- ΔY_{jj} : VBF Higgs signal events are characterized by a large separation of the two tagging jets in rapidity. This variable is used as a signal region cut.
- m_{jj} : VBF Higgs events tend to have a high jet invariant mass (m_{jj}), defined by combining mass of tagged jets. This analysis applies a cut on m_{jj} in our signal region.
- η_{lep} centrality: This analysis uses an outside lepton veto defined to reject events with leptons outside the rapidity gap between the two tagged jets. The sum of the centralities of each lepton is used as a discriminant to train various multivariate classifiers. The OLV variable is defined using pseudorapidity of the tagged jets and leptons as follows:

$$\begin{aligned} \text{OLV}_{l_0} &= 2 \cdot \left| \frac{\eta_{l_0} - \bar{\eta}}{\eta_{j_0} - \eta_{j_1}} \right|, \\ \text{OLV}_{l_1} &= 2 \cdot \left| \frac{\eta_{l_1} - \bar{\eta}}{\eta_{j_0} - \eta_{j_1}} \right|, \\ \eta_{\text{lep}} \text{ centrality} &= \text{OLV}_{l_0} + \text{OLV}_{l_1}, \end{aligned} \quad (5.2)$$

where $\bar{\eta} = (\eta_{j_0} + \eta_{j_1})/2$ and so for each lepton:

$$\text{OLV}_l \left\{ \begin{array}{ll} = 0 & \rightarrow \text{The lepton is within the rapidity gap between the two tagged jets.} \\ < 1 & \rightarrow \text{The lepton lies within the rapidity gap between the two tagged jets.} \\ > 1 & \rightarrow \text{The lepton is outside the rapidity gap between the two tagged jets.} \end{array} \right. \quad (5.3)$$

- $\sum_{l,j} M_{lj}$: The sum of the invariant masses of all possible lepton-jet pairs are used to train our signal discriminant as VBF Higgs signal peaks at a higher value than the dominant backgrounds. VBF signal jets tend to be very forward while lepton central so a large separation between lepton and jets is expected as opposed to typical background topologies.

5.4 Event selection

Figure 5.2 shows the Feynman diagram for the vector boson fusion Higgs production mode. Two energetic jets with large separation in rapidity accompany the Higgs and its decay products. In addition, since the Higgs is created through the fusion of two electro-weak bosons, there is no QCD interaction between the jets and the Higgs boson or its decay products. The main backgrounds this analysis seeks to mitigate include top quark production, Drell-Yan/ Z , di-bosons (WW , WZ , ZZ , and $W\gamma$), ggF Higgs production, and $W+jets$.

This analysis controls and estimates these backgrounds with a variety of methods depending on the characteristics of each background. Major backgrounds are estimated in CRs and minor backgrounds are estimated using MC simulation. Top quark production is suppressed in the SR by a b -jet veto requirement and can be studied in a very pure orthogonal set of bins in the signal region defined by a boosted decision tree discriminant. A pure validation

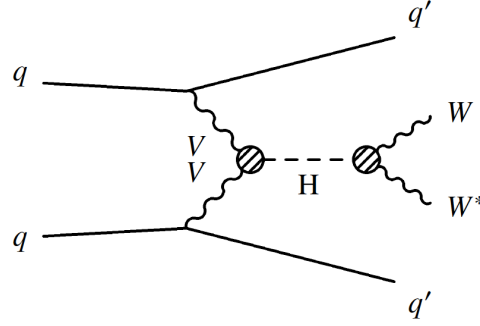


Figure 5.2: Feynman diagram for VBF Higgs production [7]

region is also defined to cross-check top MC modeling. The Drell-Yan/ Z background is suppressed by kinematic requirements and is constrained in a dedicated and orthogonal CR and ultimately normalized in the signal phase space. The ggF Higgs production mode is particularly difficult to separate from the VBF production mode, therefore several CRs are defined to constrain it in data, and ultimately its normalization is determined in the signal phase space. Other Higgs production modes (VH and $t\bar{t}H$) are analyzed and included as backgrounds, but play a very small role in our overall result. The W +jets background is estimated with data-driven techniques, as described in the Chapter 6, and then fixed in the simultaneous fit of SR and CRs.

We utilize multivariate analysis (MVA), more specifically gradient boosted decision trees trained to discriminate between samples. There are six trained BDTs used to separate WW +top and VBF events, VBF and ggF events, ggF events from all other samples in each of their three control regions, and WW +top events and all other samples. The use of these BDTs separates the backgrounds from our signal in the signal region and maintains discrimination between the WW and top background samples.

The WW +top vs. VBF BDT is discussed in this chapter while the others are explained with their associated backgrounds in Chapter 6. In addition, two other types of BDT have been tested in this analysis: a Z +jets vs. VBF BDT and a 3D BDT to separate ggF , WW

CHAPTER 5. EVENT SELECTION

and VBF events. Results from these tests showed that though these led to minimization of background (in the case of $Z+jets$ vs. VBF) and good discrimination between key backgrounds in the signal region (in the case of the 3D BDT), when used in the final fit with systematic uncertainties they showed no significant decrease in calculated error in the VBF coupling value. Results from these studies are shown in Appendix B and C.

Background	Relative size Pre-selection	Relative size Signal Region	Estimation	Generator
WW	$\sim 8\%$	$\sim 20\%$	MC only + BDT	SHERPA 2.2.2 ($gg \rightarrow WW$: SHERPA 2.1)
Top	$\sim 73\%$	$\sim 61\%$	MC only + BDT	POWHEG+PYTHIA 8
ggF Higgs	$< 1\%$	$\sim 2\%$	MC only + BDT	POWHEG+PYTHIA 8 NNLOPS
$W+jets$	$\sim 2.5\%$	$\sim 4\%$	Data-driven	-
$Z \rightarrow \tau\tau$	$\sim 16\%$	$\sim 7\%$	Data+MC ($Z \rightarrow \tau\tau$ CR)	SHERPA 2.2.1
$W\gamma, W\gamma^*$	$\sim 1\%$	$\sim 2.5\%$	MC only	SHERPA 2.1/SHERPA 2.2.2

Table 5.3: Each background and its relative size of in SR (after all cuts), estimation method, and generator.

5.4.1 Pre-selection

The VBF differential analysis shares object definitions with the VBF and ggF coupling analysis and pre-selection cuts are based off of those used in the 2016 ggF and VBF $H \rightarrow WW$ 36.1 fb^{-1} cross-section paper [15]. The VBF selection utilizes observables defined in the previous section. Cuts applied in the preselection region are listed and described in Table 5.4.

Yields for all samples as well as data for pre-selection cuts are shown in Table 5.5.

The plots in Figure 5.3 show kinematic distributions after all preselection cuts with fake factors applied directly after a 2-jet cut. These show good modeling with data over a variety of kinematic variables including those used in the Top+ WW vs. VBF BDT. We were not able to directly examine modeling of input variables to this BDT because blinding is required in the signal region. Modeling in the pre-selection region was studied in lieu of

CHAPTER 5. EVENT SELECTION

Pre-sel cut	Description
Channel Selection	Fits $e\mu/\mu e$ channel/event weight applied
Trigger Selection	Trigger selected
Trigger Matching	Trigger weight applied
Data driven muon/electron	W+jets split into electron and muon fake flavors
Cut Jet Cleaning	Pass loose jet cleaning
Cut $V\gamma/Z$ +jets overlap	Eliminate any Z +jets events that overlap with $V\gamma$
Only two leptons	Require exactly 2 leptons (in case of fakes make sure 1 ID/1 Anti-ID)
Lead lepton p_T	$p_T^{lead} > 22\text{GeV}$
Sublead lepton p_T	$p_T^{sublead} > 15\text{GeV}$
Opposite sign leptons	Require zero dilepton charge
Fake Factor	W+jets weight applied

Table 5.4: Table describing pre-selection cuts applied in common with VBF and ggF coupling analyses

$\mathcal{L} = 139 \text{ fb}^{-1}$	H_{VBF}	H_{ggF}	$H_{VH/ttH}$	Diboson	Top	Z_{jets}	Mis-Id	Data	Data/MC
Channel Selection	904.81 \pm 0.92	9452.28 \pm 10.11	3666.16 \pm 3.84	303490.72 \pm 801.96	1709307.70 \pm 287.98	655027.79 \pm 1233.45	5121458.35 \pm 4457.28	4374979	0.56 \pm 0.00
Trigger Matching	882.26 \pm 0.90	9154.83 \pm 9.82	3559.20 \pm 3.73	291625.39 \pm 761.98	1678206.02 \pm 283.57	624251.33 \pm 1168.16	5275683.79 \pm 4374.34	4352644	0.55 \pm 0.00
Jet Cleaning	882.26 \pm 0.90	9154.83 \pm 9.82	3559.20 \pm 3.73	291625.39 \pm 761.98	1678206.02 \pm 283.57	624251.33 \pm 1168.16	3905166.04 \pm 3213.25	4352644	0.67 \pm 0.00
Only two Leptons	880.17 \pm 0.89	9147.93 \pm 9.81	3543.12 \pm 3.73	289154.52 \pm 756.66	1662432.27 \pm 282.33	622191.46 \pm 1160.36	3903952.62 \pm 3197.39	4331979	0.67 \pm 0.00
$p_T^{lead} > 22 \text{ GeV}$	880.17 \pm 0.89	9147.93 \pm 9.81	3543.12 \pm 3.73	289154.52 \pm 756.66	1662432.27 \pm 282.33	622191.46 \pm 1160.36	3903952.62 \pm 3197.39	4331979	0.67 \pm 0.00
$p_T^{sublead} > 15$	879.98 \pm 0.89	9147.27 \pm 9.81	3542.23 \pm 3.73	288984.90 \pm 756.30	1661877.68 \pm 282.29	622068.28 \pm 1160.19	3902218.38 \pm 3196.64	4330240	0.67 \pm 0.00
OS Leptons	879.86 \pm 0.89	9147.00 \pm 9.81	3540.93 \pm 3.73	288453.03 \pm 752.41	1661388.47 \pm 282.25	622135.47 \pm 1154.02	3896428.83 \pm 3190.85	4326784	0.67 \pm 0.00
Leptons ID	596.53 \pm 0.74	5800.47 \pm 7.84	1778.69 \pm 2.60	146784.04 \pm 237.54	1165160.56 \pm 237.51	257302.75 \pm 431.92	1144546.96 \pm 1611.02	1587474	0.58 \pm 0.00
Apply fake factor	596.53 \pm 0.74	5800.47 \pm 7.84	1778.69 \pm 2.60	146784.04 \pm 237.54	1165160.56 \pm 237.51	257302.75 \pm 431.92	32954.44 \pm 259.52	1587474	0.99 \pm 0.00

Table 5.5: Cutflow in the pre-selection region with statistical errors shown.

this and showed no evidence of bias. In addition, normalization factors (NF) are calculated by data/MC comparisons in top ($Z \rightarrow \tau\tau$) validation (control) regions. These scale factors are added to $Z \rightarrow \tau\tau$ background events in order to correct for MC mis-modeling and are calculated to be 0.99 ± 0.01 and 1.01 ± 0.04 , respectively.

5.4.2 Signal region selection

In addition to the pre-selection cuts which are in common with the ggF coupling analysis, additional selection criteria are applied to the VBF signal region. These selections include a requirement for at least 2 jets ($n_{jets} \geq 2$) and a b -veto using the DL1r b -tagging algorithm. A central-jet-veto (CJV) and an outside-lepton-veto (OLV) are also applied. These remove

CHAPTER 5. EVENT SELECTION

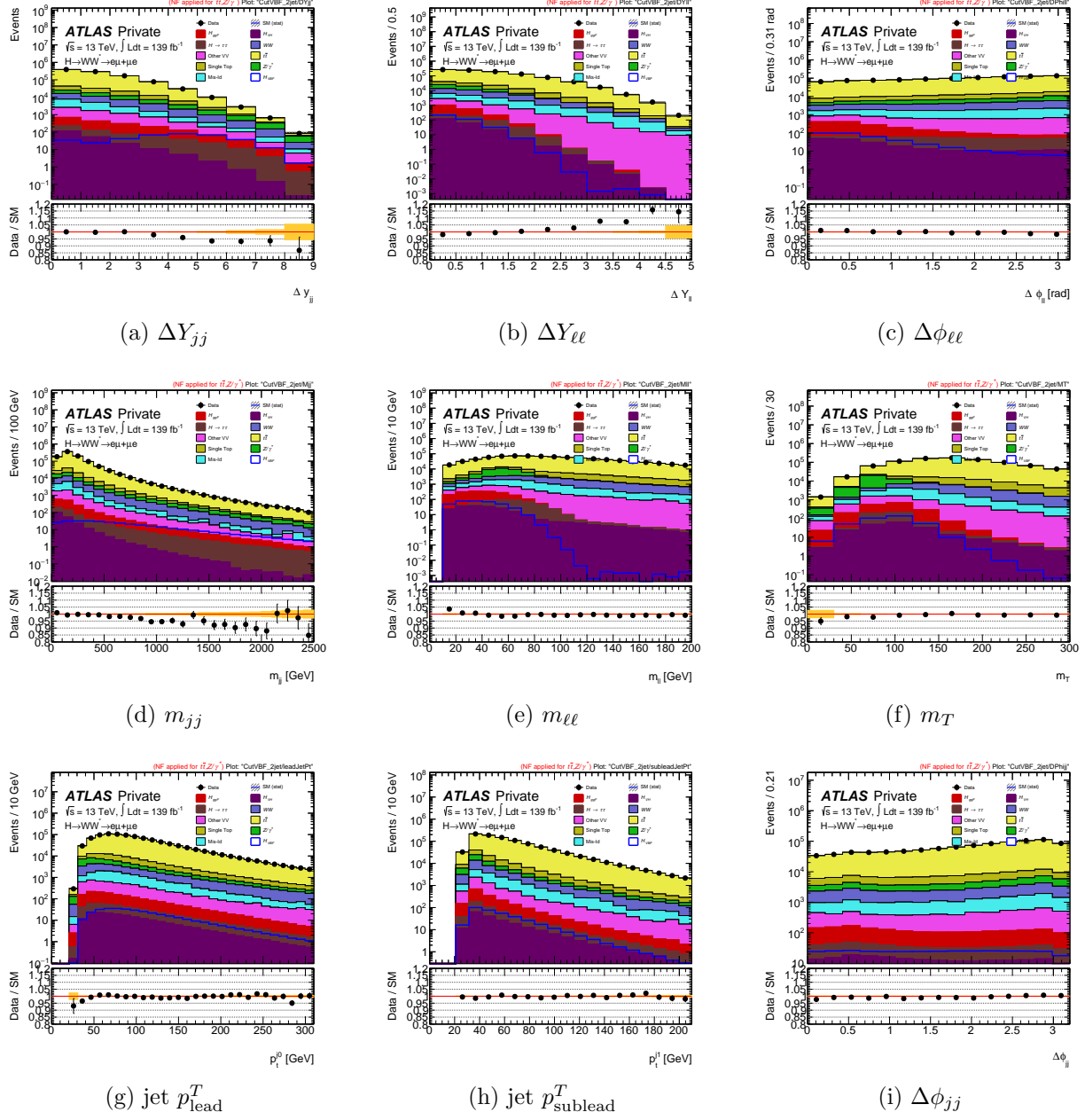


Figure 5.3: Distributions of ΔY_{jj} , ΔY_{ll} , $\Delta \phi_{ll}$, m_{jj} , m_{ll}, m_T , jet p_T^{lead} , jet p_T^{sublead} , and $\Delta \phi_{jj}$ in the preselection region. Distributions show good MC modeling of variables used in the signal region BDT.

CHAPTER 5. EVENT SELECTION

first events with $p_T > 20$ GeV which lie between the tagging jets in pseudo-rapidity and next any event where the two charged leptons are not within the tagging jets' rapidity gap. Two additional cuts that differ from the VBF HWW couplings analysis are also added. These require that the mass of the two jets be > 200 GeV and that the rapidity difference between the two jets be > 2.1 . These further purify the signal region against a range of backgrounds, notably top. The plots in Figure 5.4 show signal and background yields as well as signal significance at a variety of m_{jj} and ΔY_{jj} values. The values used here are chosen for their effects on signal significance while retaining high signal statistics.

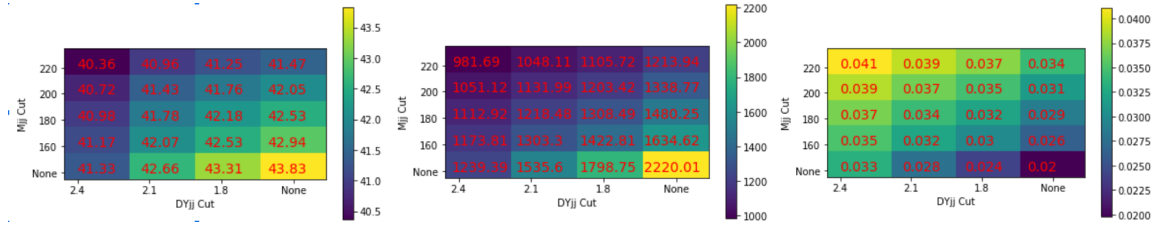


Figure 5.4: Signal and background yields for VBF and total background (aside from fakes) at various m_{jj} and ΔY_{jj} cut values. Simulated events for MC16a campaign only. Choice of cut at $m_{jj} > 200$ GeV and $DY_{jj} > 2.1$ nearly halves background yields while reducing signal by $< 5\%$.

Signal region cuts are listed in Table 5.6.

Signal region cut	Description
2-jet (30,30)	Require at least 2 jets with $p_T \geq 30$ GeV
b -veto	Use DL1 efficiency b -tag reject events with b -jets/apply b -tag weight
Blinding (VBF)	Blinding condition on data (cut on VBF vs. Top+WW BDT)
CJV (20GeV)	Cut events with a third central rapidity jet $p_T > 20$ GeV
OLV bool	Leading lepton η required to be between two η 2 leading jets
$Z \rightarrow \tau\tau$ veto	$m_{\tau\tau} < m_Z - 25$ GeV
m_{jj} cut	$m_{jj} > 200$ GeV
ΔY_{jj} cut	$\Delta Y_{jj} > 2.1$

Table 5.6: Table describing VBF signal region cuts

Yields for all samples, as well as data for signal region cuts are shown in Table 5.7.

CHAPTER 5. EVENT SELECTION

$\mathcal{L} = 139\text{fb}^{-1}$	H_{VBF}	H_{ggF}	H_{VH}/ttH	Diboson	Top	Zjets	Mis-Id	Total Bkg	Significance	Data	Data/MC
2-jet (30,30)	366.47 ± 0.58	1295.72 ± 3.71	546.16 ± 1.37	29416.97 ± 102.99	911158.91 ± 201.74	26427.69 ± 108.55	11693.87 ± 173.01	980539.32 ± 305.02	0.37 ± 0.00	976091	1.00 ± 0.00
b-veto	323.67 ± 0.54	1109.94 ± 3.42	437.85 ± 1.22	25106.71 ± 97.05	63791.88 ± 57.23	22173.36 ± 102.83	3894.07 ± 76.09	116513.82 ± 170.50	0.95 ± 0.00	109677	0.94 ± 0.00
CJV (20GeV)	256.58 ± 0.48	807.85 ± 2.92	328.57 ± 1.05	18007.06 ± 84.13	43137.71 ± 47.63	16175.90 ± 89.43	2702.09 ± 63.72	81159.19 ± 146.33	0.90 ± 0.00	76518	0.94 ± 0.00
OLV	199.59 ± 0.43	218.02 ± 1.52	96.84 ± 0.52	3354.46 ± 38.64	9418.78 ± 22.26	3667.83 ± 45.34	467.18 ± 28.80	17223.10 ± 69.83	1.52 ± 0.00	16472	0.95 ± 0.01
$Z \rightarrow \tau\tau$ veto	172.20 ± 0.40	192.86 ± 1.43	29.99 ± 0.30	2056.45 ± 30.90	6057.87 ± 17.83	1333.31 ± 35.97	316.83 ± 22.36	9987.31 ± 55.40	1.72 ± 0.01	9517	0.94 ± 0.01
$M_{jj} > 200$	165.51 ± 0.39	133.74 ± 1.19	15.72 ± 0.22	1387.95 ± 18.84	3568.95 ± 13.73	858.83 ± 31.05	202.79 ± 16.81	6167.98 ± 42.33	2.10 ± 0.01	5940	0.94 ± 0.01
$DY_{jj} > 2.1$	163.07 ± 0.39	121.34 ± 1.13	13.90 ± 0.21	1217.98 ± 17.55	3005.95 ± 12.74	793.44 ± 30.73	181.99 ± 15.44	5334.60 ± 40.68	2.22 ± 0.01	5106	0.93 ± 0.01

Table 5.7: Cutflow in the signal region.

The following plots in Figure 5.5 show kinematic distributions after the described selection. MC predictions show good modeling of data. Uncertainties shown are purely statistical

VBF signal boosted decision tree discriminant

This analysis uses a number of boosted decision trees (BDTs) to both amplify our VBF signal and discriminate and reject a number of specific backgrounds. A decision tree is a collection of cuts designed to classify events as signal-like or background-like. A given signal event is correctly identified if it is placed in a signal-dominated leaf and vice-versa for background events. After the initial tree is built, another tree is grown to better separate the signal and background events misidentified by the first tree. This proceeds iteratively until there is a collection of a specified number of trees, in a process known as boosting. A weighted average is taken from all these trees to form a BDT output discriminant with values ranging from -1 to 1.

This section will focus on the BDT trained and used in the signal region to isolate the VBF signal from dominant backgrounds (top and WW events). The discriminant used in this analysis is the result of numerous studies on training parameters, input variables, and multivariate analysis techniques. Appendix C shows results from studies on using a multidimensional BDT to simultaneously discriminate VBF, ggF, and WW background samples. While initially this 3D BDT showed promising results, estimation of ggF backgrounds

CHAPTER 5. EVENT SELECTION

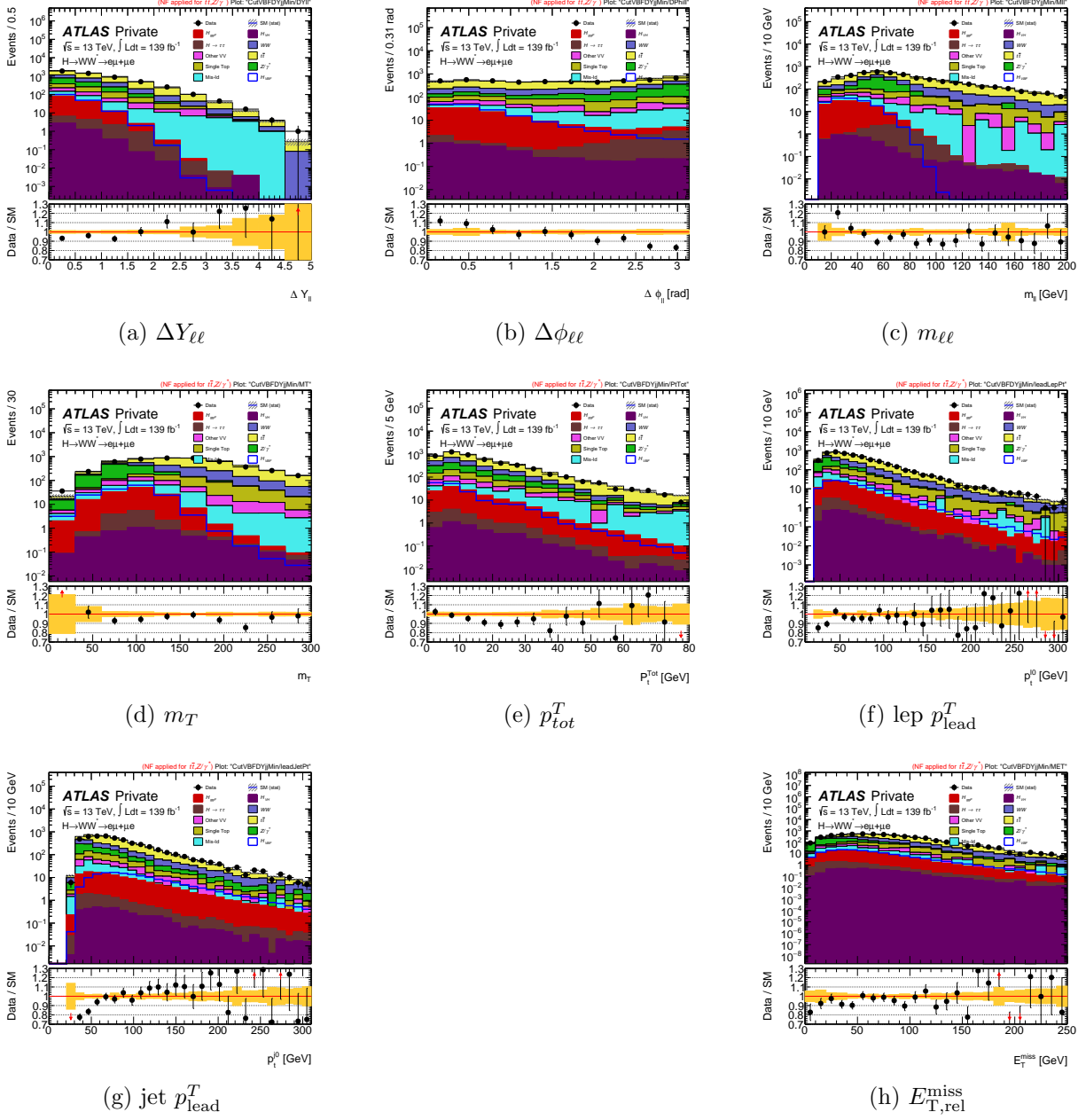


Figure 5.5: Distributions of $\Delta Y_{\ell\ell}$, $\Delta \phi_{\ell\ell}$, $m_{\ell\ell}$, m_T , $p_{\ell\ell}^T$, lep p_{lead}^T , jet p_{lead}^T and $E_{\text{T},\text{rel}}^{\text{miss}}$ in the differential VBF signal region, many used as input to the BDT discriminating VBF from top + WW backgrounds.

CHAPTER 5. EVENT SELECTION

through use of multiple control regions (summarized in the next chapter) showed better determination of the ggF background, so the one-dimensional method here was adopted.

This BDT is trained using $e\mu + \mu e$ events after the VBF selection and the signal regions cuts including that on n_{jets} , b -veto, OLV, CJV, M_{jj} and ΔY_{jj} . In this way, the phase space in which we train the BDT is exactly the same as the one where we apply it. The training includes only the top and WW backgrounds and the VBF signal. Half of the available events are used for training and the other half are used to test the training. This corresponds to about 90,000 un-weighted WW and top events and 100,000 raw VBF events. This training includes MC weights on events to best account for overall event distributions. There are approximately 2000 total weighted top and WW events used in the training and 80 weighted VBF events. The TMVA BDTG interface is used to train and test the BDT [52]. The optimal parameters were found through a scan of reasonable values and the final set is summarized in Table 5.8. This BDT utilizes 12 lepton and jet kinematic variables to

Parameter	Value
Boosting algorithm	Gradient
Maximum tree depth	22
Number of trees	400
Minimum number of events requires per mode	5%
Number of cuts	7

Table 5.8: BDT parameters used for the VBF vs. top + WW training.

distinguish between signal and background events. These include ΔY_{jj} , $\Delta Y_{\ell\ell}$, $\Delta\phi_{\ell\ell}$, m_{jj} , $m_{\ell\ell}$, m_T , η_{j0} , η_{j1} , p_{j0}^T , p_{j1}^T , $\Delta\phi_{jj}$, and \sum centralities (L). While a larger variety of variables have been tested, these demonstrated the highest discrimination between VBF and top/ WW background. Figures 5.6 and 5.7 demonstrate the input distributions used to train the BDT and their correlations.

The BDT training successfully separates VBF signal and top/ WW background. These

CHAPTER 5. EVENT SELECTION

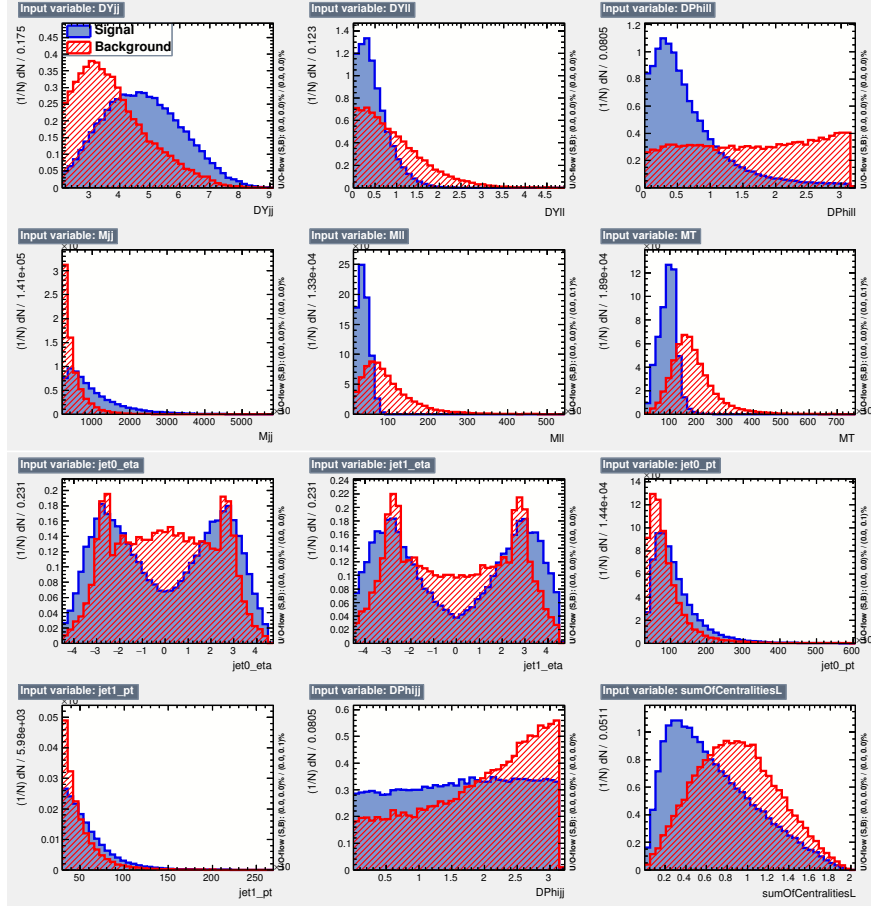


Figure 5.6: Distributions of input variables to VBF vs. top+WW BDT. Samples are weighted and normalized to even numbers of background and signal events. Signal represents VBF and background top+WW [53].

CHAPTER 5. EVENT SELECTION

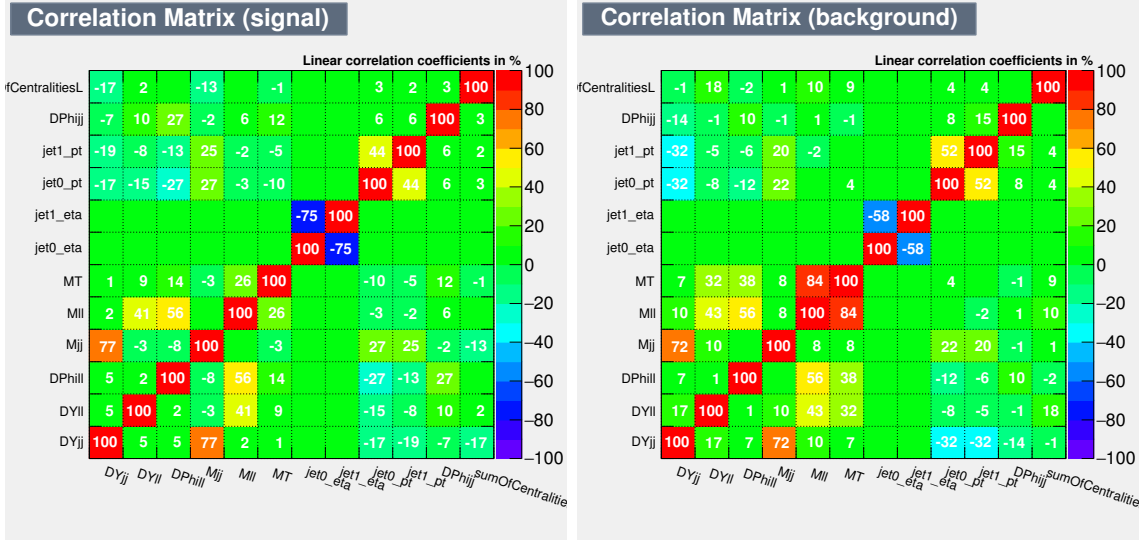


Figure 5.7: Correlations of input variables to VBF vs. top + WW BDT. Signal represents VBF and background top+ WW [53].

backgrounds are considered together because our overall fit uses one parameter to estimate both WW and top backgrounds due to their similar signatures. One useful metric to test the success of a classifier is a receiver operating characteristic curve (ROC curve). This curve measures signal acceptance over background rejection and its integral for a perfect classifier would be 1. In order to quantify the discrimination we use the integrated-ROC calculated through TMVA for weighted normalized samples and find an optimal value of 0.960, showing very good classification. Comparisons between the test and training show that the BDT is un-biased as one can see that the testing and trainings samples are quite similar. Differences between testing and training samples would imply overtraining, or the BDT using too many parameters on too few events. A Kolmogorov-Smirnov (KS) test is performed to measure if the two test and training distributions differ significantly. If the two distributions are random samples of the same parent distribution, the KS-test would give a uniformly distributed value between zero and one (or an average value of 0.5). The closer to 0.5 the KS-test value, the greater likelihood the curves come from the same parent, however this calculation is heavily

CHAPTER 5. EVENT SELECTION

skewed toward lower values so any value above zero (or not very close to zero, on order 10^{-4}) can be considered not indicative of overtraining. For signal and background we find KS-test values of 0.107 and 0.154, and so no evidence of over-training. We can visualize the BDT output variable both on weighted normalized samples and on samples with all event weights applied. Figures 5.8 and 5.8 show BDT results applied to normalized samples of VBF signal and top/ WW backgrounds and applied to all fully weighted samples in the signal region.

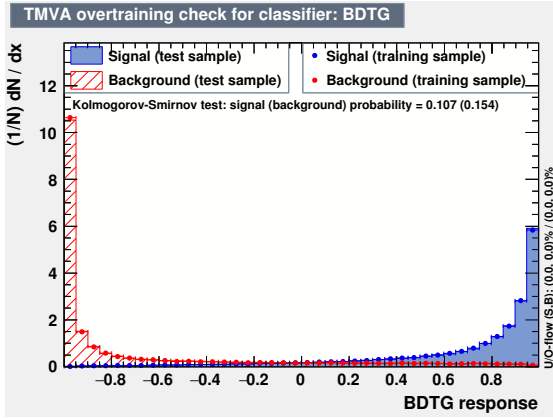


Figure 5.8: Weighted, normalized samples of VBF (signal) and top+ WW samples (background) plotted over BDT output distribution, overlaid testing and training samples shown [53].

We aim to fit this distribution in the signal region with high significance in uppermost bins of the distribution. Since this BDT is trained and applied in the signal region, we cannot directly test the modeling of input variables. However, these variables at the pre-selection level are shown earlier in the chapter and demonstrate successful modeling of data. The binning for this discriminant used in the statistical fit and its result are shown in the final chapter.

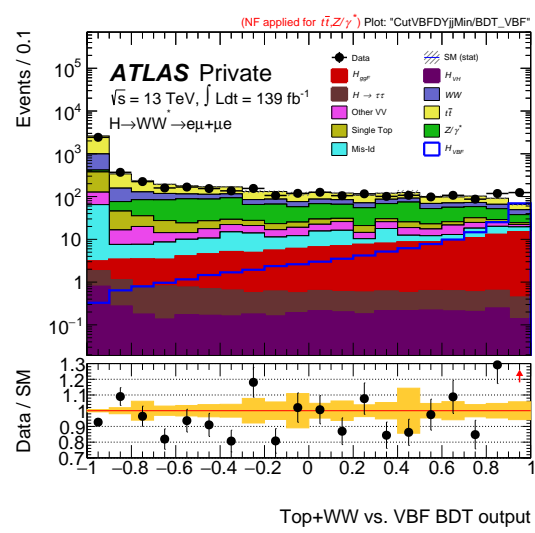


Figure 5.9: Full weighted samples of VBF signal and all backgrounds plotted over BDT output distribution after signal region selection.

Chapter 6

Backgrounds and Systematics

6.1 Backgrounds

While the VBF $H \rightarrow WW \rightarrow \ell\nu\ell\nu$ channel gives a fairly clear signal with E_T^{miss} , two leptons, and 2 jets, there are substantial backgrounds with similar final states. These include Drell-Yan processes (in which a Z boson is formed from quark anti-quark annihilation of the two colliding protons), top quark final states (predominantly $t\bar{t}$), diboson events (led by SM WW events), Higgs decays from the other production modes (mainly ggF), and background from mis-identified leptons, called fakes. In this section I will detail each background and describe our methods for estimating their role in overall results. I will describe how this analysis estimates and minimizes contributions from each background process. Finally, I will measure the purity and validate the modeling of these backgrounds by using events in “control” and “validation” regions. These regions are designed to select for particular backgrounds to use in the final statistical fit, “control regions”, or to test that backgrounds overall modeling, “validation regions”. I made key contributions in this analysis in optimizing and testing control region definitions and their effects on our overall results.

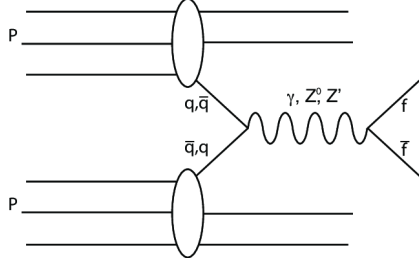


Figure 6.1: Feynman diagram for Drell-Yan process in which two quarks produce a photon or Z -boson that then decays leptonically [54].

6.1.1 Drell-Yan background ($Z \rightarrow \tau\tau$)

The Drell-Yan background is produced in the initial collision when two quarks produce a Z boson which then decays to two leptons. In this analysis we select two different flavor leptons in order to reject large Drell-Yan backgrounds in which the Z decays to two electrons or two muons. However, our signal is still contaminated by Drell-Yan decays where the Z decays to two τ leptons. We select events where one τ decays to an electron and the other to a muon. There are two jets and two leptons in this the Drell-Yan final state as well as missing energy from neutrinos, all of which are indicative of signal VBF Higgs events. The Feynman diagram for a typical Drell-Yan event is shown in Figure 6.1.

Removing events in a 25 GeV window about the Z -mass peak drastically improves Z +jets purity from only 19% of total events to approximately 52%.

We have also tested and trained a secondary discriminant for Z +jets in our analysis, a BDT trained to discriminate between Z +jets and VBF signal events. This BDT significantly decreases overall Z +jets background in our signal region but we found that the subsequent decrease in statistics from using this cut leads to very similar overall results. The results from this comparison are shown in Appendix B.

CHAPTER 6. BACKGROUNDS AND SYSTEMATICS

Drell-Yan Control Region

The Z +jets control region definition is quite similar to the VBF signal region except that the Z +jets veto cut is inverted. Thus instead of removing events near the Z -mass window we select for them by applying a cut on $m_{ll} < 80$ GeV, $66.2 \text{ GeV} < m_{\tau\tau} < 116.2 \text{ GeV}$, and the same OLV and CJV cuts as in the VBF signal region. The Z +jets control region has a purity of $\approx 82\%$ and yields in this region are shown in the Table 6.1.

$\mathcal{L} = 139 \text{ fb}^{-1}$	H_{VBF}	H_{ggF}	$H_{VH}/t\bar{t}H$	Diboson	Top	Zjets	Mis-Id	Data	Data/MC
$ m_{\tau\tau} - m_Z < 25$	27.15 ± 0.16	84.85 ± 0.95	101.90 ± 0.60	2540.17 ± 32.93	5635.24 ± 17.11	8909.14 ± 45.18	417.01 ± 26.17	16400	0.93 ± 0.01
$M_{ll} < 80 \text{ GeV}$	26.48 ± 0.16	82.16 ± 0.93	83.99 ± 0.55	1081.54 ± 27.11	1703.83 ± 9.25	8674.53 ± 40.97	232.18 ± 20.92	10805	0.91 ± 0.01
$\text{CJV} < 20 \text{ GeV}$	20.86 ± 0.14	58.69 ± 0.79	63.86 ± 0.48	790.53 ± 23.90	1150.59 ± 7.67	6474.42 ± 35.91	185.09 ± 18.00	7931	0.91 ± 0.01
OLV	16.04 ± 0.12	14.49 ± 0.39	21.00 ± 0.24	157.28 ± 12.16	292.25 ± 3.90	1392.75 ± 17.23	15.06 ± 8.64	1832	0.96 ± 0.03

Table 6.1: Cutflow in the Z +jets control region.

Data/MC shows agreement over various variable distributions as seen in Figures 6.2. Some of these variables are also used in the BDT described in Appendix B.

Normalization factors (NF) are derived in the Z +jets control region to correct for Data/MC mis-modeling. These factors are applied to the Z +jets sample in the signal region. The NF factor used in this analysis is 1.01 ± 0.04 .

6.1.2 Top background

The top background consists of two main components, Wt and $t\bar{t}$ events, where the W decays leptonically and the top quarks decay to jets (notably b -jets). The top background is dominated by $t\bar{t}$ and is the largest background in our signal region, composing about 60% of the total background. Though top backgrounds are numerous, discrimination between top and signal Higgs events is possible through training a BDT on variables that have very different distributions between these two types of events like $m_{\ell\ell}$ and ΔY_{jj} . As demonstrated in Chapter 5, our BDT discriminates between signal and top background quite well. The

CHAPTER 6. BACKGROUNDS AND SYSTEMATICS

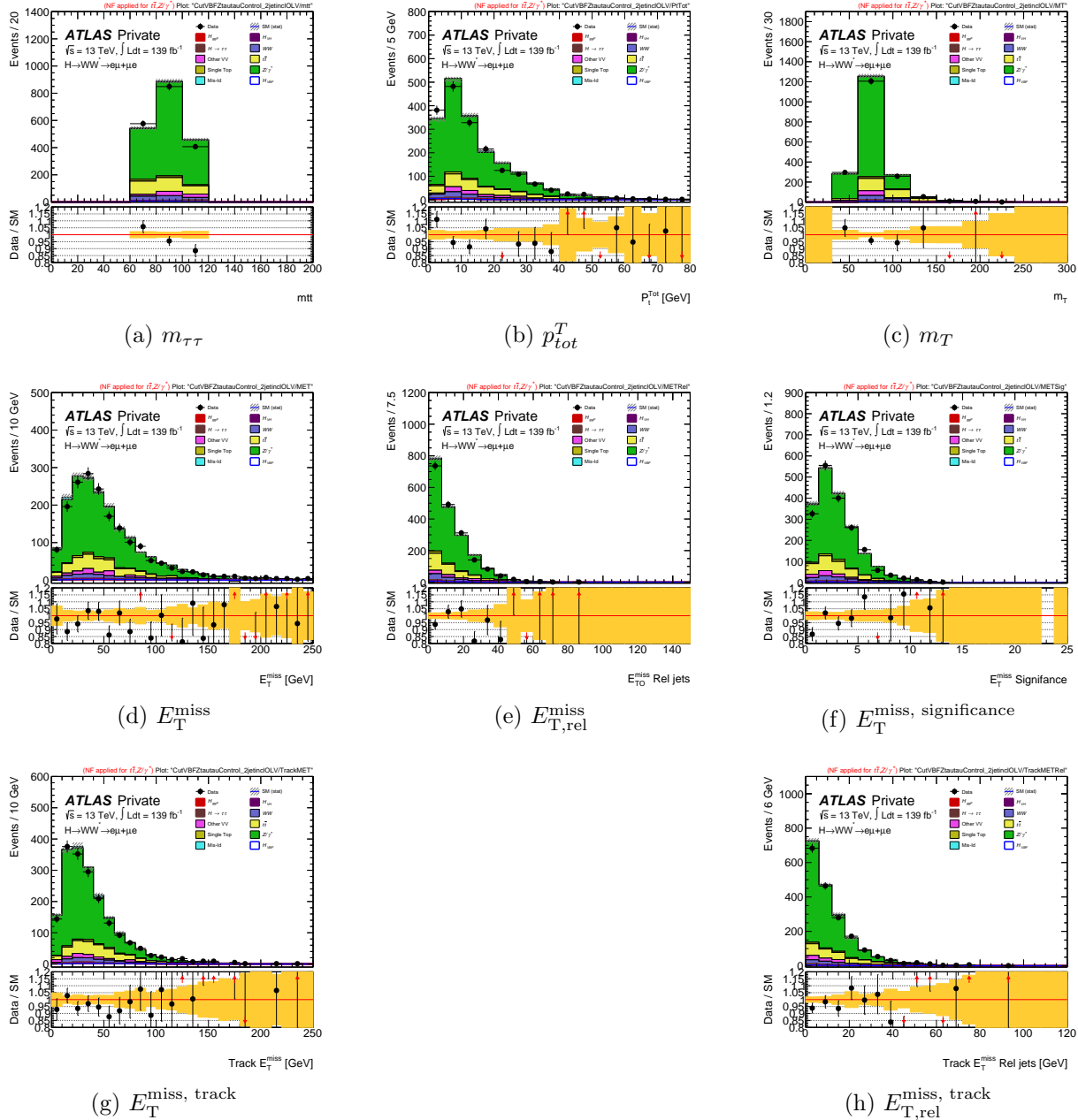


Figure 6.2: Distributions of $m_{\tau\tau}$, p_{tot}^T , m_T , $E_{\text{T}}^{\text{miss}}$, $E_{\text{T},\text{rel jets}}^{\text{miss}}$, $E_{\text{T}}^{\text{miss}, \text{significance}}$, $E_{\text{T}}^{\text{miss}, \text{track}}$, and $E_{\text{T},\text{rel jets}}^{\text{miss}}$ in the $Z + \text{jets}$ control region.

top background is therefore defined in the signal region and separated using the VBF vs. top+WW discriminant. The final statistical fit uses six total BDT discriminants and two

CHAPTER 6. BACKGROUNDS AND SYSTEMATICS

of these are associated with the top background: VBF vs. top+ WW and top+ WW vs. all other samples. The overall statistical fit strategy is discussed in the following chapter but in this section I will describe the BDT used as the top discriminant: top+ WW vs. all other samples.

We define a top validation region to test top Monte Carlo modeling and calculate a normalization factor used to correct top mis-modeling in the signal region. The top validation region is described similarly to the signal region with one major difference: the b -tagging selection applied in the signal region is (almost) reversed. Instead, we require exactly one b -tagged jet. The result is a highly pure top validation region, approximately 97%, where the flavor composition of the tagged jets is close to the signal region. Yields in this region are shown in the Table 6.2.

$\mathcal{L} = 139 \text{ fb}^{-1}$	H_{VBF}	H_{ggF}	$H_{VH}/t\bar{t}H$	Diboson	Top	Zjets	Mis-Id	Data	Data/MC
$n_{b-jets} = 1$	39.79 ± 0.19	162.38 ± 1.34	89.41 ± 0.57	3922.22 ± 31.68	349820.12 ± 128.80	3683.96 ± 34.18	4601.97 ± 97.54	359758	0.99 ± 0.00
$Z \rightarrow \tau\tau$ veto	18.05 ± 0.13	22.85 ± 0.50	5.66 ± 0.13	245.35 ± 12.82	30023.80 ± 38.13	180.86 ± 8.66	280.21 ± 28.51	30709	1.00 ± 0.01
CJV < 20 GeV	29.69 ± 0.17	106.25 ± 1.08	62.42 ± 0.47	2518.28 ± 26.99	238659.28 ± 107.33	2487.15 ± 30.44	2941.00 ± 80.13	244811	0.99 ± 0.00
OLV	20.85 ± 0.14	25.71 ± 0.53	13.85 ± 0.20	411.01 ± 13.96	46267.04 ± 47.47	499.81 ± 12.91	415.70 ± 35.23	47182	0.99 ± 0.00
$Z \rightarrow \tau\tau$ veto	18.05 ± 0.13	22.85 ± 0.50	5.66 ± 0.13	245.35 ± 12.82	30023.80 ± 38.13	180.86 ± 8.66	280.21 ± 28.51	30709	1.00 ± 0.01

Table 6.2: Cutflow in the top control region.

Data/MC in the top validation region shows good agreement over various variable distributions as seen in Figure 6.3. Many of these distributions are used as inputs to the top+ WW vs. all BDT.

Top+ WW BDT discriminant

The top+ WW BDT is trained after the VBF selection and applied in the same phase space. The training includes top and WW trained against weighted samples of VBF, ggF, $Z+jets$, and $V\gamma$ events. There are about 90,000 un-weighted WW and top events corresponding to approximately 2,000 weighted events and about 115,000 un-weighted VBF,

CHAPTER 6. BACKGROUNDS AND SYSTEMATICS

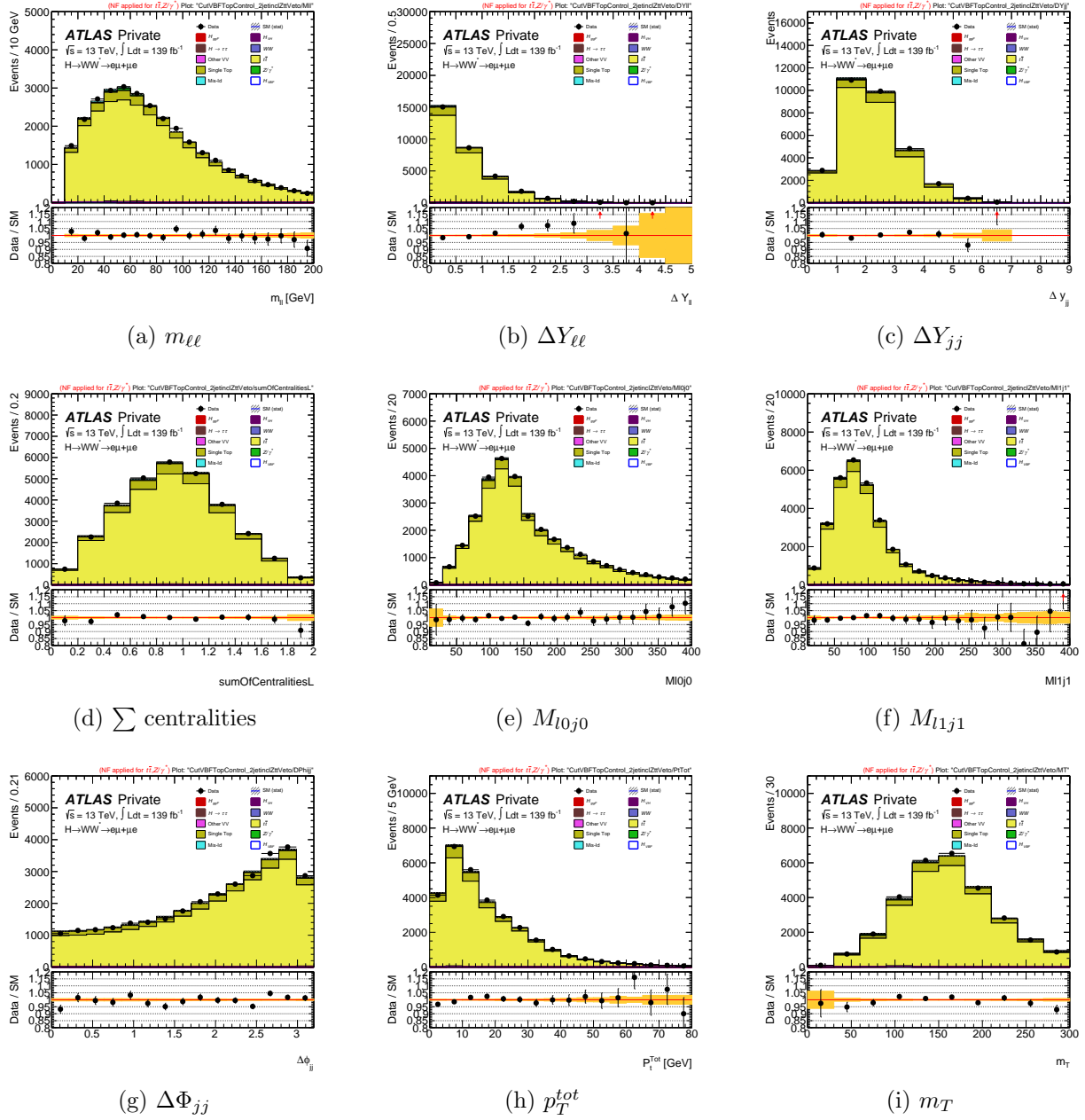


Figure 6.3: Distributions of $m_{\ell\ell}$, $\Delta Y_{\ell\ell}$, ΔY_{jj} , \sum centralities, M_{l0j0} , M_{l1j1} , $\Delta\Phi_{jj}$, p_T^{tot} , and m_T in the top validation region.

ggF, $Z+jets$ and $V\gamma$ events corresponding to 550 weighted events. The same BDT training interface and strategy discussed in Chapter 5 is used again here. The final set of testing

CHAPTER 6. BACKGROUNDS AND SYSTEMATICS

parameters is summarized in Table 6.3.

Parameter	Value
Boosting algorithm	Gradient
Maximum tree depth	22
Number of trees	200
Minimum number of events requires per mode	5%
Number of cuts	7

Table 6.3: BDT parameters used for the top + WW vs. other backgrounds training.

This BDT utilizes 8 lepton and jet kinematic variables to distinguish between top+ WW and other events. These include ΔY_{jj} , the combination of lepton/jet masses M_{l0j0} for leading and subleading leptons and jets, $\Delta\Phi_{\ell\ell}$, m_T , η_{j0} , η_{j1} , $\Delta\Phi_{jj}$, and \sum centralities (L). Figures 6.4 and 6.5 demonstrate the input distributions used to train the BDT and their correlations.

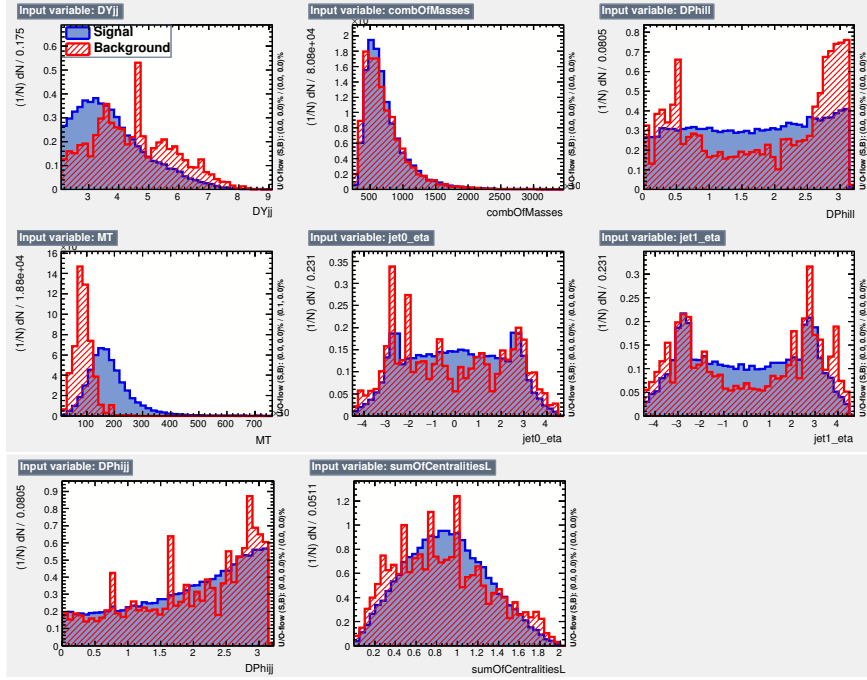


Figure 6.4: Distributions of input variables to top+ WW vs. other samples BDT. Samples are weighted and normalized to even numbers of background and signal events. Signal represents top+ WW and background all other samples [53].

CHAPTER 6. BACKGROUNDS AND SYSTEMATICS

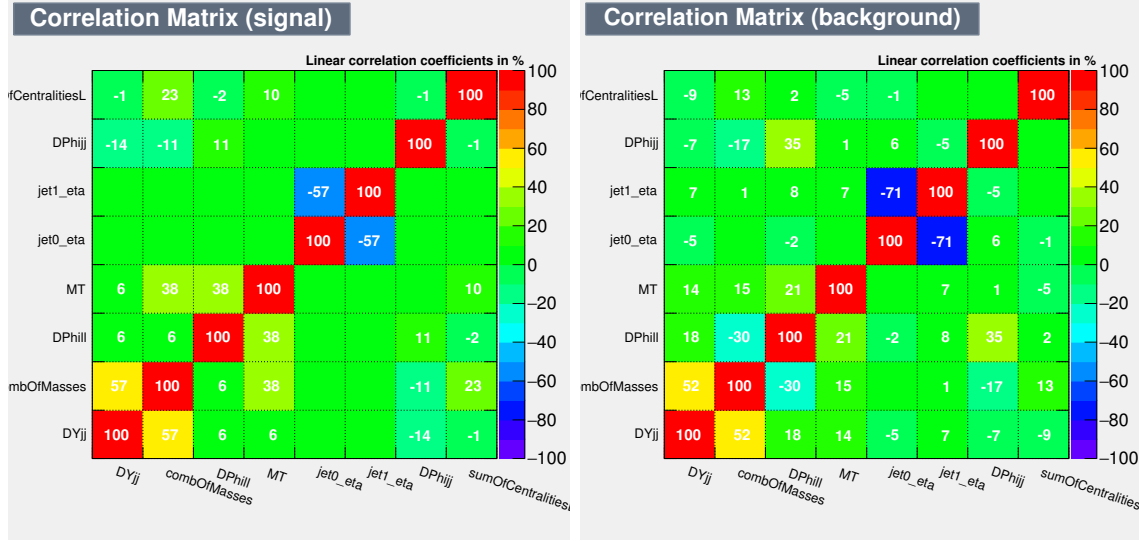


Figure 6.5: Correlations of input variables to top + WW vs other samples BDT. Signal represents top+ WW and background other samples [53].

The BDT training successfully separates top/ WW background and other samples (ggF, VBF, $Z+jets$, and $V\gamma$). We calculate an integrated-ROC value of 0.920. For signal and background we find KS-test values of 0.107 and 0.154 respectively, and so no evidence of over-training. The BDT output variables are shown both on weighted normalized samples and on samples with full event weights applied in Figures 6.6 and 6.7.

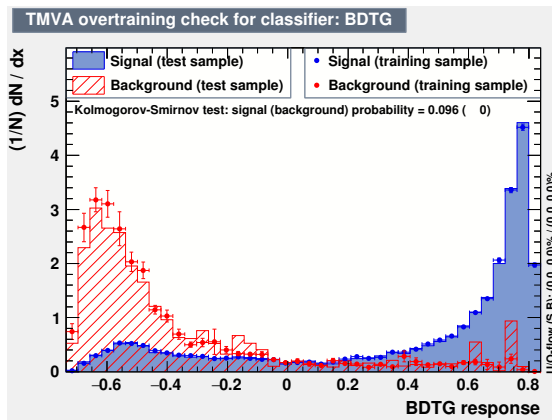


Figure 6.6: Weighted, normalized samples of top+ WW samples (signal) and other samples (background) plotted over BDT output distribution [53].

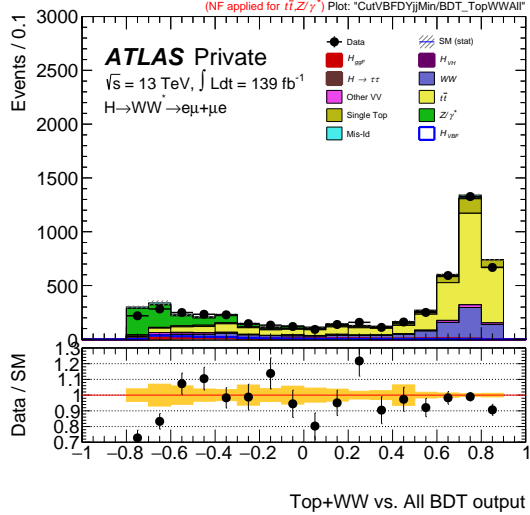


Figure 6.7: Full weighted samples of all signal and background events plotted over BDT output distribution after signal region selection.

We aim to fit this distribution in the signal region with high significance for top/ WW events in the uppermost bins of the distribution. Since this BDT is trained and applied in the signal region, we cannot directly test the modeling of input variables. However, modeling at the pre-selection level for each of these variables as well as in the top validation region described earlier show no evidence of mis-modeling. The binning for this discriminant used in the statistical fit and its result are shown in Chapter 7.

Normalization factors (NF) are derived in the top validation region to correct for data/MC mis-modeling. These factors are applied to the top sample in the signal region. The NF factor used in this analysis is 0.99 ± 0.01 .

6.1.3 Diboson background

The WW background consists primarily of QCD WW +jets events (highly dominating electroweak vertices). This background is estimated along with the top background using a

CHAPTER 6. BACKGROUNDS AND SYSTEMATICS

joint parameter due to their similarities in signature as well as the difficulty in defining a pure WW control region without top contamination. A WW validation region is defined to demonstrate WW MC modeling in a targeted WW region. The WW validation region is defined by requiring at least 2 jets, a b -veto ($N_{b-jet} < 1$) and a central-jet-veto of below 20 GeV as in the signal region. Two additional cuts differ from the signal region: $m_T > 130$ GeV and $m_{T2} > 160$ GeV. m_{T2} , or the stransverse mass, is used to describe a lower bound on a pair-production parent particle's mass. m_{T2} is calculated as the minimum $m_T(m_{\text{inv}}, \vec{p}_T^i)$ for all values of p_T^1 and p_T^2 which satisfy $\vec{p}_T^1 + \vec{p}_T^2 = \vec{p}_T^{\text{miss}}$ [55]. This can be summarized as

$$m_{T2} = \min_{\vec{p}_T^1, \vec{p}_T^2} (\max(m_T(m_{\text{inv}}, \vec{p}_T^1), m_T(m_{\text{inv}}, \vec{p}_T^2))). \quad (6.1)$$

where m_{inv} is zero in this analysis. Requiring $m_{T2} > 160$ GeV eliminates contamination from many $t\bar{t}$ decays which have an upper limit near the top mass. The purity of the WW validation region is $\approx 37\%$ and the cutflow for this region is shown Table 6.4.

$\mathcal{L} = 139 \text{ fb}^{-1}$	H_{VBF}	H_{ggF}	H_{VH}/ttH	Diboson	Top	Zjets	Mis-Id	Data	Data/MC
b-veto	323.67 ± 0.54	1109.94 ± 3.42	437.85 ± 1.22	25106.71 ± 97.05	63787.91 ± 57.22	22151.24 ± 102.73	3793.55 ± 70.69	109677	0.94 ± 0.00
$M_T > 130 \text{ GeV}$	32.37 ± 0.17	155.17 ± 1.28	59.98 ± 0.44	18021.15 ± 51.26	50088.35 ± 50.83	872.43 ± 33.66	1784.17 ± 49.41	68255	0.96 ± 0.00
$M_{T2} > 160 \text{ GeV}$	18.87 ± 0.13	62.44 ± 0.82	17.29 ± 0.24	7271.80 ± 35.96	11553.13 ± 24.82	302.42 ± 14.17	515.71 ± 26.44	18672	0.95 ± 0.01
CJV (20GeV)	13.61 ± 0.11	40.50 ± 0.66	11.30 ± 0.20	4861.01 ± 32.55	6415.93 ± 19.00	184.81 ± 12.88	327.54 ± 20.73	11245	0.95 ± 0.01

Table 6.4: Cutflow in the WW validation region.

Data/MC shows good agreement over various variable distributions as shown in Figure 6.8.

6.1.4 ggF background

Other Higgs production modes are considered backgrounds in this analysis. Vector mediated Higgs production (VH) and top produced Higgs (ttH) are small in our signal region so do not play a large role in the analysis. ggF Higgs production, however, represents a

CHAPTER 6. BACKGROUNDS AND SYSTEMATICS

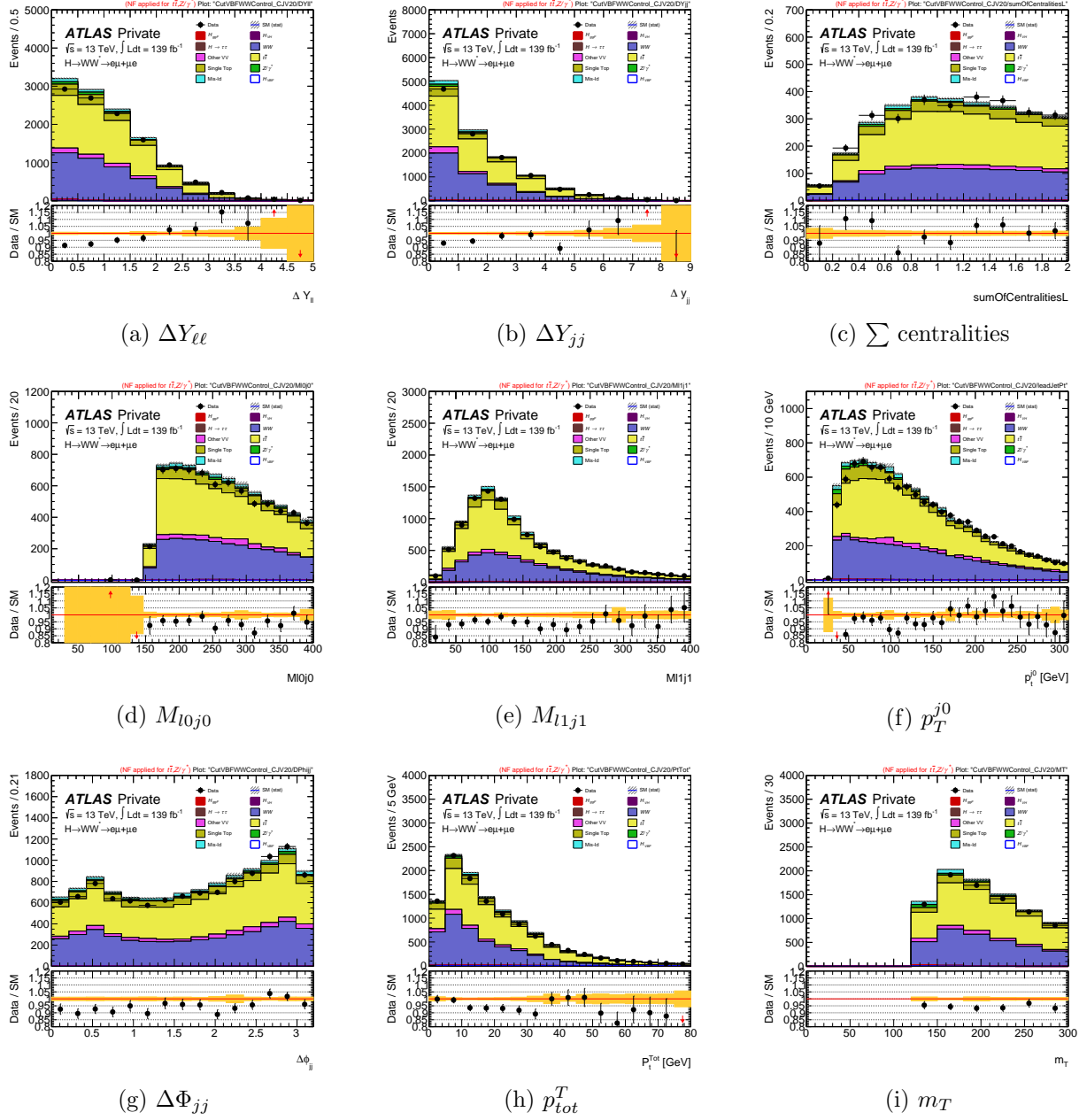


Figure 6.8: Distributions of $\Delta Y_{\ell\ell}$, ΔY_{jj} , \sum centralities, M_{l0j0} , M_{l1j1} , p_T^{j0} , $\Delta\Phi_{jj}$, p_T^T , and m_T in the WW validation region.

significant background. Signal region cuts requiring at least 2-jets and the central jet veto significantly reduce background yields, but because ggF is kinematically very similar to VBF

CHAPTER 6. BACKGROUNDS AND SYSTEMATICS

signal, it still has a large effect on the VBF fiducial cross-section measurement. To mitigate these effects, ggF events are simultaneously estimated from three control regions and the signal region. The control regions are chosen to minimize both the statistical and the modeling uncertainties, in particular those originating from the modeling of higher order QCD corrections. The definition begins with a subdivision based on the jet multiplicity and creates three orthogonal regions that are similarly orthogonal to the signal region. The full definitions are described:

- **GGF-CR1:** Preselection criteria and $N_{\text{jet}} \geq 2$, b veto, $Z \rightarrow \tau\tau$ veto, $\text{CJV} \geq 20$ GeV and $\text{OLV} = 1$ or $\text{CJV} < 20$ GeV and $\text{OLV}! = 1$.
- **GGF-CR2:** Preselection criteria and $N_{\text{jet}} \geq 2$, b veto, $Z \rightarrow \tau\tau$ veto, $\text{CJV} \geq 20$ GeV and $\text{OLV}! = 1$ or $\text{CJV} > 1$ and $\text{OLV} < 1$.
- **GGF-CR3:** Preselection criteria and $N_{\text{jet}} \geq 2$, b veto, and $Z \rightarrow \tau\tau$ veto.

The full ggF expectation in the signal region is built from the following ratio, inspired by the ABCD method [56]:

$$\mu_{\text{GGF-SR}} = \frac{\mu_1^{\text{GGF-CR}} \cdot \mu_3^{\text{GGF-CR}}}{\mu_2^{\text{GGF-CR}}}, \quad (6.2)$$

where μ_{ggF} represents the yield modifier in each ggF control region. In each ggF category, the ggF yield is extracted from simulation-extracted template fits based on dedicated discriminants. For each control region a dedicated multivariate discriminant is trained and applied to discriminate between ggF and all other samples. Results and training parameters from each of these discriminants is summarized next.

Discriminant in ggF CR1

The multivariate discriminant used for ggF CR1 is a boosted decision tree (BDT) trained after the ggF CR1 selection. The training includes ggF events trained against VBF signal and all backgrounds with about 8,000 ggF events (70 weighted) and 250,000 other events (5,000 weighted). The optimal parameters for training are summarized in Table 6.5.

Parameter	Value
Boosting algorithm	Gradient
Maximum tree depth	10
Number of trees	600
Minimum number of events requires per mode	5%
Number of cuts	7

Table 6.5: BDT parameters used for the ggF CR1 training.

For this BDT, 8 kinematic distributions are used to take advantage of differences in distributions between ggF events and other sample types. These variables include $\Delta Y_{\ell\ell}$, $\Delta\Phi_{\ell\ell}$, $m_{\ell\ell}$, m_T , jet p_{lead}^T , jet p_{sublead}^T , $\Delta\Phi_{jj}$, and $E_{\text{T}}^{\text{miss}}$. Distributions for these variables in the ggF CR1 region where the BDT is trained are shown in Figure 6.9 demonstrating data/MC modeling for each.

Figure 6.10 and Figure 6.11 demonstrate the input distributions used to train the BDT and their correlations where each distribution is normalized to equal number of background and signal events.

The BDT has an integrated-ROC value of 0.898, demonstrating successful classification. Comparisons between the test and training show that the BDT is un-biased and a KS-test (values 0.191, 0.049 for signal, background) demonstrates this. The BDT output variable is visualized on weighted normalized samples and on samples without normalization in Figures 6.12 and 6.13.

CHAPTER 6. BACKGROUNDS AND SYSTEMATICS

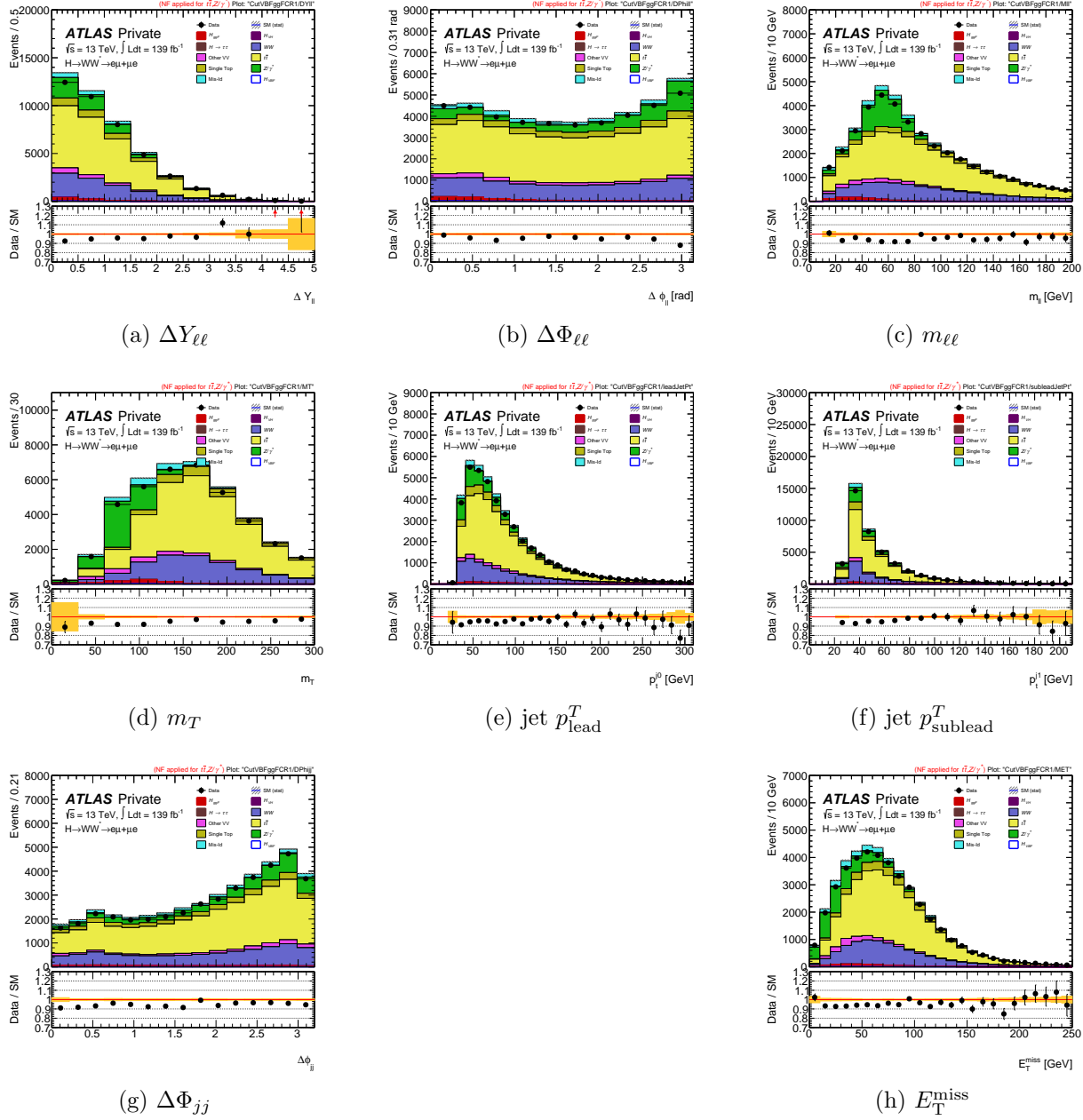


Figure 6.9: Distributions of $\Delta Y_{\ell\ell}$, $\Delta \Phi_{\ell\ell}$, $m_{\ell\ell}$, m_T , jet p_T^{lead} , jet p_T^{sublead} , $\Delta \Phi_{jj}$, and E_T^{miss} in the ggF CR1 used as input to the BDT discriminating ggF from all other samples.

Discriminant in ggF CR2

The ggF CR2 BDT discriminant is trained using all ggF CR2 selection criteria. The training includes about 2,000 unweighted (300 weighted) ggF events trained against 90,000

CHAPTER 6. BACKGROUNDS AND SYSTEMATICS

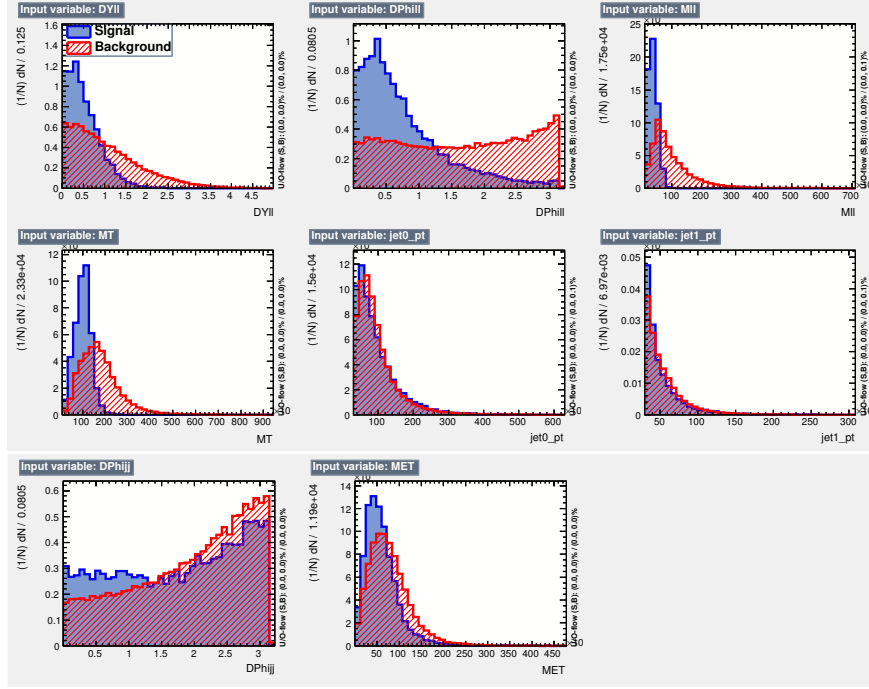


Figure 6.10: Distributions of input variables to ggF CR1 BDT. Samples are weighted and normalized to even numbers of background and signal events. Signal represents ggF and background all other samples [53].

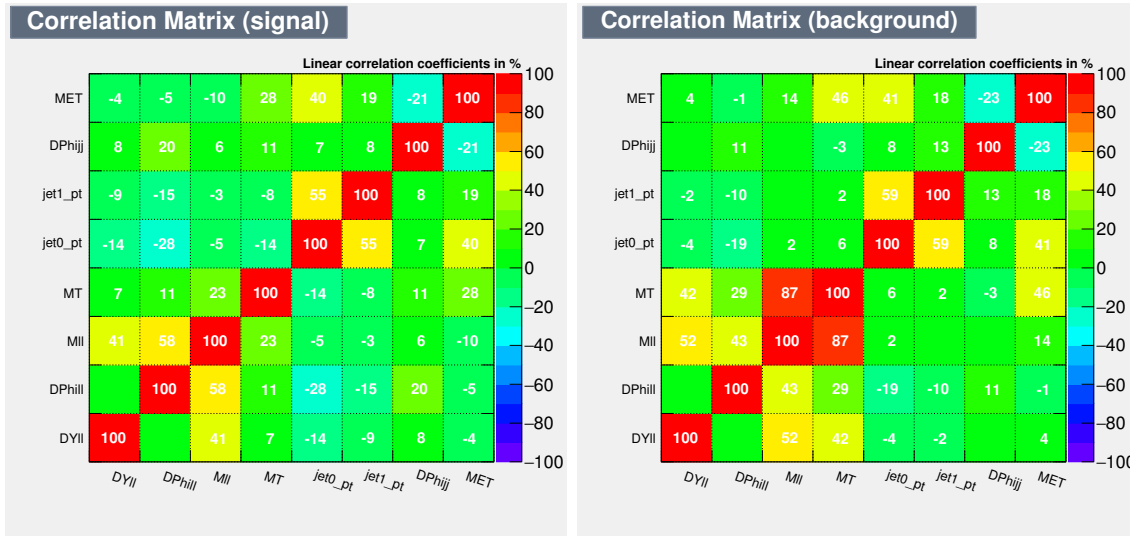


Figure 6.11: Correlations of input variables to ggF CR1 BDT. Signal represents ggF and background all other samples [53].

CHAPTER 6. BACKGROUNDS AND SYSTEMATICS

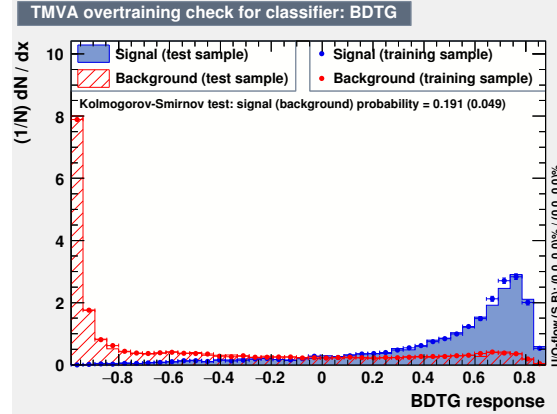


Figure 6.12: Normalized samples of ggF (signal) and all other samples (background) plotted over BDT output distribution, overlaid testing and training samples shown [53].

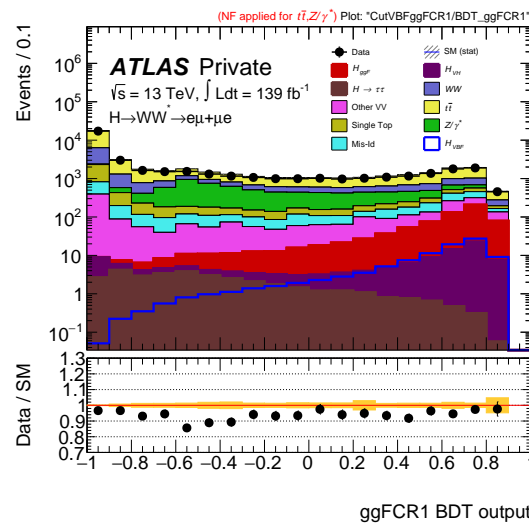


Figure 6.13: Full weighted samples of ggF signal and all other backgrounds plotted over BDT output distribution after ggF CR 1 [53].

CHAPTER 6. BACKGROUNDS AND SYSTEMATICS

un-weighted (1,500 weighted) other samples. The optimal training parameters are summarized in Table 6.6.

Parameter	Value
Boosting algorithm	Gradient
Maximum tree depth	10
Number of trees	50
Minimum number of events requires per mode	5%
Number of cuts	7

Table 6.6: BDT parameters used for the ggF CR2 training.

Six lepton and jet kinematic distributions are used, including $\Delta Y_{\ell\ell}$, $\Delta\Phi_{\ell\ell}$, $m_{\ell\ell}$, m_T , $\Delta\Phi_{jj}$, and E_T^{miss} . Distributions for these variables in the ggF CR2 region are shown in Figure 6.14 and demonstrate data/MC modeling.

Figures 6.15 and 6.16 demonstrate the input distributions used to train the BDT and their correlations where each distribution is normalized to equal numbers of background and signal events.

The integrated-ROC calculated with normalized samples is 0.902, demonstrating good discrimination in the ggF CR2. KS tests measure values of 0.012 (0.303) for signal (background), which shows the BDT training is un-biased. The BDT output variable for ggF CR2 is shown for weighted normalized samples and fully weighted events in Figures 6.17 and 6.18.

CHAPTER 6. BACKGROUNDS AND SYSTEMATICS

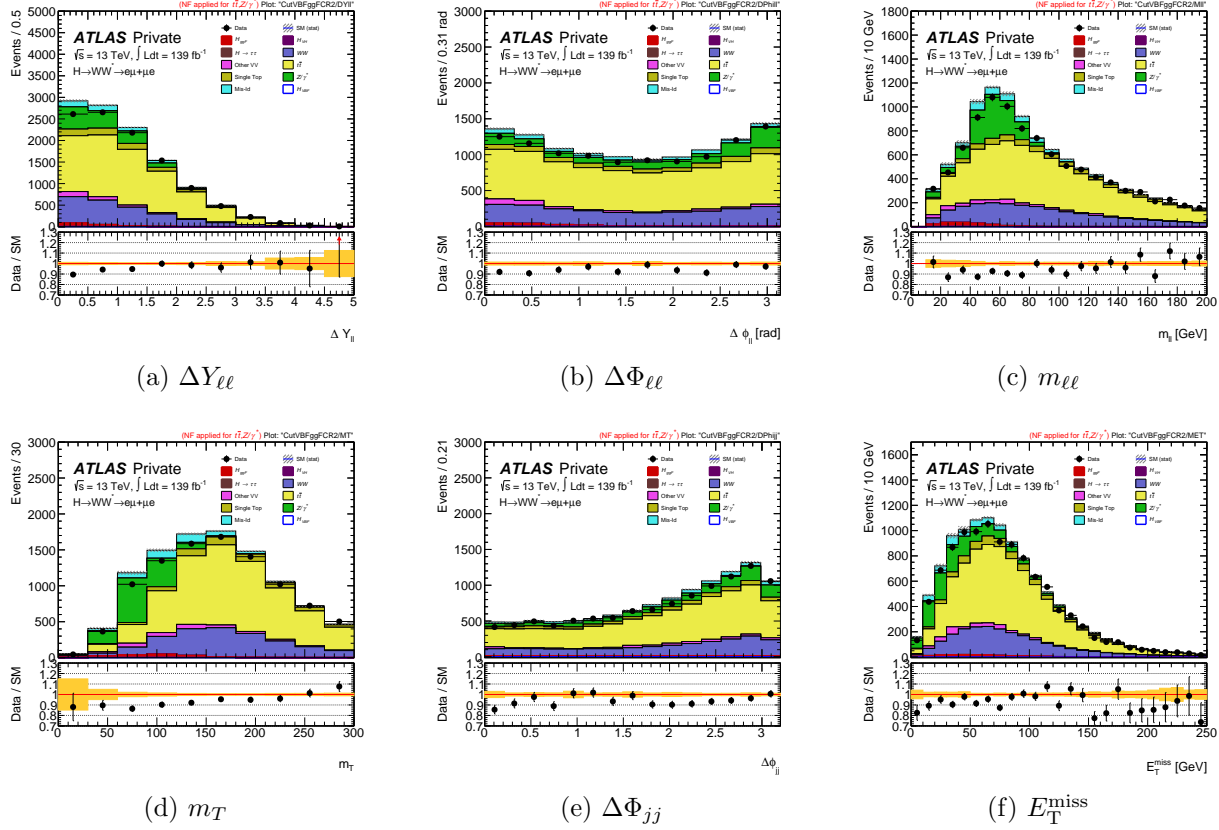


Figure 6.14: Distributions of $\Delta Y_{\ell\ell}$, $\Delta \Phi_{\ell\ell}$, $m_{\ell\ell}$, m_T , $\Delta \Phi_{jj}$, and E_T^{miss} in the ggF CR2 used as input to the BDT discriminating ggF from all other samples.

Discriminant in ggF-CR3

The ggF CR3 is the only region which requires less than two jets. The training discriminates ggF events from all other samples within the ggF CR3 and very high statistics: 200,000 un-weighted (4,000 weighted) ggF events and about 2,800,000 un-weighted (10,000 weighted) other events. The training uses 1,000 trees and only four variables to take advantage of the high statistics. Training parameters are listed in Table 6.7.

The training variables include $\Delta Y_{\ell\ell}$, $\Delta \Phi_{\ell\ell}$, $m_{\ell\ell}$, and m_T . Distributions for these variables in the ggF CR3 region are shown in Figure 6.19 and demonstrate data/MC modeling.

CHAPTER 6. BACKGROUNDS AND SYSTEMATICS

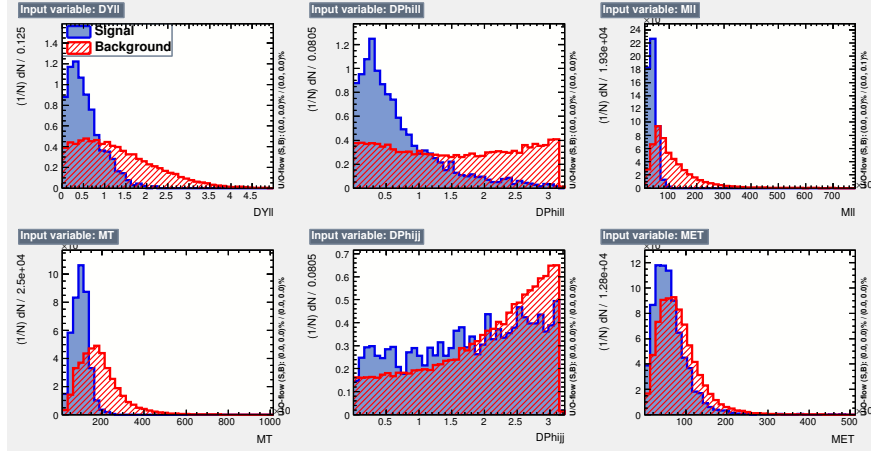


Figure 6.15: Distributions of input variables to ggF CR2 BDT. Samples are weighted and normalized to even numbers of background and signal events. Signal represents ggF and background all other samples [53].

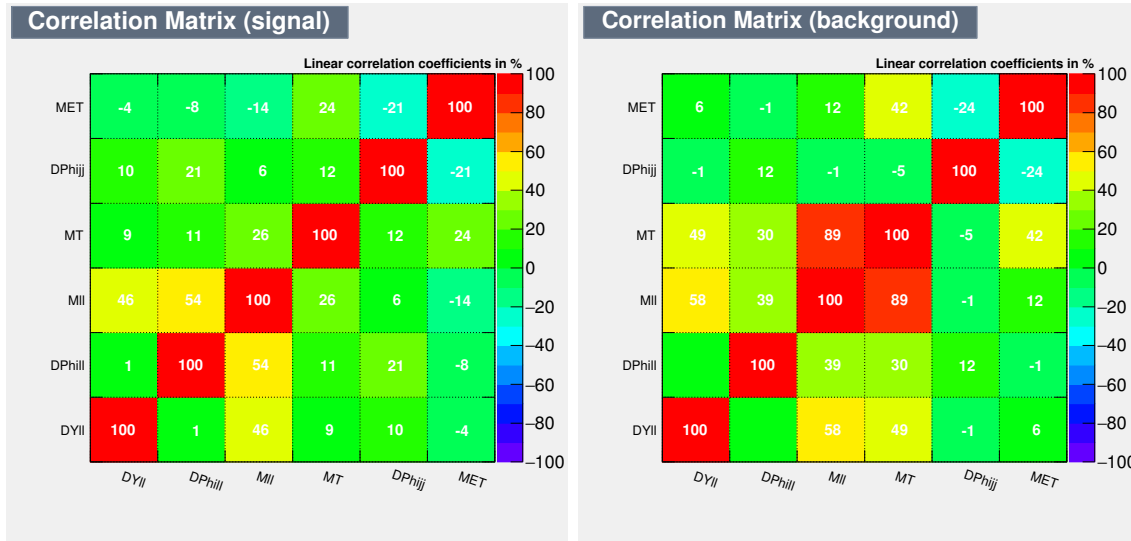


Figure 6.16: Correlations of input variables to ggF CR2 BDT. Signal represents ggF and background all other samples [53].

CHAPTER 6. BACKGROUNDS AND SYSTEMATICS

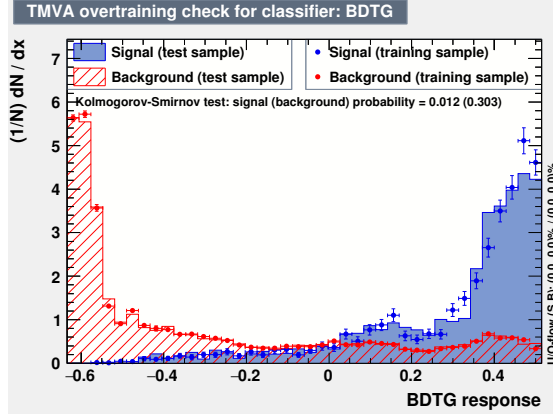


Figure 6.17: Weighted, normalized samples of ggF (signal) and all other samples (background) plotted over BDT output distribution, overlaid testing and training samples shown [53].

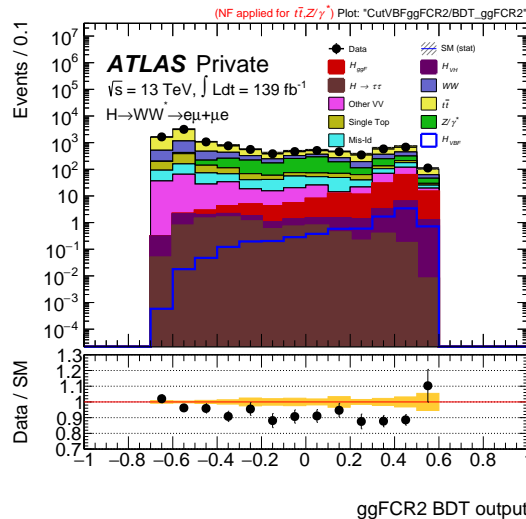


Figure 6.18: Full weighted samples of ggF signal and all other backgrounds plotted over BDT output distribution after ggF CR2 cuts [53].

CHAPTER 6. BACKGROUNDS AND SYSTEMATICS

Parameter	Value
Boosting algorithm	Gradient
Maximum tree depth	10
Number of trees	1000
Minimum number of events requires per mode	5%
Number of cuts	7

Table 6.7: BDT parameters used for the ggF CR3 training.

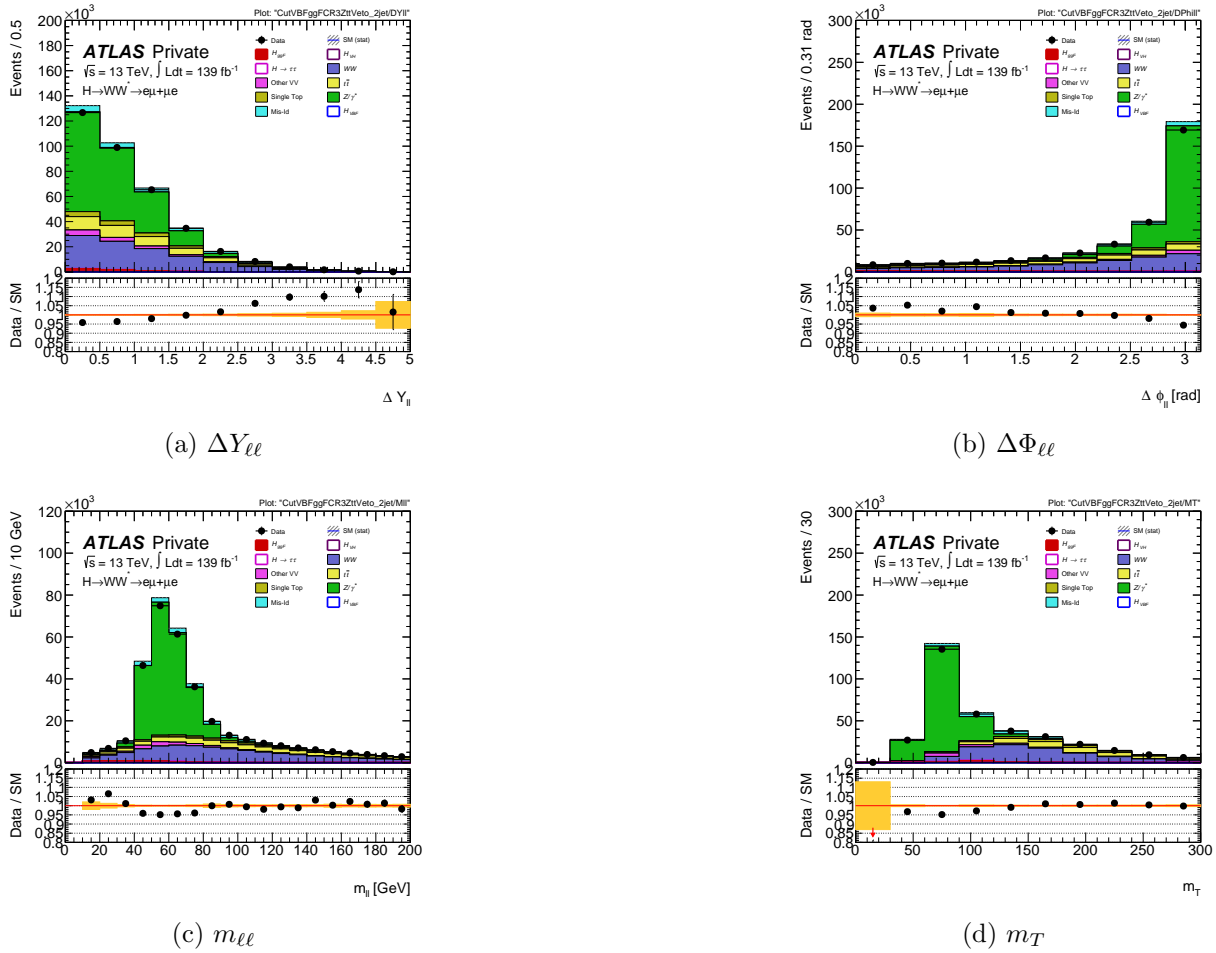


Figure 6.19: Distributions of $\Delta Y_{\ell\ell}$, $\Delta \Phi_{\ell\ell}$, $m_{\ell\ell}$, and m_T in the ggF CR3 used as input to the BDT discriminating ggF from all other samples.

Figures 6.20 and 6.21 demonstrate the input distributions used to train the BDT and their correlations where each distribution is normalized to equal number of background and

CHAPTER 6. BACKGROUNDS AND SYSTEMATICS

signal events.

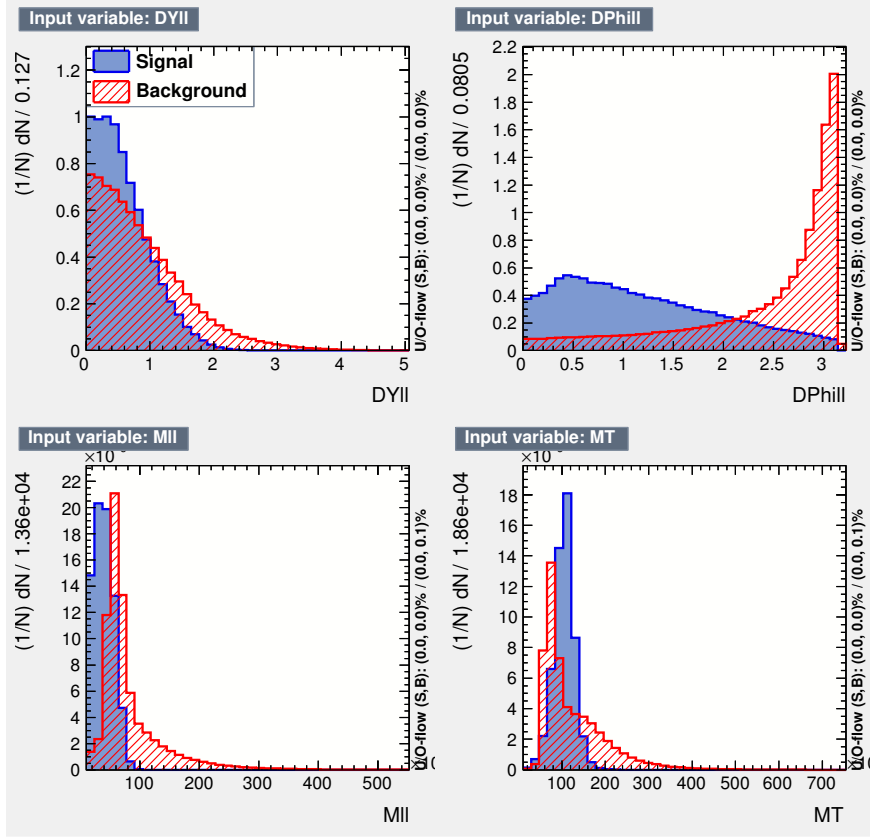


Figure 6.20: Distributions of input variables to the ggF CR3 BDT. Samples are weighted and normalized to even numbers of background and signal events. Signal represents ggF and background all other samples [53].

The discrimination is quantified using the integrated-ROC and calculated at 0.888, which shows good separation. Comparisons between the test and training show that the BDT is un-biased, and KS-test values of 0.276 (0.673) for signal (background) support this. The BDT output variable is visualized both on weighted normalized samples and on samples with full event weights applied in Figures 6.22 and 6.23.

CHAPTER 6. BACKGROUNDS AND SYSTEMATICS

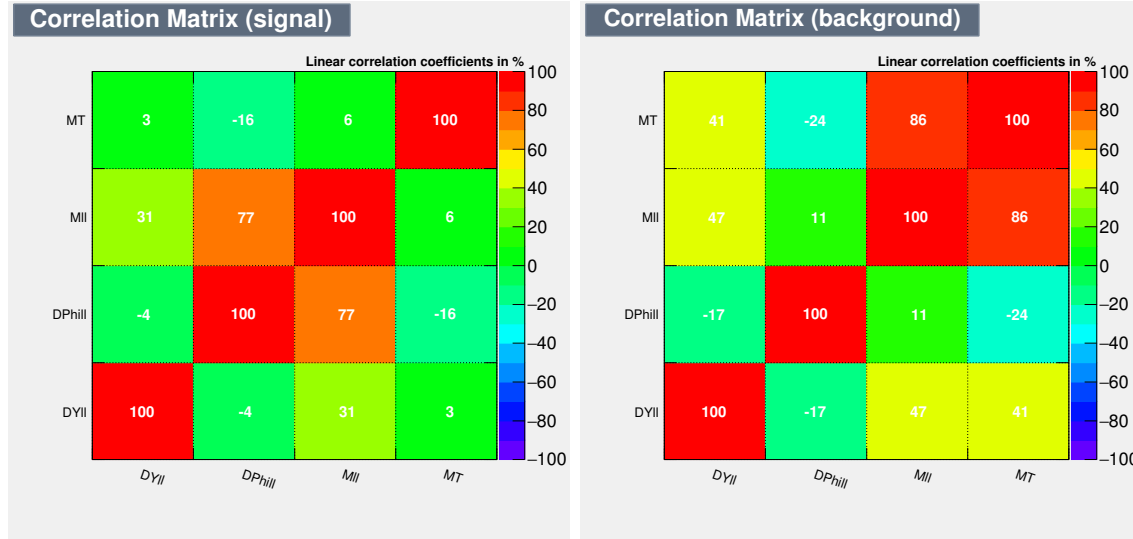


Figure 6.21: Correlations of input variables to the ggF CR3 BDT. Signal represents ggF and background all other samples [53].

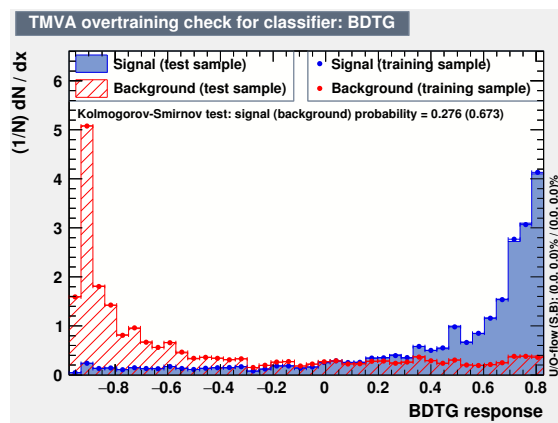


Figure 6.22: Normalized samples of ggF (signal) and all other samples (background) plotted over BDT output distribution, overlaid testing and training samples shown [53].

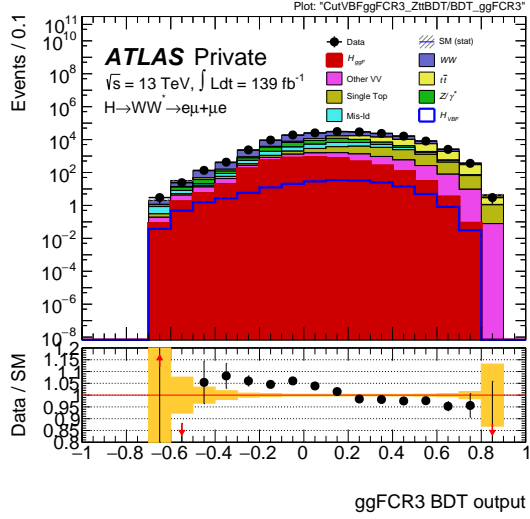


Figure 6.23: Full weighted samples of ggF signal and all other backgrounds plotted over BDT output distribution after ggF CR3 cuts.

Discriminant for ggF and VBF in the signal region

There is one final multivariate discriminant used to discriminate ggF backgrounds. This BDT is trained to differentiate ggF and VBF events in the signal region. Roughly 6,000 un-weighted (60 weighted) ggF events and 95,000 un-weighted (80 weighted) signal events. Training parameters for the ggF vs. VBF BDT are summarized in Table 6.8.

Parameter	Value
Boosting algorithm	Gradient
Maximum tree depth	10
Number of trees	300
Minimum number of events requires per mode	5%
Number of cuts	7

Table 6.8: BDT parameters used for the ggF vs. VBF training.

Seven distributions are used to take advantage of differences in distributions between ggF and VBF events. These variables include ΔY_{jj} , $\Delta \Phi_{jj}$, m_T , p_T^{j0} , p_T^{j1} , \sum centralities, and $\sum M_{lj}$. Figures 6.24 and 6.25 demonstrate the input distributions used to train the BDT

CHAPTER 6. BACKGROUNDS AND SYSTEMATICS

and their correlations where each distribution is normalized to equal number of background and signal events.

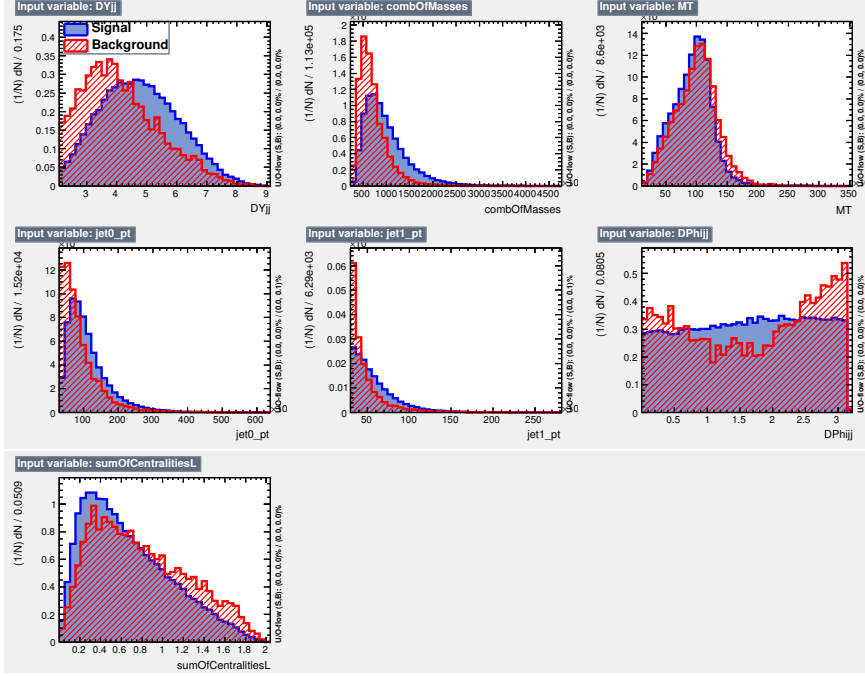


Figure 6.24: Distributions of input variables to the ggF vs. VBF BDT. Samples are weighted and normalized to even numbers of background and signal events. Signal represents VBF and background ggF samples [53].

The integrated-ROC calculated for this BDT is 0.785, which shows moderate discrimination. KS test values of 0.008 (0.047) for signal (background) show no evidence of bias. The BDT output variable is shown both on weighted normalized samples and on samples with full event weights applied in Figures 6.26 and 6.27.

6.1.5 Fake backgrounds

One last substantial background in the VBF HWW cross-section measurement is from mis-identified leptons. These are jets that are mistakenly identified as leptons in reconstruction and in this analysis these predominantly come from $W + \text{jet}$ events. In these events a

CHAPTER 6. BACKGROUNDS AND SYSTEMATICS

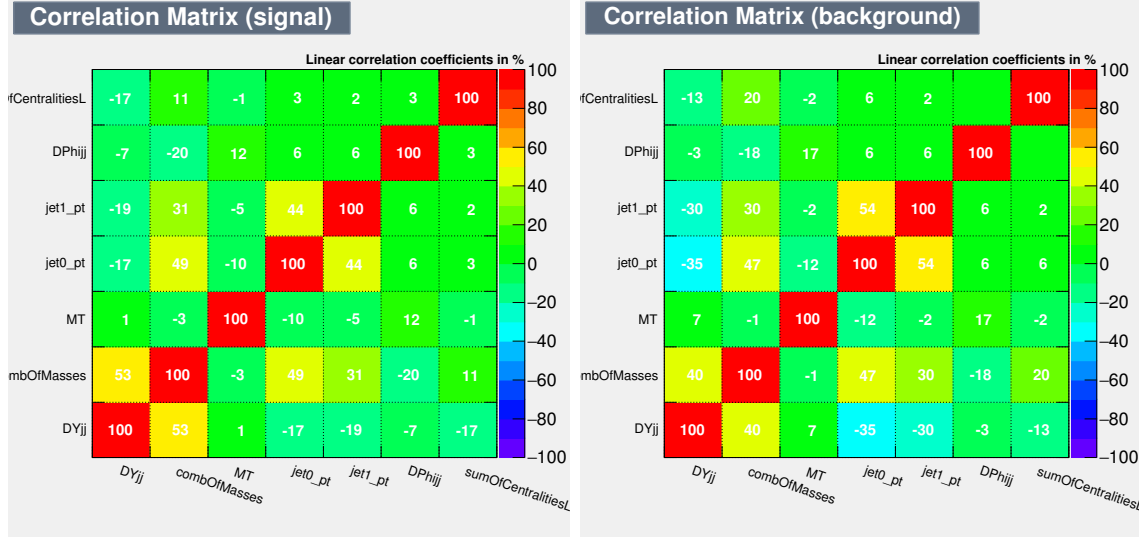


Figure 6.25: Correlations of input variables to the ggF vs. VBF BDT. Signal represents VBF and background ggF samples [53].

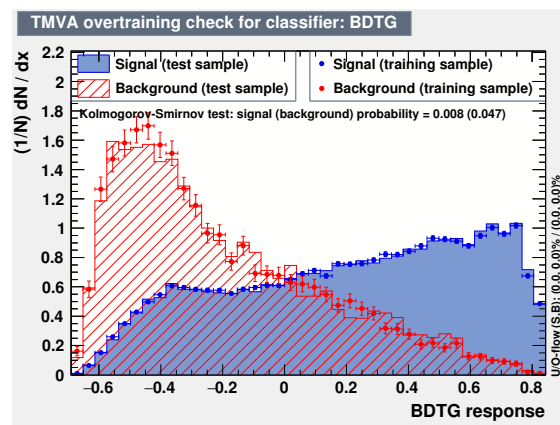


Figure 6.26: Normalized samples of VBF (signal) and ggF (background) plotted over BDT output distribution, overlaid testing and training samples shown.

CHAPTER 6. BACKGROUNDS AND SYSTEMATICS

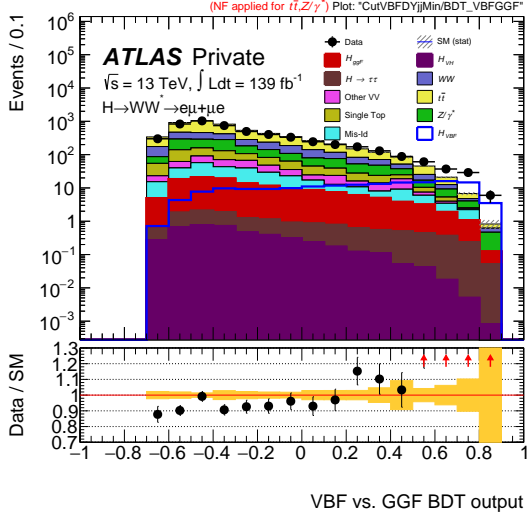


Figure 6.27: Full weighted samples of VBF signal and ggF background plotted over BDT output distribution after SR cuts.

W boson decays leptonically leading to one true lepton and one mistaken lepton, which is actually a jet from the primary vertex. This event mirrors our desired two lepton signature and so creates an additional HWW background sample. This background is estimated with the same methodology used in the 2015–2016 HWW coupling measurement [15], referred to as the fake factor method. Further detail on the overall fake factor method and its mathematical formulation can be found in Ref. [57] while further details on HWW-specific fake background studies are discussed in Ref. [15]. In this section I will give a brief summary of how the so-called “fake background” is estimated.

The fake background is estimated using data measured in a region defined by signal region cuts with one important distinction—one or both of the leptons used are “anti-identified”, meaning they pass some looser lepton identification criteria and not that used in the analysis signal region. These fakes are then extrapolated to the true signal region (with two “identified” leptons) using “fake factors”. Fake factors are defined as the ratio of identified to anti-identified leptons and measured as functions of p_T and η in jet-enriched $Z+\text{jets}$ sam-

CHAPTER 6. BACKGROUNDS AND SYSTEMATICS

ples. The fake backgrounds can be considered split between “single-fake” (with one “anti-ID” lepton) from the predominant $W+\text{jets}$ background and “double-fake” (with two “anti-ID” leptons) from QCD processes. The total signal sample can be defined as:

$$N_{id+id} = N_{id+id}^{EW} + N_{id+id}^{W+jets} + N_{id+id}^{QCD}, \quad (6.3)$$

so that the total events include all electroweak processes (N_{id+id}^{EW}) as well as fake backgrounds from $W+\text{jets}$ and QCD events. In order to estimate the total fake background in the signal region, we need to estimate the number of $W+\text{jets}$ and QCD events in “id+anti-id” events and then apply the fake factor to extrapolate into the “id+id” region. The $N_{id+anti-id}$ for fake backgrounds is calculated after subtraction of electroweak backgrounds (two true leptons that contaminate the “id+anti-id region”) from Monte Carlo simulations as follows:

$$N_{id+anti-id}^{W+jets} + N_{id+anti-id}^{QCD} = N_{id+anti-id} - N_{id+anti-id}^{EWMC}. \quad (6.4)$$

Fake factors are derived from $Z+\text{jets}$ samples and then applied to $W+\text{jets}$ regions so the differences between these two samples are important to understand fully. The fake factor, FF, is defined as

$$FF = \frac{N_{id}}{N_{anti-id}} \quad (6.5)$$

and is measured separately for electron and muons in bins of η and p_T . Table 6.9 summarizes “id” and “anti-id” requirements. $Z+\text{jets}$ event are selected to contain exactly three loosely identified leptons with $p_T > 15$ GeV. They also need to contain an opposite sign ee or $\mu\mu$ lepton pair with $7 < m_{\ell\ell} < 110$ GeV. Both lepton candidates from the Z decay must be “identified” so that the third is the fake candidate. An additional WZ veto is applied using $m_T > 50$ GeV to mitigate electroweak background in the $Z+\text{jets}$ sample. Dedicated MC

CHAPTER 6. BACKGROUNDS AND SYSTEMATICS

Table 6.9: Requirements for “identified” and “anti-identified” electrons and muons.

“id” electron	“anti-id” electron	“id” muon	“anti-id” muon
$p_T > 15 \text{ GeV}$			$p_T > 15 \text{ GeV}$
$ \eta < 2.47$, excluding $1.37 < \eta < 1.52$			$ \eta < 2.45$
$ z_0 \sin\theta < 0.5 \text{ mm}$			$ z_0 \sin\theta < 0.5 \text{ mm}$
Pass <i>Tight</i> if $p_T < 25 \text{ GeV}$	Pass <i>Loose</i>	Pass <i>Tight</i>	Pass <i>Medium</i>
Pass <i>Medium</i> if $p_T > 25 \text{ GeV}$	Pass <i>Loose</i>	Pass <i>Tight</i>	Pass <i>Medium</i>
$ d_0 \sigma(d_0) < 5$			$ d_0 \sigma(d_0) < 3$
Pass FixedCutTrackCone40 if $p_T < 25 \text{ GeV}$		$E_T^{\text{cone}20}/p_T < 0.09$	
Pass IsoGradient if $p_T < 25 \text{ GeV}$		$p_T^{\text{varcone}30}/p_T < 0.06$	
	Veto against identified electron		Veto against identified muon

Table 6.10: Fake factors binned for muons and electrons in p_T and η with their statistical uncertainties

$p_T(\text{GeV})$	Muon FF ($ \eta < 1.5$)	Muon FF ($1.5 < \eta < 2.5$)	Electron FF
15–25	0.038 ± 0.004	0.057 ± 0.005	0.079 ± 0.005
20–25	0.021 ± 0.007	0.036 ± 0.008	0.097 ± 0.001
25–35	0.029 ± 0.011	0.064 ± 0.014	0.157 ± 0.017
35–inf	0.049 ± 0.023	0.110 ± 0.040	0.190 ± 0.026

simulations model electroweak backgrounds in the $Z + \text{jets}$ region and include $V + \gamma$, diboson (WW , WZ , and ZZ), single top and $t\bar{t}$. WZ backgrounds are normalized to their measured cross-sections. Fake yields for the $Z + \text{jets}$ samples are finally calculated by subtracting MC electroweak backgrounds from data.

The fake factor is computed as a ratio between “id” and “anti-id” leptons and is binned in p_T , [15, 20, 25, 35, inf], and for muons also in η , [0, 1.5, 2.5], excluding the electromagnetic calorimeter crack region. Table 6.10 summarizes fake factors used in this analysis.

Further studies on fake factors include comparisons to their MC simulation expectations and studies on differences between the $Z + \text{jets}$ control sample used to calculate fake factors and the $W + \text{jets}$ sample on which they are applied. These studies are beyond the scope of this thesis but support the use of the fake factor method in our analysis. Specifically, jet kinematics and heavy flavor fraction in both samples are studied by the HWW coupling analysis group and factor into a correction factor applied to transfer between $Z + \text{jets}$ and

CHAPTER 6. BACKGROUNDS AND SYSTEMATICS

$W+jets$ samples. More information on these studies and correction factors can be found in Ref. [15].

The $W+jets$ control region is defined as in the signal region, with cuts specifying at least 2 jets, a b -veto, $m_{\tau\tau}$ based Z-veto, an opposite lepton veto, central jet veto, and cuts on m_{jj} and ΔY_{jj} . Unlike the signal region, this region specifies one “id” and one “anti-id” lepton instead of two identified leptons. The cutflow for this region is shown below where fakes are defined from the subtraction of total electroweak background from data. Once fake factors are applied, these events constitute the fake background estimate in the signal region. Fake purity in this control region is 74% after all signal region-like cuts are applied.

$\sqrt{s} = 13TeV, \mathcal{L} = 139fb^{-1}$ (Full Run 2)	Total Bkg	Data	Fakes	Fake purity(%)
Channel Selection	8116768.84 ± 3042.09	13124937	5008168.16 ± 4730.67	38.16 ± 0.04
Trigger Selection	8116768.84 ± 3042.09	13124937	5008168.16 ± 4730.67	38.16 ± 0.04
Trigger Matching	7906126.65 ± 2917.00	13057932	5151805.35 ± 4644.01	39.45 ± 0.04
$W+jets$ flavour split muon	5896841.78 ± 2703.75	10572340	4675498.22 ± 4228.78	44.22 ± 0.04
$W+jets$ flavour split electron	3791849.84 ± 2494.76	7417426	3625576.16 ± 3693.41	48.88 ± 0.05
Jet Cleaning	3791849.84 ± 2494.76	7417426	3625576.16 ± 3693.41	48.88 ± 0.05
Overlap: Vgamma/Vjets	3791849.84 ± 2494.76	7417426	3625576.16 ± 3693.41	48.88 ± 0.05
Only two Leptons	3754720.02 ± 2485.95	7376514	3621793.98 ± 3681.91	49.10 ± 0.05
$p_t^{lead} > 22$ GeV	3754720.02 ± 2485.95	7376514	3621793.98 ± 3681.91	49.10 ± 0.05
$p_t^{\text{sublead}} > 15$	3753322.61 ± 2485.49	7373346	3620023.39 ± 3681.17	49.10 ± 0.05
OS Leptons	3751223.46 ± 2483.45	7365693	3614469.54 ± 3678.75	49.07 ± 0.05
$M_{\ell\ell} > 12/10$ GeV	3751147.28 ± 2483.41	7365336	3614188.72 ± 3678.68	49.07 ± 0.05
SF: Z Veto	3751147.28 ± 2483.41	7365336	3614188.72 ± 3678.68	49.07 ± 0.05
Leptons ID-anti-ID	780838.94 ± 837.46	1931616	1150777.06 ± 1622.64	59.58 ± 0.09
2-jet (30,30) fJVT	384692.76 ± 242.92	657536	272843.24 ± 846.49	41.49 ± 0.14
b-veto	62361.10 ± 199.23	198158	135796.90 ± 487.70	68.53 ± 0.29
CJV (20GeV)	43093.51 ± 171.93	137885	94791.49 ± 409.20	68.75 ± 0.35
OLV bool	9162.00 ± 78.28	28068	18906.00 ± 184.92	67.36 ± 0.77
$Z \rightarrow \tau\tau$ veto	5142.69 ± 60.99	18069	12926.31 ± 147.61	71.54 ± 0.97
$M_{jj} > 200$	3233.48 ± 51.55	11911	8677.52 ± 120.70	72.85 ± 1.21
$DY_{jj} > 2.1$	2838.02 ± 50.56	10904	8065.98 ± 116.02	73.97 ± 1.28

Table 6.11: Cutflow in the $W+jets$ control region. Lepton ID/anti-ID describes the selection of fake candidates with either one or two “anti-id” leptons

Distributions shown in Figure 6.28 show the electroweak background processes (blue) in the fake control region along with data (black). The $W+jets$ or fake background is taken as the difference between data and EW background and shown in the plots as light blue points. This selection achieves high purity of the “fake background” sample which, along with fake

CHAPTER 6. BACKGROUNDS AND SYSTEMATICS

factors, is used to estimate fakes contaminating our signal region.

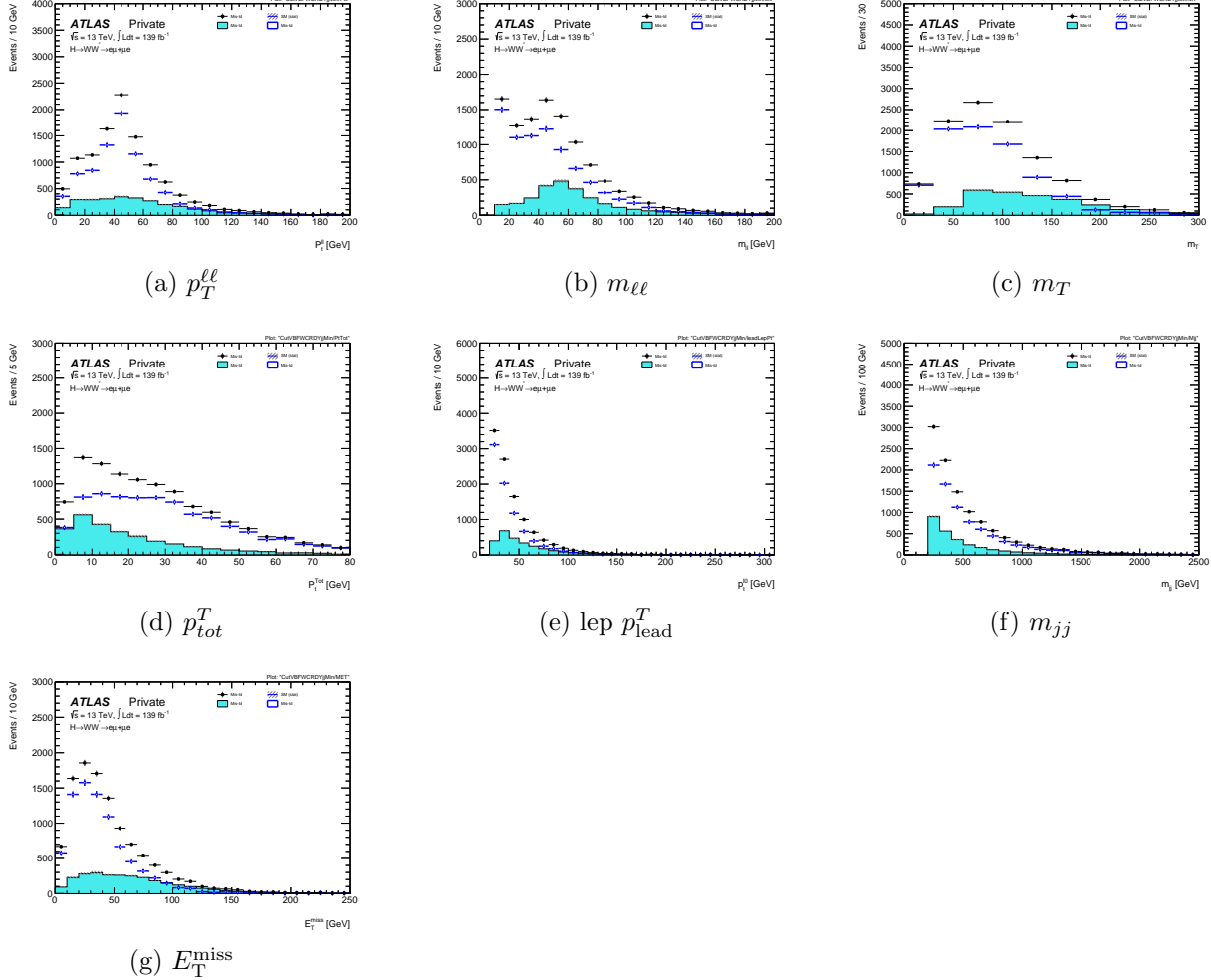


Figure 6.28: Distributions of $p_T^{\ell\ell}$, $m_{\ell\ell}$, m_T , p_{tot}^T , lep p_{lead}^T , lep $p_{sublead}^T$, m_{jj} , and E_T^{miss} in the differential VBF W +jets control region.

6.2 Systematic uncertainties

The experimental, theoretical, and statistical uncertainties in this analysis all impact the final measurement substantially. In this section I describe both the experimental and

CHAPTER 6. BACKGROUNDS AND SYSTEMATICS

theoretical systematic uncertainties in detail. Statistical uncertainties are derived from the limited number of MC events used to model each of signal and background samples in the fiducial cross-section measurement. A single MC-stat nuisance parameter is implemented based on Poisson statistics and used in our overall statistical fit.

6.2.1 Experimental uncertainties

Several types of experimental systematics uncertainties affect this analysis. Each systematic estimate follows the current prescriptions from performance groups and can be split into those derived for muons, electrons, Jet/ E_T^{miss} , Trigger, flavor tagging and pile-up. The current set of experimental systematics uses 102 nuisance parameters, each briefly described with their associated names in Table 6.12. The impact of these systematics on our overall result, as well as their ranking and interpretation, is included in the next Chapter 7.

Systematic uncertainties on the energy of jets and electrons as well as on the momentum of muons are based on scale and resolution values. These uncertainties are evaluated by testing the number of events in the final state affected by shifting energy/momentun by a scale factor. This “smearing” procedure is done for a nominal scaling value and values with $\pm 1\sigma$. Systematic uncertainty on scale factors is calculated by comparing nominal event numbers to those after particular weights are applied. These weights are derived from data-MC agreement and their uncertainty is the relative difference between nominal and modified weight sums.

There are four nuisance parameters associated with muon reconstruction and identification. Muon momentum resolution uncertainties are divided into those from the Inner Detector and those from the muon spectrometer. Muon momentum scale uncertainties are contained in one parameter and two additional systematic uncertainties come from a correc-

CHAPTER 6. BACKGROUNDS AND SYSTEMATICS

tion applied to muons to account for residual ID/MS misalignments which create a charge dependent bias. Two nuisance parameters account for muon isolation uncertainties and an additional two account for muon trigger uncertainties [31].

Electron reconstruction and identification uncertainties are contained in 35 recommended nuisance parameters. There are three additional standard systematics included for electron energy scale and resolution and a final two are included for electron isolation and trigger efficiency [30].

There are a number of jet energy scale and resolution systematics in the analysis including parameters to estimate energy scale and resolution uncertainties, b -jet scale and efficiency uncertainties, flavor composition, response, energy scale dependence on pile-up, and η calibrations [39].

Systematics from the pileup $\langle \mu \rangle$ value are determined by varying the data scale factor and are accounted for with one overall nuisance parameter (though pile-up effects on jets are considered independently). Overall integrated luminosity uncertainty is $\pm 1.7\%$ as calculated for the complete 2015-2018 dataset [58].

6.2.2 Theoretical uncertainties

Theoretical uncertainties determine the accuracy of each of our Monte Carlo generated signal and background samples and are evaluated per sample rather than on reconstructed physics objects. In this analysis, theoretical uncertainties are calculated and included in our overall fit for VBF signal and ggF, top, WW and $Z \rightarrow \tau\tau$ background events. For this measurement, I use global normalization uncertainties estimated within the signal region, which are dominant over shape effects. In this section, I will briefly discuss the uncertainties associated with each sample and show how they affect the cross-section measurement. Their

CHAPTER 6. BACKGROUNDS AND SYSTEMATICS

Systematic uncertainty	Short description
	Event
Luminosity PRW_DATASF	uncertainty on total integrated luminosity uncertainty on pileup reweighting
	Electrons
EL_EFF_Trigger_Total_1NPCOR_PLUS_UNCOR EL_EFF_Reco_Total_1NPCOR_PLUS_UNCOR EL_EFF_ID_CorrUncertaintyNP (0 to 15) EL_EFF_ID_SIMPLIFIED_UncorrUncertaintyNP (0 to 17) EL_EFF_Iso_Total_1NPCOR_PLUS_UNCOR EG_SCALE_ALL EG_SCALE_AF2	trigger efficiency uncertainty reconstruction efficiency uncertainty ID efficiency uncertainty splits in 16 components ID efficiency uncertainty splits in 18 components isolation efficiency uncertainty energy scale uncertainty
	Muons
MUON_EFF_TrigStatUncertainty MUON_EFF_STAT MUON_EFF_SYS MUON_EFF_STAT_LOWPT MUON_EFF_SYST_LOWPT TMUON_ID MUON_MS MUON_SCALE MUON_SAGITTA_RHO MUON_SAGITTA_RESBIAS	trigger efficiency uncertainty reconstruction and ID efficiency uncertainty for muons with $p_T > 20$ GeV reconstruction and ID efficiency uncertainty for muons with $p_T \leq 20$ GeV momentum resolution uncertainty from inner detector momentum resolution uncertainty from muon system momentum scale uncertainty charge dependent momentum scale uncertainty
	Jets
JET_EffectiveNP_Detector (1 to 2) JET_JER_EffectiveNP_ (1 to 7) JET_JER_DataVsMC JET_BJES_Response JET_EffectiveNP_Mixed (1 to 3) JET_EffectiveNP_Modelling (1 to 4) JET_EffectiveNP_Statistical (1 to 6) JET_EtaIntercalibration_NonClosure_negEta JET_EtaIntercalibration_NonClosure_posEta JET_EtaIntercalibration_TotalStat JET_Pileup_OffsetMu JET_Pileup_OffsetNPV JET_Pileup_PtTerm JET_Pileup_RhoTopology JET_Flavor_Composition JET_Flavor_Response JET_PunchThrough_MC16 JET_SingleParticle_HighPt JET_JvtEfficiency FT_EFF_Eigen_B (0 to 2) FT_EFF_Eigen_C (0 to 2) FT_EFF_Eigen_Light (0 to 3) FT_EFF_Eigen_extrapolation FT_EFF_Eigen_extrapolation_from_charm	detector related energy scale uncertainty energy resolution uncertainty energy resolution modeling uncertainty energy scale uncertainty on b-jets energy resolution uncertainty energy scale uncertainty on eta-intercalibration (modeling) statistical resolution uncertainty energy scale uncertainty on eta-intercalibrations (non-closure) energy scale uncertainty on eta-intercalibrations (non-closure) energy scale uncertainty on eta-intercalibrations (statistics/method) energy scale uncertainty on pile-up (mu dependent) energy scale uncertainty on pile-up (NPV dependent) energy scale uncertainty on pile-up (pt term) energy scale uncertainty on pile-up (density ρ) energy scale uncertainty on flavour composition energy scale uncertainty on samples' flavour response energy scale uncertainty for punch-through jets energy scale uncertainty from the behaviour of high- p_T jets JVT efficiency uncertainty <i>b</i> -tagging efficiency uncertainties (“BTAG_MEDIUM”): 3 components for b jets, 3 for c jets and 4 for light jets <i>b</i> -tagging efficiency uncertainty on the extrapolation to high- p_T jets <i>b</i> -tagging efficiency uncertainty on tau jets

Table 6.12: Summary of the experimental systematic uncertainties considered.

CHAPTER 6. BACKGROUNDS AND SYSTEMATICS

impacts on the overall result are further discussed in the next chapter.

Theory uncertainties on VBF Higgs production

The VBF theoretical uncertainties include parton shower, PDF, α_s , and QCD scale. Shower uncertainties are derived from comparisons between different Parton Shower generators (Powheg+Pythia8, nominal, and Powheg+Herwig7) and constitute the largest theoretical uncertainties in the signal region. PDF uncertainties are derived from internal re-weighting within the nominal Powheg+Pythia8 samples, QCD uncertainties include factorization and renormalization scales and are found with an 8-point envelope scheme. VBF signal theory systematics within the signal region, control/validation regions are shown in Table 6.13.

	Impact high / low (+/- stat) [%]
VBF Parton Shower	-8.8 \pm 0.5
VBF QCD Scale	0.9 \pm 0.0 / -0.8 \pm 0.0
VBF PDF	1.7 \pm 0.0
VBF α_s	0.5 \pm 0.3

Table 6.13: VBF theory uncertainties breakdown

We examine these uncertainties for any shape effects on the BDT output used in the final fit. The distributions shown in Figure 6.29 show very little shape effects.

Theoretical uncertainties on ggF Higgs production

The ggF theoretical uncertainties come also include Parton Shower, PDF, α_s , and QCD scale variations. Parton Shower uncertainties use the same prescription described for the VBF samples and similarly constitute the largest theoretical uncertainties from ggF events. PDF uncertainties are derived from internal re-weighting as for VBF and QCD uncertainties include factorization and renormalization scales and are derived using the WG1 scheme [59].

CHAPTER 6. BACKGROUNDS AND SYSTEMATICS

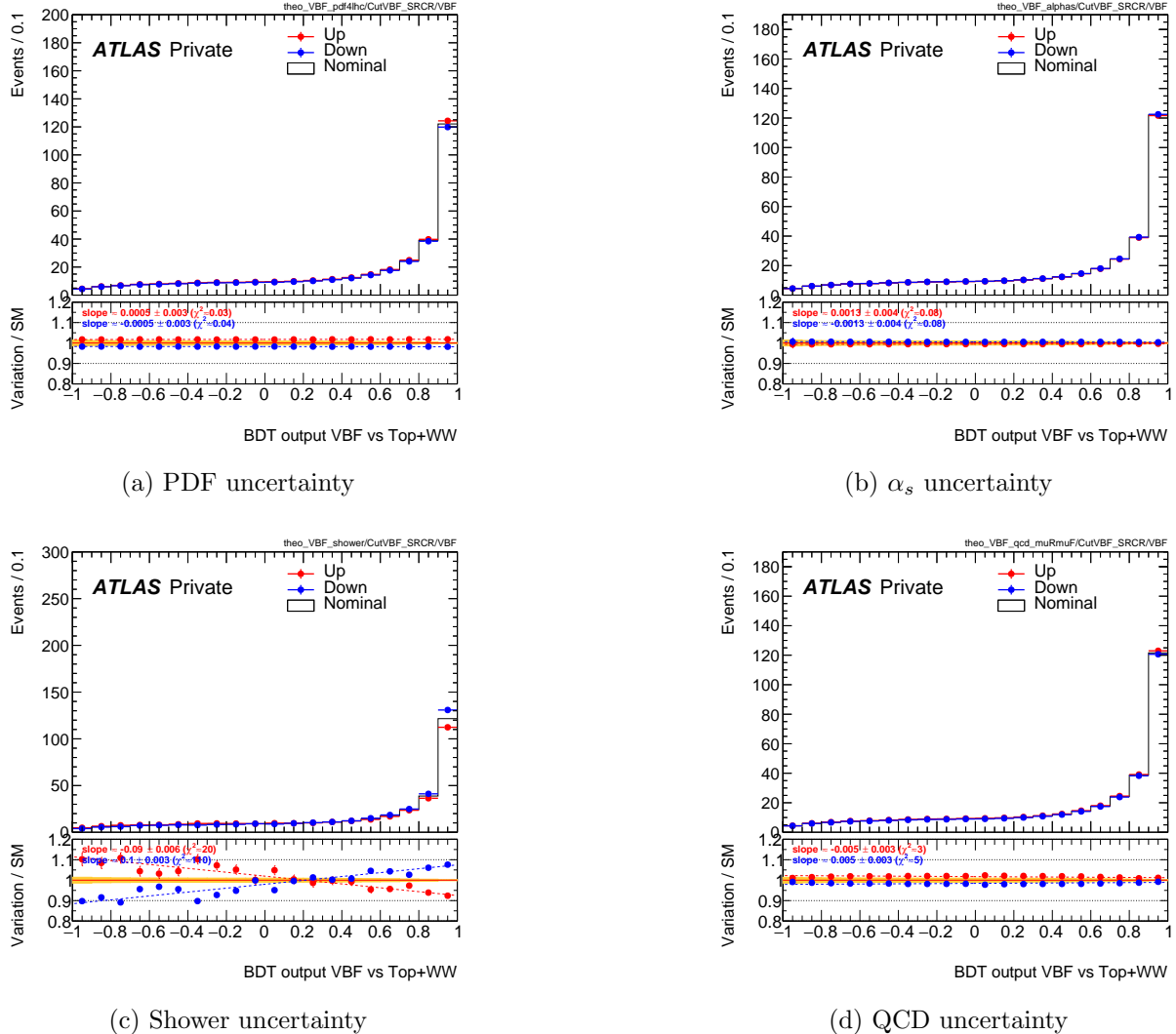


Figure 6.29: Up and down variations shown for four theoretical uncertainties from the VBF signal displayed against the VBF vs. top + WW BDT. The nominal sample is shown in black and slopes are calculated for up and down variations to display any potential linear shape effects. Distributions are shown after all signal region cuts [53].

ggF theory uncertainties derived in the signal and validation regions are shown in Table 6.14.

We examine these uncertainties for any shape effects on the BDT output used in the final fit. Figure 6.30 shows very little shape effects.

CHAPTER 6. BACKGROUNDS AND SYSTEMATICS

	Impact high / low (+/- stat) [%]
ggF PDF	1.7 \pm 0.0
ggF α_s	3.2 \pm 1.3
ggF Parton Shower	-14.4 \pm 1.2
ggF QCD	10.9 \pm 3.9

Table 6.14: ggF theory uncertainties breakdown

Theoretical uncertainties on top decays

The top background considered in this analysis includes $t\bar{t}$ and Wt where $t\bar{t}$ is the dominant sample by far. Theoretical uncertainties are produced for both single top and $t\bar{t}$ independently and both include those from a variety of sources including hard scatter generation, parton shower, factorization and renormalization scales, initial state radiation (ISR), final state radiation (FSR), and PDFs. For parton shower uncertainties, the same scheme used in ggF and VBF samples is used. Hard scatter generation uncertainties are similarly derived from comparing the nominal generation method with aMCatNlo+Pythia8. QCD scale uncertainties from renormalization and factorization are added with a 6-point envelope scheme. ISR and FSR uncertainties are determined through varying internal weights and the PDF uncertainty is completed with internal reweighting and errors produced within the nominal Powheg+Pythia8 samples. Wt events contain one additional systematic uncertainty - interference. This is derived from removing $t\bar{t}$ -like contributions at the level of amplitude (DR) or matrix elements (DS) [60]. Table 6.15 shows theory uncertainty from $t\bar{t}$ events in the signal, control and validation regions while table 6.16 shows the same for Wt . While Wt uncertainties are large, the background has a minimal contribution to the analysis so these do not have a large effect on overall results. **Looking into ttbar uncertainties, slightly larger generator/scale than expected.**

Figure 6.31 shows very little shape effects from theoretical uncertainties on $t\bar{t}$ back-

CHAPTER 6. BACKGROUNDS AND SYSTEMATICS

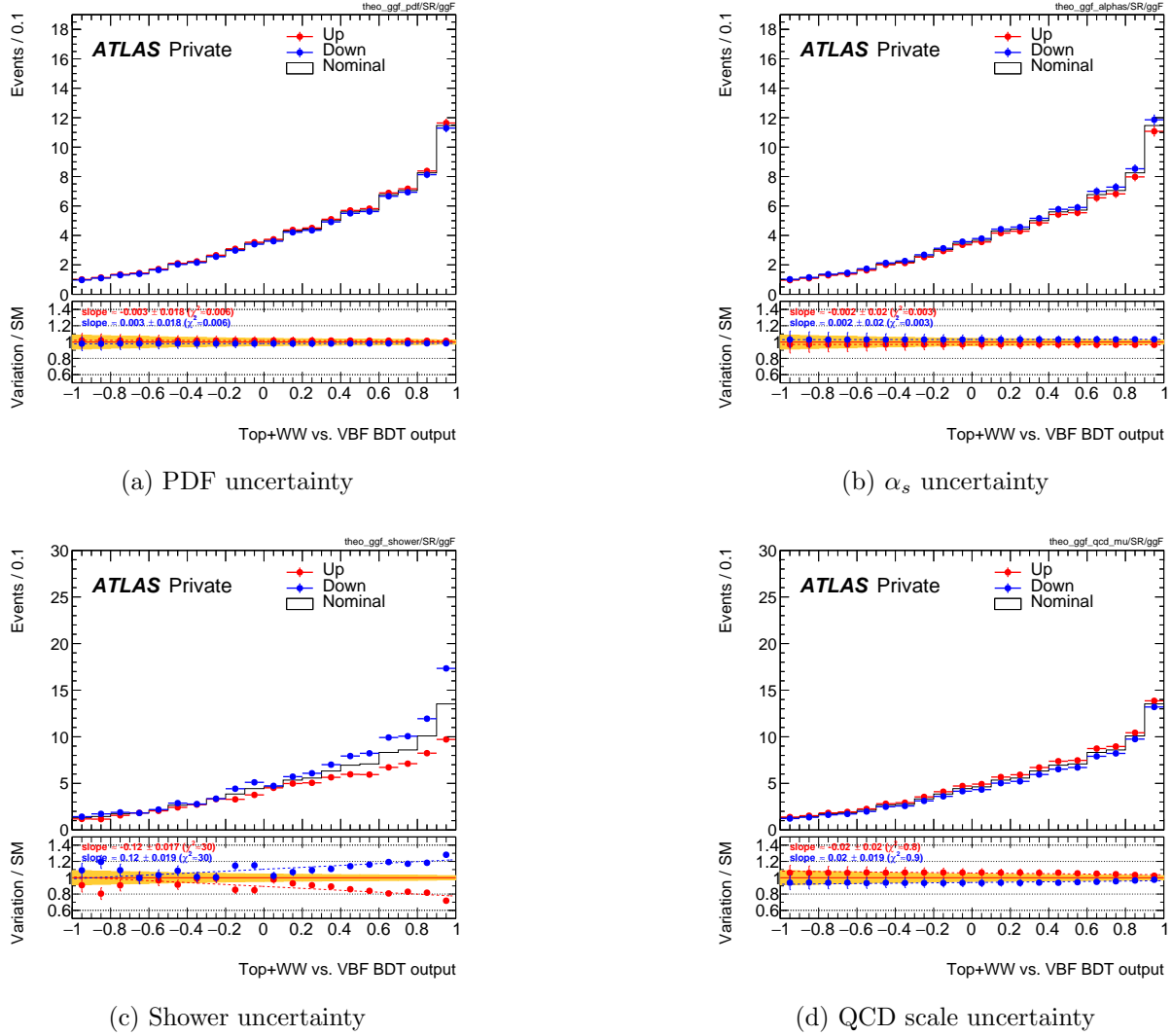


Figure 6.30: Up and down variations shown for four theoretical uncertainties from the ggF background displayed against the VBF vs. top +WW BDT. The nominal sample is shown in black and slopes are calculated for up and down variations to display any potential linear shape effects. Distributions are shown after all signal region cuts.

grounds. Wt distributions have too little statistics in the signal region for theory systematics to have shape effects.

CHAPTER 6. BACKGROUNDS AND SYSTEMATICS

	Impact high / low (+/- stat) [%]
$t\bar{t}$ Parton Shower	4.1 ± 0.6
$t\bar{t}$ Generator	18.3 ± 1.2
$t\bar{t}$ QCD Scale	$13.6 / -12.9$
$t\bar{t}$ ISR	$-0.6 / 0.6$
$t\bar{t}$ FSR	$-1.3 / 2.2$
$t\bar{t}$ PDF	1.9

Table 6.15: $t\bar{t}$ theory uncertainties breakdown

	Impact high / low (+/- stat) [%]
Wt Parton Shower	18.9 ± 3.3
Wt Generator	21.4 ± 4.5
Wt QCD Scale	$5.1 / -5.0$
Wt ISR	$-0.1 / 0.1$
Wt FSR	$-0.2 / 3.9$
Wt Interference	-4.4 ± 2.5
Wt PDF	2.0

Table 6.16: Wt theory uncertainties breakdown

Theoretical uncertainties on WW production

The WW background theoretical uncertainties include PDF, α_s , and QCD scale variations. [Add CKKM uncertainties and generator?](#). PDF uncertainties are derived from internal re-weighting within the nominal Powheg+Pythia8 samples, QCD uncertainties include factorization and renormalization scales, and generator uncertainties are derived from a comparison with $MG5_aMC@NLO$ interfaced with Pythia8 (and so include shower uncertainty). WW theory systematics within the signal region, control/validation regions are shown in Table 6.17.

	Impact high / low (+/- stat) [%]
WW QCD Scale	$20.0 / -14.9$
WW PDF	1.0
WW α_s	2.0

Table 6.17: WW theory uncertainties breakdown

CHAPTER 6. BACKGROUNDS AND SYSTEMATICS

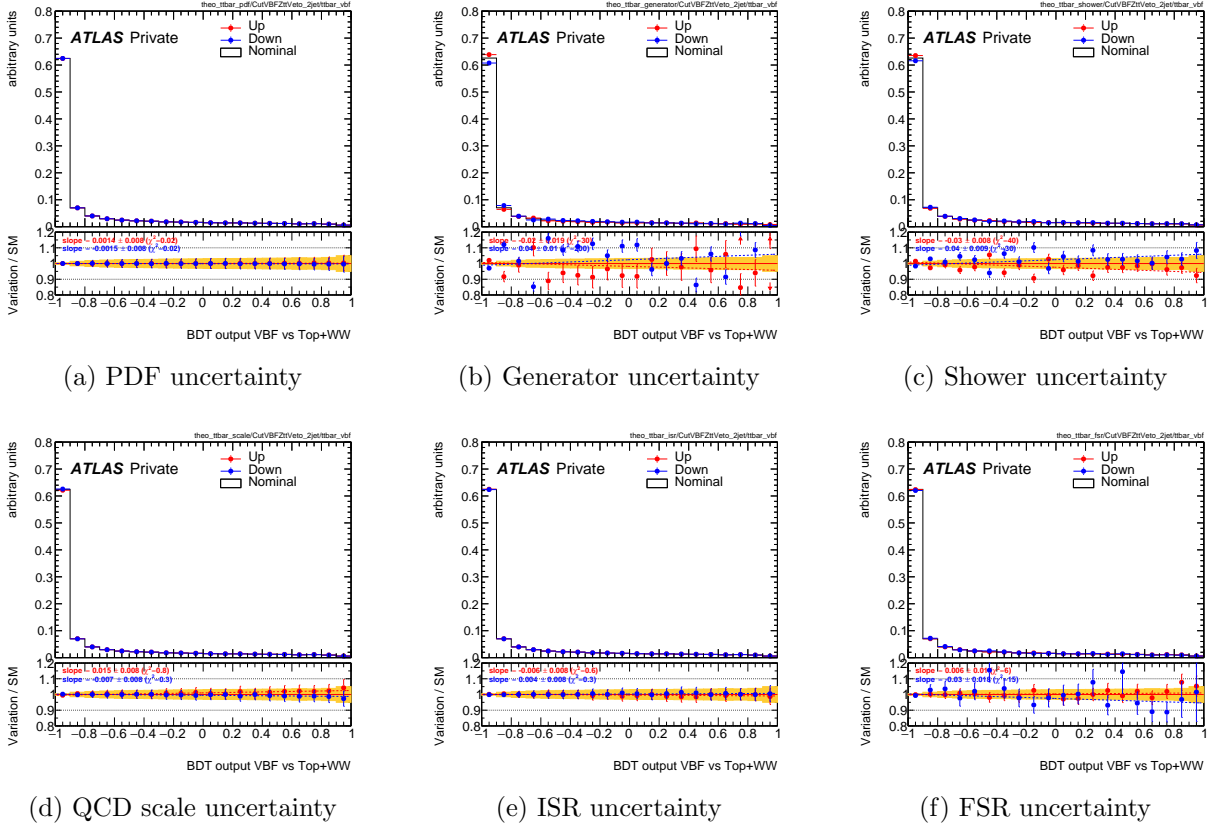


Figure 6.31: Up and down variations shown for four theoretical uncertainties from the $t\bar{t}$ background displayed against the VBF vs. top +WW BDT. The nominal sample is shown in black and slopes are calculated for up and down variations to display any potential linear shape effects. Distributions are shown after all signal region cuts [53].

We examine these uncertainties for any shape effects on the BDT output used in the final fit. Figure 6.32 shows no shape effects.

Theoretical uncertainties on $Z \rightarrow \tau\tau$

The $Z \rightarrow \tau\tau$ theoretical uncertainties include PDF, α_s , QCD scale, and generator variations. PDF uncertainties are derived from internal re-weighting within the nominal Powheg+Pythia8 samples, QCD uncertainties include factorization and renormalization

CHAPTER 6. BACKGROUNDS AND SYSTEMATICS

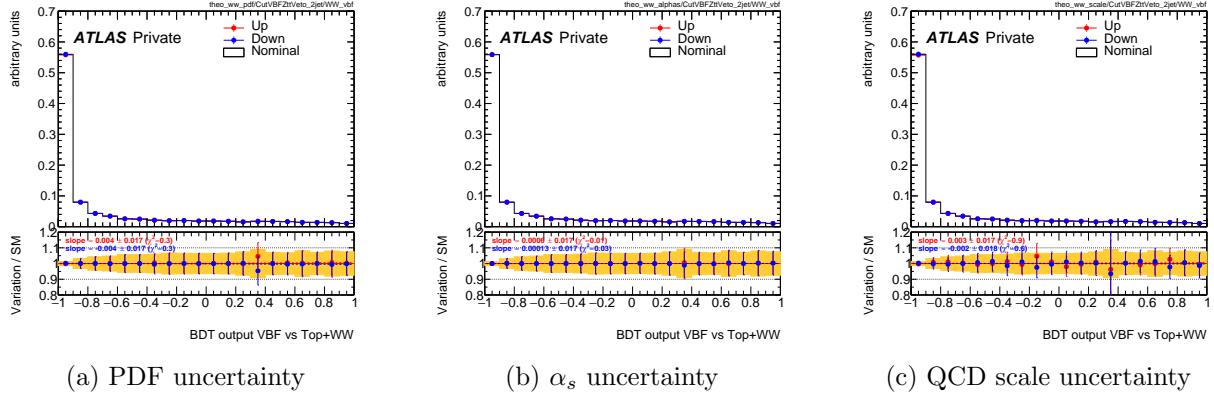


Figure 6.32: Up and down variations shown for four theoretical uncertainties from the WW background displayed against the VBF vs. top + WW BDT. The nominal sample is shown in black and slopes are calculated for up and down variations to display any potential linear shape effects. Distributions are shown after all signal region cuts [53].

scales and use a seven-point envelope, α_s uncertainties use an up-down comparison with two $NNPDF3.0$ NNLO α_s variations, and generator uncertainties are derived from a comparison with $MG5_aMC@NLO$ interfaced with Pythia8. $Z \rightarrow \tau\tau$ theory systematics within the signal region, control/validation regions are shown in 6.18.

	Impact high / low (+/- stat) [%]
$Z \rightarrow \tau\tau$ QCD Scale	6.6 / -5.7
$Z \rightarrow \tau\tau$ PDF	1.6
$Z \rightarrow \tau\tau$ α_s	1.4
$Z \rightarrow \tau\tau$ Generator	-17.2 ± 5.9

Table 6.18: $Z \rightarrow \tau\tau$ theory uncertainties breakdown

We examine these uncertainties for any shape effects on the BDT output used in the final fit. Figure 6.33 shows very little shape effects.

CHAPTER 6. BACKGROUNDS AND SYSTEMATICS

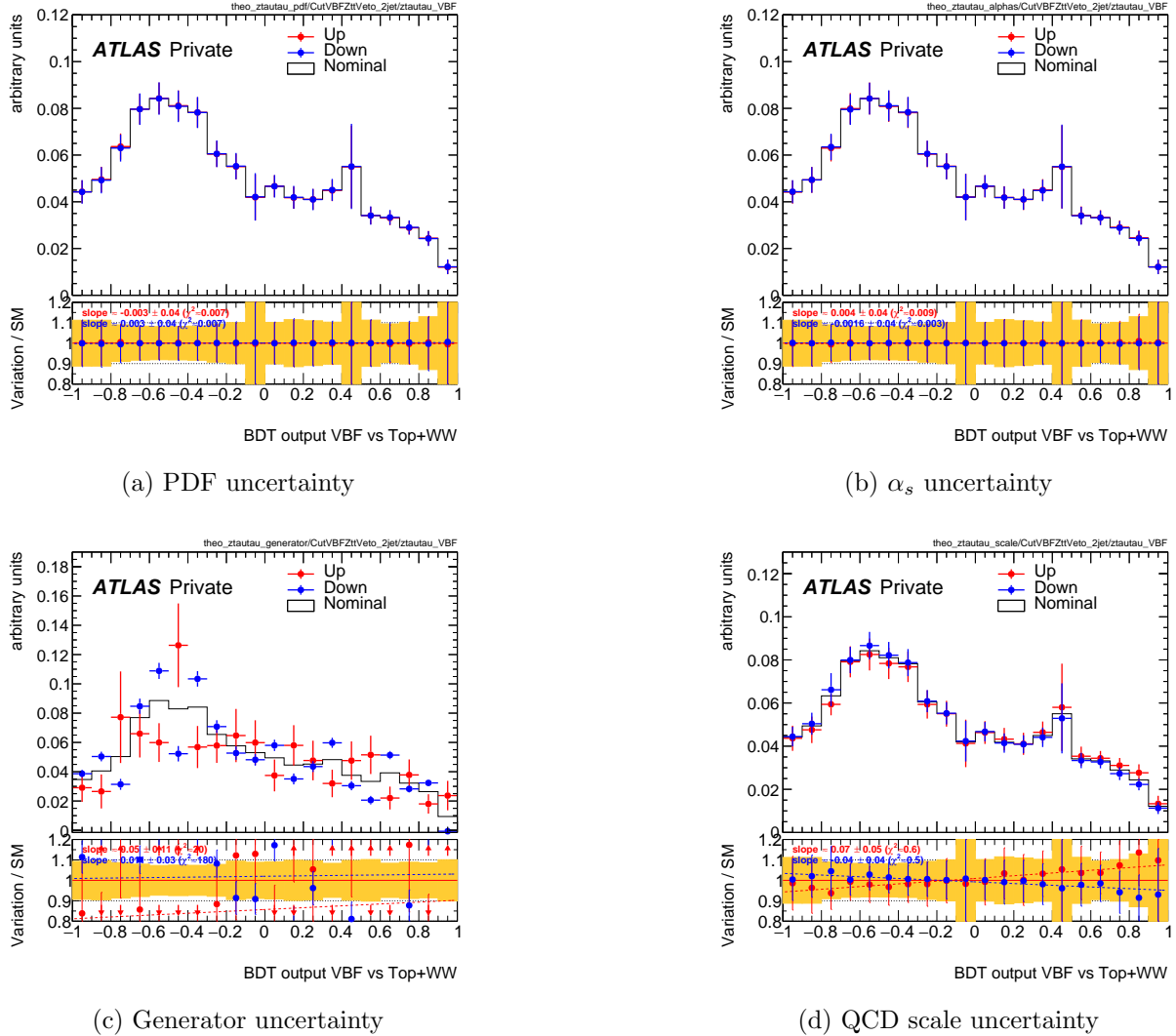


Figure 6.33: Up and down variations shown for four theoretical uncertainties from the $Z \rightarrow \tau\tau$ background displayed against the VBF vs. top +WW BDT. The nominal sample is shown in black and slopes are calculated for up and down variations to display any potential linear shape effects. Distributions are shown after all signal region cuts [53].

Chapter 7

Results

Thus far I have outlined all reconstruction-level inputs to our analysis including event selection, backgrounds and their estimation methods, and systematic uncertainties. Each of these components is critical to our final result. This section will focus on the methods used to extract the VBF $H \rightarrow WW^*$ cross-section measurement.

7.1 Statistical analysis

7.1.1 Likelihood functions

This analysis rests on the estimation of a parameter, μ , signal strength, which describes the statistical significance of our signal yield relative to its Standard Model prediction and, in this particular analysis, defines the signal cross-section and signal and background yields.

We build a likelihood function, $\mathcal{L}(\mu, \Theta)$, where the signal strength μ is a parameter of interest (POI) and nuisance parameters (NPs) $\Theta = \Theta_a, \Theta_b, \dots$ represent all relevant uncertainties. None of these values are known a priori, so the likelihood is built to represent the probability of particular values for the POIs and NPs. The analysis uses a maximum likeli-

CHAPTER 7. RESULTS

hood estimator to find the inputs which maximize the likelihood, i.e. minimize the negative log of the likelihood. Here I will briefly outline how a likelihood function can incorporate regions of interest. This discussion uses Ref. [61] as a guide. The Poisson distribution $\mathcal{P}(n|\lambda)$ describes the probability of n events with a true unknown yield λ :

$$\mathcal{P}(n|\lambda) = \lambda^n \frac{e^{-\lambda}}{n!}. \quad (7.1)$$

We can define a variable observable x with probability density $f(x)$, hence with n events the probability density of each is multiplied. The likelihood of λ can now be written as

$$\mathcal{L}(\lambda) = \mathcal{P}(n|\lambda) \prod_{\text{event}}^n f(x). \quad (7.2)$$

Our likelihood also must take into account multiple regions (the signal region as well as the control regions) and these likelihoods are multiplied together with their own distinct Poisson distributions,

$$\mathcal{L}(\lambda) = \prod_r^{\text{regions}} (\mathcal{P}(n_r|\lambda_r) \prod_{\text{event}}^n f(x)). \quad (7.3)$$

Our statistical fit maximizes this likelihood function and so produces a yield λ for each free parameter simultaneously. The λ values represent predicted yields where $\lambda_{r,b} = \mu\lambda_{\text{sig}} + \lambda_{\text{bkg}}$. Maximizing the overall likelihood is made simpler by applying the natural logarithm, as the products between Poisson distributions become summations.

Particle physics defines discovery with rigorous standards using hypothesis testing. In the fit, we consider both the null (background-only) hypothesis, in which $\mu = 0$, and the alternative hypothesis, in which we consider both signal and background to be present. The probability that the null hypothesis is rejected (or that the signal is discovered) is defined using a p -value. The p -value can be converted to a number of Gaussian standard deviations.

CHAPTER 7. RESULTS

In high-energy physics a 3σ significance, p -value of 1.35×10^{-3} , is considered evidence, while a 5σ result, p -value 2.87×10^{-7} , is considered a discovery.

This analysis uses the HistFitter software compiled with RooStats, RooFit, and HistFactory to perform the likelihood maximization. We measure the signal VBF Higgs cross-section in the fiducial space defined by the signal region selection with a simultaneous fit to the signal and control regions. Each region has a different distribution used in the fit to maximize that discrimination of each respective sample against all other events. This fit includes as floating parameters the signal strength of seven different processes: μ_{VBF} , μ_{TopWW} , μ_{Z+jets} , μ_{ggFSR} , μ_{ggF1} , μ_{ggF2} , and μ_{ggF3} . Each numbered ggF parameter is estimated in an orthogonal control region described in Chapter 6 while ggF SR is measured in the signal region with a targeted discriminant to differentiate VBF and ggF events. Other backgrounds, mis-identified leptons, V/γ , VH , and tth , are included as fixed parameters.

The background treatment differs depending on the particular region and sample. For $Z+jets$, a designated control region is used and the yield in the signal region is found by including a transfer factor, which maps the yield in the $Z+jets$ control region to that in the signal region. Transfer factors to extrapolate yields are derived by normalizing to MC simulation. For backgrounds estimated within the signal region (Top/ WW) the transfer factor is used only to extrapolate into the control regions where the contribution enters and thus uncertainties associated with transfer factors are reduced. We use the predicted MC values for all backgrounds included as fixed parameters such as $V\gamma$, VH , and tth . We use a data-driven method to estimate the mis-identified lepton background.

Events in the $e\mu$ and μe channels are combined in the analysis and the likelihood is defined as the product of the Poissonians over BDT output bins in the signal region multiplied by the product of Poissonians over discriminant distributions in the controls regions (ggF CRs, $Z+jets$ CR and Top/ WW CR- within the signal region). The likelihood can then be

CHAPTER 7. RESULTS

calculated

$$\begin{aligned} \mathcal{L}(\mu) &= \prod_{j=0}^{N_{\text{sig BDT bins}}} \mathcal{P}(n_j | \lambda_r) \times \prod_{k=1}^{N_{\text{CR-bins}}} P(n_k | \lambda_b) \\ &= \prod_{j=0}^{N_{\text{sig BDT bins}}} \mathcal{P}(n_j | \mu_s \lambda_{sig,j} + \sum_n \mu_b^n \lambda_{bkg}^{nj}) \times \prod_{k=1}^{N_{\text{CR-bins}}} P(n_k | \mu_s \lambda_{sig,k} + \sum_n \mu_b^n \lambda_{bkg}^{nk}). \end{aligned} \quad (7.4)$$

The signal and background strengths are denoted μ and the yields λ . Sums over all n backgrounds include $Z+\text{jets}$, top/ WW , and ggF; the minor backgrounds and data-driven $W+\text{jets}$ estimate are added to Poisson expectations as fixed parameters.

The last important additions to this likelihood are nuisance parameters. These parameters Θ come in two general types: systematics which do not affect the shape of discriminating variables ("flat systematics") and those that do ("shape systematics"). Flat systematics are constrained with a unit Gaussian and their effects are measured for $\Theta = \pm 1$. Shape systematics are constrained with a unit Gaussian as well though their effects are measured through $\nu_{\text{shape}}(\Theta) = 1 + \epsilon\Theta$, where ϵ is determined by measuring ν_{shape} at $\Theta = \pm 1$. Adding nuisance parameters Θ our final likelihood can be written

$$\mathcal{L}(\mu, \vec{\Theta}) = \prod_{j=0}^{N_{\text{sig BDT bins}}} \mathcal{P}(n_j | \mu_s \lambda_{sig,j} + \sum_n \mu_b^n \lambda_{bkg}^{nj}) \times \prod_{k=1}^{N_{\text{CR-bins}}} P(n_k | \mu_s \lambda_{sig,k} + \sum_n \mu_b^n \lambda_{bkg}^{nk}) \times \prod_{i=1}^{N_{\Theta_i}} G(\tilde{\Theta}_i | \Theta_i, 1) \quad (7.5)$$

where $G(\tilde{\Theta}_i | \Theta_i, 1) = \frac{1}{\sqrt{2\pi}} e^{\frac{(\tilde{\Theta}_i - \Theta_i)^2}{2}}$ is the unit Gaussian and $\tilde{\Theta}$ is an auxiliary measurement of Θ .

The fit is performed simultaneously for the signal region, three ggF control regions, a $Z+\text{jets}$ control region, and a shared top/ WW control defined within the signal region. Table 7.1 summarizes the regions used within the fit and their defining selections. These are

CHAPTER 7. RESULTS

discussed in more detail in Chapters 5 and 6.

Signal region	Top/ WW CR	$Z+jets$ CR	ggF SR	ggF CR1	ggF CR2	ggF CR3
$n_{jets} \geq 2$						$n_{jets} < 2$
b-veto						-
CJV			CJV/!OLV !CJV/OLV	!CJV	-	-
OLV			-	!OLV	-	-
Z -veto		$m_{\tau\tau}$	Z veto			
$m_{jj} > 200$ GeV		$m_{\ell\ell} < 80$ GeV	$m_{jj} > 200$ GeV			
$\Delta Y_{jj} > 2.1$		-	$\Delta Y_{jj} > 2.1$			
BDT _{VBF} ≥ 0	BDT _{VBF} < 0	-	-0.5 < BDT _{VBF} < 0	-	-	-

Table 7.1: Summary of all signal and control regions included in simultaneous fit

Each of the regions included in the fit uses a different discriminant to best characterize that sample’s contribution. These discriminants are almost all BDT outputs trained on various kinematic distributions to characterize certain background and signal samples, as discussed in Chapters 5 and 6. The $Z+jets$ control region is defined with m_T instead of a designated BDT after studies showed its success at mitigating uncertainty on μ_{Z+jets} . These studies are included in Appendix B. Table 7.2 summarizes the fit regions and shows their discriminant and number of bins. Table 7.3 shows MC event yields in all regions included in the statistical analysis.

Category	SR	Top/ WW CR	$Z+jets$ CR	ggF-SR	ggF-CR1	ggF-CR2	ggF-CR3
Discriminant	BDT _{VBF}	BDT _{TopWW}	m_T	BDT _{ggFVBF}	BDT _{ggF1}	BDT _{ggF2}	BDT _{ggF1}
Number of bins	25	8	20	25	8	8	8

Table 7.2: Fit categories, including SR and CRs, distributions and number of bins used in the fit.

7.1.2 Asimov results

The Asimov dataset is formed with Monte Carlo pseudo-experiments and by design returns the true value for each estimated parameter. We use the Asimov dataset to test analysis

CHAPTER 7. RESULTS

Category	SR	Top/ WW CR	Z +jets CR	ggF-CR1	ggF-CR2	ggF-CR3
VBF	149.7	14.1	16.1	100.4	8.6	192.3
Top	385.9	2878.7	331.3	34110.4	10546.4	40206.3
WW	202.0	969.0	122.6	9653.7	2608.5	86387.7
ggF	72.4	30.3	11.7	543.1	114.1	4069.1
Z +jets	313.1	476.4	1391.1	5288.5	1395.6	131014.0
Fakes	63.5	123.4	16.7	1752.9	570.0	15166.2
$V\gamma$	23.5	33.7	36.7	490.7	94.9	4652.9
VH	2.0	2.4	1.4	89.7	18.5	164.6
$t\bar{t}H$	3.8	5.9	19.8	35.5	8.5	437.6

Table 7.3: MC event yields in each signal and control region pre-fit.

strategies and deduce expected performance of the fit without using true data. We “blind” the data with by removing events in the uppermost bins of the BDT_{VBF} and use only Monte Carlo events in the signal region to eliminate any potential bias. Using this approach, we gain an understanding for the constraints on our nuisance parameters and their expected uncertainties. Using the Asimov dataset, all floating parameters are measured to be 1 and all nuisance parameters 0. Results of the fitted nuisance parameters to the Asimov dataset are made under the hypothesis that VBF Higgs boson cross-sections follow our Standard Model predictions.

Fit results for each of the signal strength parameters in our statistical fit are shown with statistical uncertainties only and statistical+systematic uncertainties. After including all uncertainties, the Asimov dataset provides an uncertainty $\pm 22\%$ on μ_{VBF} . This corresponds to a null p-value of 1.5×10^{-9} or a significance of 5.9σ , which is more than twice the expected significance in the last published ATLAS VBF Higgs $\rightarrow \ell\nu\ell\nu$ result [15]. Table 7.4 shows the stat-only and combined systematic resulting signal strengths and their expected uncertainties based on Asimov fits.

We used the Asimov dataset to optimize fit strategies and selection criteria and to de-

CHAPTER 7. RESULTS

Parameter	Estimated Uncertainty	
	Stat-only	Stat + Sys
μ_{VBF}	18.7 %	19.8%
$\mu_{\text{top}/WW}$	0.5 %	16.1%
$\mu_{\text{ggF-SR}}$	156.0 %	157.8%
μ_{ggF1}	22.0 %	27.1%
μ_{ggF2}	51.2 %	46.7%
μ_{ggF3}	22.9 %	28.1%
$\mu_{Z+\text{jets}}$	2.1 %	24.7%

Table 7.4: Asimov fit results for all floating parameters in stat-only and full systematic fits.

termine which uncertainties play large roles in this measurement. These include uncertainties related to jet flavor composition, which plays a large role in rejecting dominant top background events, and uncertainties on jet pile-up, which cause potential errors in the jet kinematics.

7.1.3 Unblinded results

After examining and testing Asimov results, we unblind the analysis, or incorporate observed data in the statistical analysis. For this thesis, this is done privately without ATLAS collaboration approval. **Does this need to be added?** Fit parameters measured by fitting simulated events with observed data are shown in Table 7.5.

The distributions in Figure 7.1 show the expected and observed events in each of the signal and control regions included in the fit. Data (black) closely matches Standard Model simulations except for some individual bins where deviations are well within the level of expected uncertainty. Bars on data points account for statistical uncertainties and shaded area shows systematics on MC events.

Figure 7.2 shows correlations between floating parameters in the fit using a stat-only

CHAPTER 7. RESULTS

Parameter	Fit value		Uncertainty	
	Stat-only	Stat+Sys	Stat-only	Stat+Sys
μ_{VBF}	1.08	0.86	19.7%	18.9%
$\mu_{\text{top}/WW}$	0.96	0.86	0.5%	13%
$\mu_{\text{ggF-SR}}$	0.55	1.00	168.0%	184%
μ_{ggF1}	1.08	1.27	22.2%	25.3%
μ_{ggF2}	0.46	0.50	50.4%	35.3%
μ_{ggF3}	1.13	1.02	23.7%	21.1%
$\mu_{Z+\text{jets}}$	0.90	92.33	2.0 %	17.2 %

Table 7.5: Fit results for all floating parameters in stat-only and stat+systematic fits.

scheme where only the seven floating signal strength parameters are included. This is to focus on the parameters which most impact the fit, although we also inspect correlations between our nuisance parameters. This is included in Ref. [53]. Correlations between fit parameters would indicate potential instability in the overall result as small changes in some estimated parameters would severely impact others. The correlation between measured background and signal parameters is small, through some parameters like μ_{ggF1} and μ_{ggF3} are anti-correlated. We have further tested the robustness of these parameters by changing their binning and discriminants and concluding that our overall Asimov fit result remains stable.

We visualize our likelihood minimization in Figure 7.3. We perform a one-dimensional scan of our parameter of interest μ_{VBF} using the inputs and distributions of of our fit. The figure shows fit results for μ_{VBF} if we use all systematics, only statistical uncertainties, and finally if we were to leave only μ_{VBF} as a floating parameter and all others constant. These results demonstrate the leading role statistical errors have in the determining our final fit value. The stat-only analysis has an expected uncertainty of 16.8/ – 16.2% while including all systematics gives an expected 19.0/ – 19.3%.

We can break down these impacts to assess which uncertainties (nuisance parameters)

CHAPTER 7. RESULTS

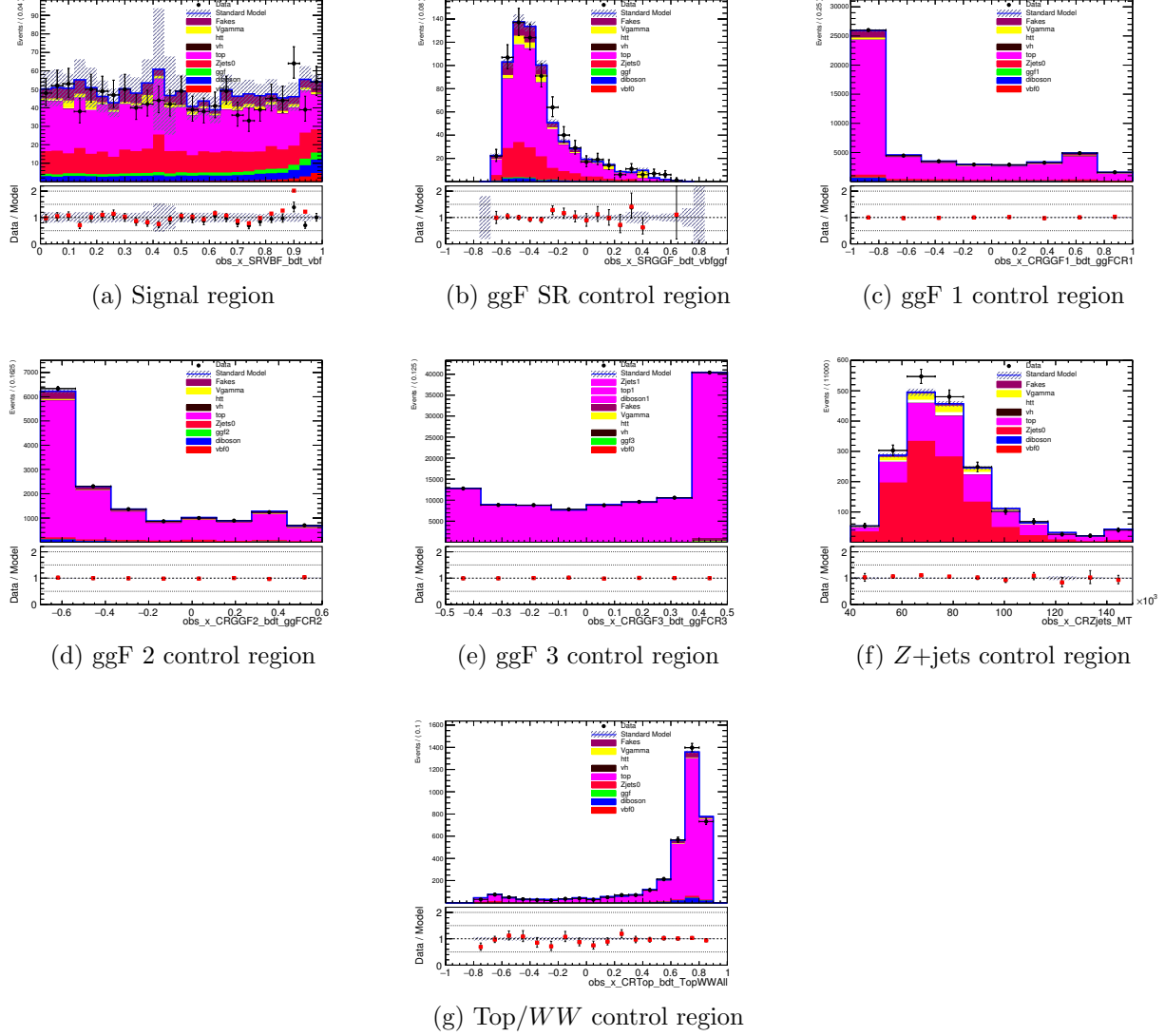


Figure 7.1: Binned distributions for each signal and control region shown after stat+sys fit where ratio between data and MC predictions is shown (black). Red points show ratio of data to all backgrounds, excluding VBF signal. Error bands show statistical (black) and systematic uncertainties (shaded).

have the greatest effects on each measured parameter. In this way, we find any that seem unduly high and test statistical means to control their effects like altering the event selection and adjusting control region definitions. Figure 7.4 shows the 30 largest impact parameters

CHAPTER 7. RESULTS



Figure 7.2: Correlations between floating parameters after a stat-only fit

for the measured signal strength. These effects are derived post-fit which means that at the maximum of the likelihood each parameter is changed by $\pm 1\sigma$ individually. The measured effects of these changes are shown in blue on the plots and ranked in order of their total combined positive and negative impact.

Most of the uncertainties in Figure 7.4 are expected to have substantial impacts on the measurement. While ggF is not the largest uncertainty, its similar signature makes it particularly difficult to differentiate from our signal. The combined WW/top estimation has a similarly large effect on the measurement. Here the backgrounds are easily differentiated from the signal but outsize the signal by far even in the signal region. Jet-related experimental systematics have the largest effects of any, with impacts from jet energy resolution, jet pile up, and jet flavor tagging. This is expected because of the large range of jet kinematic variables in our multivariate analysis. Finally, theory systematics are pivotal to the overall estimation. VBF and ggF theory uncertainties are dominant—particularly VBF shower and PDF and ggF shower parameters. Chapter 5 describes the size of these variations and

CHAPTER 7. RESULTS

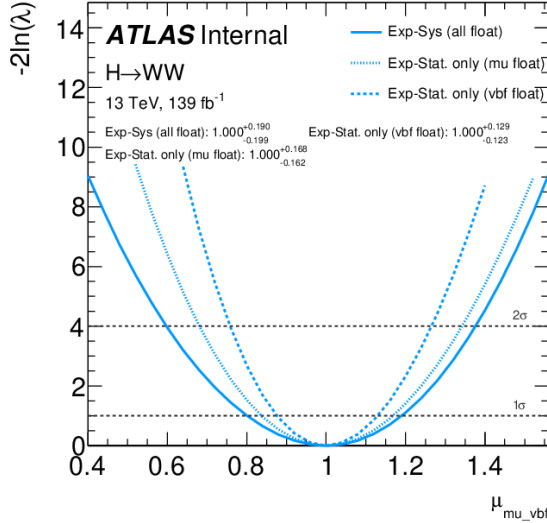


Figure 7.3: Scan of μ_{VBF} negative log-likelihood using Asimov data and using only one floating parameter, all μ values floating, and all μ and NPs floating. **Will replace with unblinded/more final plot**

explains their role in the final measurement. All theoretical systematics in this analysis are estimated using floating global variations. This intentionally overestimates the uncertainties since the final analysis will contain shape systematics that are not accounted for with this method. One of the largest overestimates comes from the top generator theory parameter. Since this background is estimated within the signal region, it will be normalized to its yield in that region and only shape systematics will have an effect. Chapter 5 shows these shape variations are small thus we can expect that the top generator uncertainty will have a smaller effect when shape systematics are included.

The fit results shown in this thesis demonstrate the most recent calculations and developments from the VBF $H \rightarrow WW$ fiducial cross-section measurement but they are not yet complete. Final fit parameters may continue to change before the analysis is published.

CHAPTER 7. RESULTS

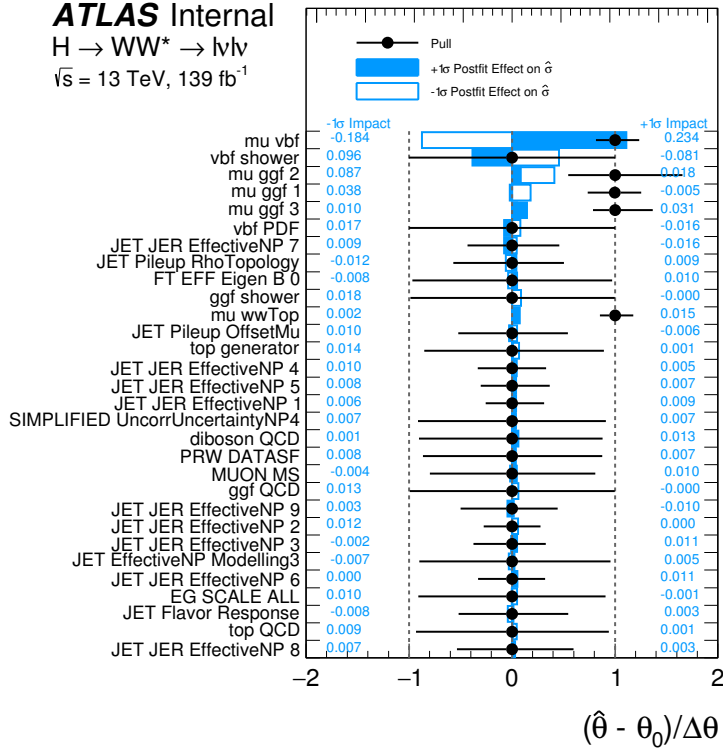


Figure 7.4: Impacts of top 30 most impactful nuisance parameters on μ_{VBF} . Asimov, will replace with unblinded plot

7.2 Fiducial and inclusive cross sections

This analysis aims to measure the total VBF $H \rightarrow WW^* \rightarrow \ell\nu\ell\nu$ cross-section in both a particular fiducial region and in a more inclusive region. The analysis group also has the goal of measuring fiducial differential $H \rightarrow WW^*$ cross-sections over a range of kinematic variables, though these measurements are beyond the scope of this thesis. In each case, the measurement must be translated from one that only represents conditions in the ATLAS detector to values that can be understood with a broad range of theoretical models. For fiducial measurements, this can be done relatively simply with a C factor. First, a fiducial

CHAPTER 7. RESULTS

region must be defined that is applicable to both reconstructed and purely theoretical, called truth level, events. This fiducial region defines the conditions under which the cross-section is measured. The fiducial cross-section is defined as

$$\sigma_{\text{VBF}H \rightarrow WW^* \rightarrow \ell\nu\ell\nu}^{\text{fid}} = \frac{N_{\text{obs}} - N_{\text{bkg}}}{C \times \mathcal{L}}, \quad (7.6)$$

where \mathcal{L} is the integrated luminosity and N (obs,bkg) is the observed and estimated background number of events, respectively. N_{bkg} is calculated through the simultaneous fit with simulated and observed events. C is a factor that accounts for detector effects that would lower the overall cross-section like detector inefficiencies and resolution effects. The fiducial phase space is defined as close to the reconstruction-level signal region as possible to minimize theoretical extrapolation. Table 7.6 lists all fiducial cuts that describe the phase space. These include requirements on lepton number, flavor, sign, and kinematics, missing energy, jet number, as well as other VBF specific requirements (OLV and CJV cuts). These cuts represent the space within which both reconstruction-level and truth-level cross-sections are measured. Yields are extracted from the statistical fit and a C -factor is defined,

$$C = \frac{N_{\text{fid}}}{N_{\text{reco}}}, \quad (7.7)$$

where N_{fid} is extacted from theoretical simulation. Powheg+Pythia8 are used to extract theoretical yields in the fiducial region. The truth-level cutflow is shown in Table 7.7. There are 371.5 ± 0.6 truth level VBF Higgs events in the final fiducial region and thus $C = 2.23 \pm 0.40$.

Using this value for C and a predicted cross-section value of 2.67 ± 0.40 fb, from the Powheg+Pythia8 fiducial cross-section truth estimate, we find a final cross-section measure-

CHAPTER 7. RESULTS

Fiducial Requirement
$ \eta(\ell) < 2.5$
$p_T^{\text{lead}} > 22\text{GeV}$
$p_T^{\text{sublead}} > 15\text{GeV}$
$N_{\text{leptons}} \geq 2$
Leptons required to be opposite flavor and sign
$\Delta R(\ell, \ell) > 0.1$
$m_{\ell\ell} > 10\text{GeV}$
$E_T^{\text{miss}} > 20\text{GeV}$
$p_T(\text{jet}) > 30\text{ GeV}$
$ \eta(\text{jet}) < 4.5$
$N_{\text{jets}} \geq 2$
$N_{b\text{-jet}} < 1$
$m_{jj} > 200\text{GeV}$
$\Delta Y_{jj} > 2.1$
$\Delta R(\ell, \text{jet}) > 0.4$
OLV=1
CJV> 20GeV

Table 7.6: Fiducial phase space definition

Full Run 2	Powheg+Pythia8 VBF
$ \eta(\ell) < 2.5$	143.72 ± 1.14
$p_T^{\text{lead}} > 22\text{GeV}$	143.72 ± 1.12
$p_T^{\text{sublead}} > 15\text{GeV}$	143.72 ± 1.12
OS Leptons	1413.74 ± 1.12
$\Delta R(\ell, \ell) > 0.1$	1345.20 ± 1.09
$m_{\ell\ell} > 10\text{GeV}$	1345.20 ± 1.09
$N_{\text{jets}} \geq 2$	744.48 ± 0.81
$m_{jj} \geq 200\text{ GeV}$	637.96 ± 0.75
$\Delta Y_{jj} > 2.1$	611.73 ± 0.73
$E_T^{\text{miss}} > 20\text{ GeV}$	544.71 ± 0.69
CJV> 20 GeV	483.37 ± 0.65
OLV bool	445.81 ± 0.62
b -veto	436.62 ± 0.62
$Z \rightarrow \tau\tau$ veto	371.49 ± 0.57

Table 7.7: Cutflow showing VBF Higgs events generated with Powheg+Pythia8 at truth-level with all fiducial selection requirements

CHAPTER 7. RESULTS

ment:

$$\sigma_{\text{fid,obs}} = 2.31 \pm 0.44 \text{fb} \quad (7.8)$$

This measured value closely matches our expected truth value, within one standard deviation, and its error of 19% is well below the previous 50% uncertainty measured on the $H \rightarrow WW^*$ VBF production cross section with 36.1 fb^{-1} [15].

The inclusive cross-section requires one additional acceptance correction factor, A , which is estimated from theoretical calculations and extrapolates the fiducial cross section to a more inclusive phase space defined solely by a requirement for $N_{\text{jets}} \geq 2$, where each jet has $p_T > 30 \text{ GeV}$. This will be calculated from

$$\sigma_{VBF}^{\text{incl}} = \frac{\sigma_{VBF}^{\text{fid}}}{A}. \quad (7.9)$$

The inclusive cross-section widens the applicable phase space of the measurement and provides another useful metric to compare data with expected Standard Model results. The A factor is found through theoretical calculations which use Powheg to estimate VBF processes at next-to-leading order in QCD and inclusive cross-section calculations from the Yellow Report [8]. The theoretical fiducial cross section is found to be $2.67 \pm \text{fb}$ using the events in Table 7.7 and the inclusive VBF $H \rightarrow WW^* \rightarrow \ell\nu\ell\nu$ cross section is calculated at $85.8 \pm 17.6 \text{ fb}$. The inclusive cross section can be calculated simply with the VBF H cross-section derived for $\sqrt{s} = 13 \text{ TeV}$ and $m_H = 125 \text{ GeV}$, and the branching fractions for $H \rightarrow WW^*$ and $WW^* \rightarrow \ell\nu\ell\nu$. The acceptance factor is therefore measured to be 0.0312 ± 0.006 . Using this factor we calculate an inclusive cross-section:

$$\sigma_{\text{incl,obs}} = 74.1 \pm 20.8 \text{fb} \quad (7.10)$$

CHAPTER 7. RESULTS

This value again matches our expected Standard Model inclusive cross section within one standard deviation.

7.3 Differential cross-section measurements

The differential cross-section measurement requires a more rigorous unfolding procedure than the total fiducial and inclusive cross-sections. Monte Carlo simulations processed in a pseudo-detector with all its expected inefficiencies and limits (reconstruction-level) are compared to Monte Carlo simulations processed solely at the particle level (truth-level). The detector effects that influence reconstruction-level events are unfolded so that they match their truth-level counterparts. This reco-truth matching is a test that the unfolding process works as expected and does not bias results. This analysis employs the iterative bayesian unfolding method [62] whose goal is to determine the probability that each bin j in a reconstruction-level distribution corresponds to bin i in a truth-level distribution. Using Bayes' theorem, this probability can be attained with knowledge of the true spectrum T and the measured or reco-level spectrum R . We begin with Bayes' theorem:

$$P(T_i|R) = \frac{P(R, T_i)P(T_i)}{\sum_t P(R, T_t)P(T_t)}, \quad (7.11)$$

where the denominator is a normalization factor, $P(R, T_i)$ represents the likelihood and $P(T_i)$ the prior. The prior here is vague and so we begin with the assumption that $P(T_i)$ is constant. Hence the most probable spectrum for T maximizes the likelihood. If we observe n reco-level events, we can assign the probability of their true distributions through

$$\hat{n}(T_i) = n(R) \prod P(T_i|R). \quad (7.12)$$

CHAPTER 7. RESULTS

We then use resultant possibilities in the Bayes formula to evaluate $P(T_i|R_j)$. These values constitute the smearing matrix M . This matrix can then be used to estimate the truth-level events in each bin of a distribution with

$$\hat{n}(T_i) = \frac{1}{\epsilon_i} \sum_{j=1}^{n_R} n(R_j) \prod P(T_i|R_j), \quad (7.13)$$

where ϵ is the inefficiency, or ratio of events that pass both truth and reco-level selection by those that pass only truth. Finally the truth can be determined by the reconstructed bin-by-bin yields through

$$n(T_i) = \sum_j M_{ij} \prod n(R_j). \quad (7.14)$$

The migration matrix directly maps reco-level distributions to truth-level. In order to calculate this matrix iteratively we first allow $P(T_i)$ to be a constant distribution, say $1/n_T$, which gives an expected number of truth events $n_0(C_i) = P_0(C_i) \prod n_R$. Next, we calculate $\hat{n}(C)$ using the efficiency equation, and finally we use χ^2 to compare $\hat{n}(C)$ and $n_0(C)$. In the next iteration, n_0 is replaced by \hat{n} and P_0 by \hat{P} , $P(\hat{C}_i) = \hat{n}(C_i)/N_{true}$, and the procedure continues until χ^2 falls below a set threshold.

While the final unfolding results fall beyond the scope of thesis, results for four kinematic variables are shown in Figure 7.5. We use reconstruction-level Monte Carlo events and their truth counterparts to calculate migration matrices for each differential observable through the iterative Bayesian unfolding process.

Further developments in unfolding are underway currently and include estimating error added by the procedure, testing for potential biases toward the truth distribution, and understanding unfolding reconstruction level uncertainties as well as nominal distributions.

CHAPTER 7. RESULTS

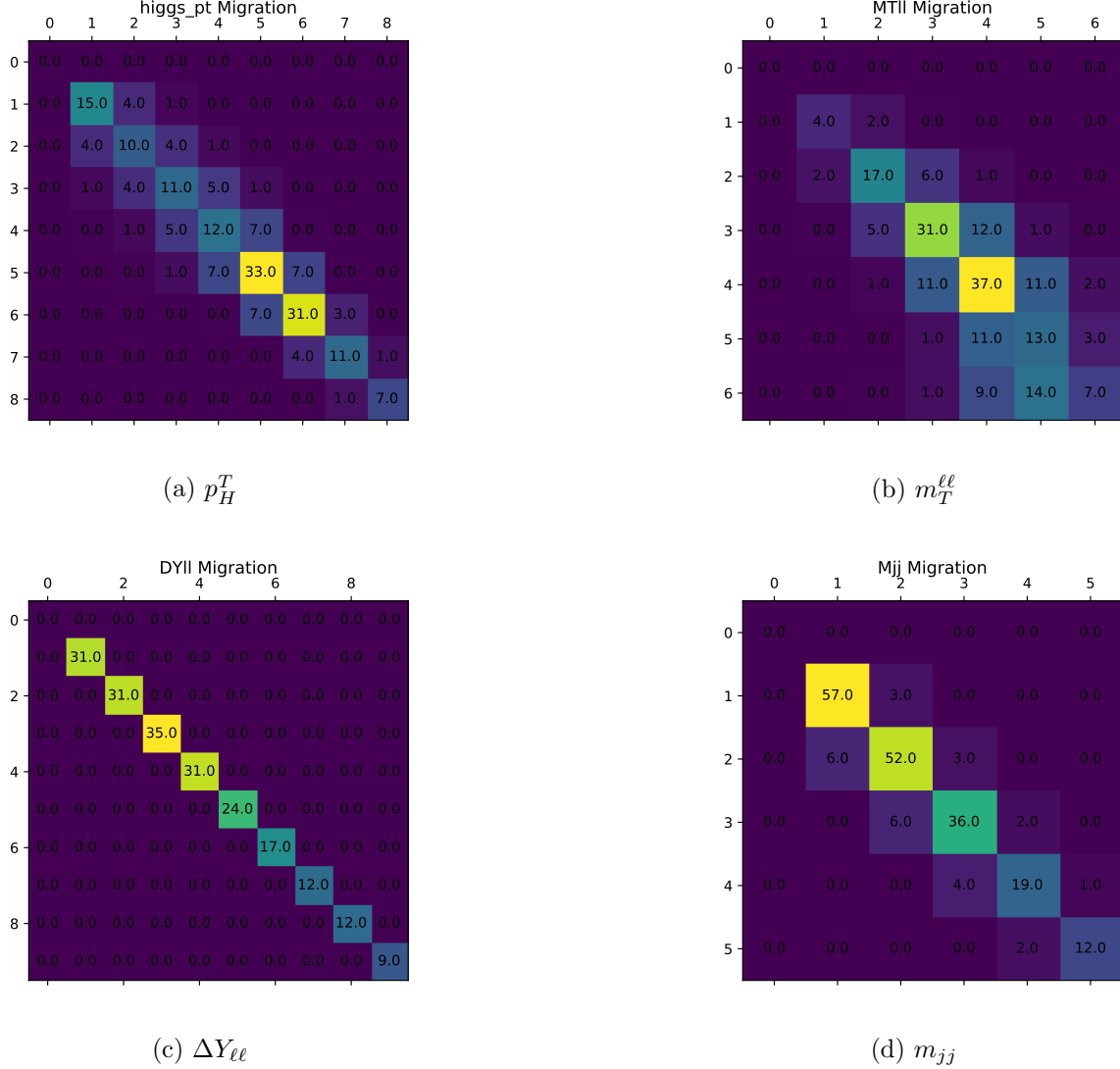


Figure 7.5: Unfolding matrices shown for p_H^T , $m_T^{\ell\ell}$, $\Delta Y_{\ell\ell}$ and m_{jj} distributions. Each bin value corresponds to normalized Bayesian probabilities and the x-axis represents reconstruction-level distributions while the y-axis shows truth distributions [53].

7.4 Future results and measurements

This thesis detailed the HWW VBF fiducial cross-section analysis as it currently stands, but there are further developments still underway. This analysis plans to measure differential

CHAPTER 7. RESULTS

cross-sections and the full unfolding procedure is almost complete. In addition, Chapter 6 discussed some theoretical uncertainties (VBF and ggF Higgs as well as top, WW, and $Z \rightarrow \tau\tau$) but these are currently estimated through global floating values. In the final analysis the uncertainties shape effects will be taken into account as well as their normalization variations.

Signal and background yields will be used within the unfolding mechanism to extract final differential distributions. The variables used in the differential analysis will also be finalized in coming months. We aim to unfold 14 variables which are listed with their planned bin edges in Table 7.8. These variables probe the kinematics of the final state particles measured through this channel and add sensitivity to the total fiducial and inclusive cross-sections. The invariant mass of the two jets that accompany the W bosons (m_{jj}) and the angular separation between them (Δy_{jj}) are particularly sensitive to the electroweak symmetry breaking mechanism. Deviations between data and theoretical predictions in the distribution of these variables may be signs of new physics that alter the HWW coupling, like new resonances at high energy scales not accessible by direct searches.

This analysis uses the full Run 2 dataset for VBF HWW cross-sections and new statistical methods. These have led to expected results which demonstrate large increases in sensitivity with respect to the most recent measurements. The VBF differential cross-sections measured for $H \rightarrow WW^*\ell\nu\ell\nu$ will be the first analyzed with the ATLAS experiment.

CHAPTER 7. RESULTS

Observable	Bin Edges
$MT^{l,l,MET}$	15,40,65,80,95,110,115,120,180
M_{ll}	0,20,25,30,35,40,45, 50, 60, 70,200
M_{jj}	200,450,700,950,1200,1500,2200,3000,5000
$Cos(\theta^*)$	0,0.125,0.25,0.375,0.5,0.625,1.0
DY_{ll}	0,0.15,0.3,0.45,0.6,0.75,0.9,1.05,1.2,1.5,4
DY_{jj}	0,2.5,3.25,3.62,4,4.35,4.75,5,5.5,6.25,7,8.5
P_t Total	150,200,250,350,500,600,900
$DPhi_{ll}$	0,0.1,0.2,0.3,0.4,0.6,0.8,1.0,1.3,1.7,2.1,2.6,3.2
P_{tll}	0,20,40,50,60,70,80,90,100,120,160,500
Higgs P_t	0,45,80,120,160,200,260,350,1000
Leading Lepton P_t	20,25,35,42,50,65,80,90,2000
Subleading Lepton P_t	20,25,35,42,50,65,80,90,2000
Leading Jet P_t	30,60,90,120,190,260,350,500
Subleading Jet P_t	30,60,90,120,190,260,350

Table 7.8: Planned observables and bin edges for differential cross-section measurements

Chapter 8

Conclusions

Bibliography

- [1] M. Tanabashi, K. Hagiwara, K. Hikasa, K. Nakamura, Y. Sumino, F. Takahashi, J. Tanaka, K. Agashe, G. Aielli, C. Amsler, M. Antonelli, D. M. Asner, H. Baer, Sw. Banerjee, R. M. Barnett, T. Basaglia, C. W. Bauer, J. J. Beatty, V. I. Belousov, J. Beringer, S. Bethke, A. Bettini, H. Bichsel, O. Biebel, K. M. Black, E. Blucher, O. Buchmuller, V. Burkert, M. A. Bychkov, R. N. Cahn, M. Carena, A. Cecucci, A. Cerri, D. Chakraborty, M.-C. Chen, R. S. Chivukula, G. Cowan, O. Dahl, G. D'Ambrosio, T. Damour, D. de Florian, A. de Gouv  a, T. DeGrand, P. de Jong, G. Dissertori, B. A. Dobrescu, M. D'Onofrio, M. Doser, M. Drees, H. K. Dreiner, D. A. Dwyer, P. Eerola, S. Eidelman, J. Ellis, J. Erler, V. V. Ezhela, W. Fettscher, B. D. Fields, R. Firestone, B. Foster, A. Freitas, H. Gallagher, L. Garren, H.-J. Gerber, G. Gerbier, T. Gershon, Y. Gershtein, T. Gherghetta, A. A. Godizov, M. Goodman, C. Grab, A. V. Gritsan, C. Grojean, D. E. Groom, M. Grunewald, A. Gurtu, T. Gutsche, H. E. Haber, C. Hanhart, S. Hashimoto, Y. Hayato, K. G. Hayes, A. Hebecker, S. Heinemeyer, B. Heltsley, J. J. Hern  ndez-Rey, J. Hisano, A. H  cker, J. Holder, A. Holtkamp, T. Hyodo, K. D. Irwin, K. F. Johnson, M. Kado, M. Karliner, U. F. Katz, S. R. Klein, E. Klemp, R. V. Kowalewski, F. Krauss, M. Kreps, B. Krusche, Yu. V. Kuyanov, Y. Kwon, O. Lahav, J. Laiho, J. Lesgourgues, A. Liddle, Z. Ligeti, C.-J. Lin, C. Lippmann, T. M. Liss, L. Littenberg, K. S. Lugovsky, S. B. Lugovsky, A. Lusiani, Y. Makida,

BIBLIOGRAPHY

F. Maltoni, T. Mannel, A. V. Manohar, W. J. Marciano, A. D. Martin, A. Masi, J. Matthews, U.-G. Meißner, D. Milstead, R. E. Mitchell, K. Mönig, P. Molaro, F. Moortgat, M. Moskovic, H. Murayama, M. Narain, P. Nason, S. Navas, M. Neubert, P. Nevski, Y. Nir, K. A. Olive, S. Pagan Griso, J. Parsons, C. Patrignani, J. A. Peacock, M. Pennington, S. T. Petcov, V. A. Petrov, E. Pianori, A. Piepke, A. Pomarol, A. Quadt, J. Rademacker, G. Raffelt, B. N. Ratcliff, P. Richardson, A. Ringwald, S. Roesler, S. Rolli, A. Romanouk, L. J. Rosenberg, J. L. Rosner, G. Rybka, R. A. Ryutin, C. T. Sachrajda, Y. Sakai, G. P. Salam, S. Sarkar, F. Sauli, O. Schneider, K. Scholberg, A. J. Schwartz, D. Scott, V. Sharma, S. R. Sharpe, T. Shutt, M. Silari, T. Sjöstrand, P. Skands, T. Skwarnicki, J. G. Smith, G. F. Smoot, S. Spanier, H. Spieler, C. Spiering, A. Stahl, S. L. Stone, T. Sumiyoshi, M. J. Syphers, K. Terashi, J. Terning, U. Thoma, R. S. Thorne, L. Tiator, M. Titov, N. P. Tkachenko, N. A. Tornqvist, D. R. Tovey, G. Valencia, R. Van de Water, N. Varelas, G. Venanzoni, L. Verde, M. G. Vinter, P. Vogel, A. Vogt, S. P. Wakely, W. Walkowiak, C. W. Walter, D. Wands, D. R. Ward, M. O. Wascko, G. Weiglein, D. H. Weinberg, E. J. Weinberg, M. White, L. R. Wiencke, S. Willocq, C. G. Wohl, J. Womersley, C. L. Woody, R. L. Workman, W.-M. Yao, G. P. Zeller, O. V. Zenin, R.-Y. Zhu, S.-L. Zhu, F. Zimmermann, P. A. Zyla, J. Anderson, L. Fuller, V. S. Lugovsky, and P. Schaffner. Review of particle physics. *Phys. Rev. D*, 98:030001, Aug 2018.

- [2] F. Halzen and A. Martin. *Quarks and Leptons: An Introductory Course in Modern Particle Physics*. 1984.
- [3] John Ellis. Higgs Physics. (KCL-PH-TH-2013-49. KCL-PH-TH-2013-49. LCTS-2013-36. CERN-PH-TH-2013-315):117–168. 52 p, Dec 2013. 52 pages, 45 figures, Lectures

BIBLIOGRAPHY

presented at the ESHEP 2013 School of High-Energy Physics, to appear as part of the proceedings in a CERN Yellow Report.

- [4] Jonathan M. Butterworth, Guenther Dissertori, and Gavin P. Salam. Hard Processes in Proton-Proton Collisions at the Large Hadron Collider. *Ann. Rev. Nucl. Part. Sci.*, 62:387–405, 2012.
- [5] John M. Campbell, J. W. Huston, and W. J. Stirling. Hard Interactions of Quarks and Gluons: A Primer for LHC Physics. *Rept. Prog. Phys.*, 70:89, 2007.
- [6] W.J. Stirling. Private communication. 2018.
- [7] Abdelhak Djouadi. The Anatomy of electro-weak symmetry breaking. I: The Higgs boson in the standard model. *Phys. Rept.*, 457:1–216, 2008.
- [8] D. de Florian, C. Grojean, F. Maltoni, C. Mariotti, A. Nikitenko, M. Pieri, P. Savard, M. Schumacher, R. Tanaka, R. Aggleton, M. Ahmad, B. Allanach, C. Anastasiou, W. Astill, S. Badger, M. Badziak, J. Baglio, E. Bagnaschi, A. Ballestrero, A. Banfi, D. Barducci, M. Beckingham, C. Becot, G. Bélanger, J. Bellm, N. Belyaev, F.U. Bernlochner, C. Beskidt, A. Biekötter, F. Bishara, W. Bizon, N.E. Bomark, M. Bonvini, S. Borowka, V. Bortolotto, S. Boselli, F.J. Botella, R. Boughezal, G.C. Branco, J. Brehmer, L. Brenner, S. Bressler, I. Brivio, A. Broggio, H. Brun, G. Buchalla, C.D. Burgard, A. Calandri, L. Caminada, R. Caminal Armadans, F. Campanario, J. Campbell, F. Caola, C.M. Carloni Calame, S. Carrazza, A. Carvalho, M. Casolino, O. Cata, A. Celis, F. Cerutti, N. Chanon, M. Chen, X. Chen, B. Chokoufé Nejad, N. Christensen, M. Ciuchini, R. Contino, T. Corbett, Raul Costa, D. Curtin, M. Dall’Osso, A. David, S. Dawson, J. de Blas, W. de Boer, P. de Castro Manzano, C. Degrande, R.L. Delgado, F. Demartin, A. Denner, B. Di Micco, R. Di Nardo, S. Dittmaier, A. Dobado, T. Dorigo,

BIBLIOGRAPHY

F.A. Dreyer, M. Dührssen, C. Duhr, F. Dulat, K. Ecker, K. Ellis, U. Ellwanger, C. Englert, D. Espriu, A. Falkowski, L. Fayard, R. Feger, G. Ferrera, A. Ferroglio, N. Fidanza, T. Figy, M. Flechl, D. Fontes, S. Forte, P. Francavilla, E. Franco, R. Frederix, A. Freitas, F.F. Freitas, F. Frensch, S. Frixione, B. Fuks, E. Furlan, S. Gadatsch, J. Gao, Y. Gao, M.V. Garzelli, T. Gehrmann, R. Gerosa, M. Ghezzi, D. Ghosh, S. Gieseke, D. Gillberg, G.F. Giudice, E.W.N. Glover, F. Goertz, D. Gonçalves, J. Gonzalez-Fraile, M. Gorbahn, S. Gori, C.A. Gottardo, M. Gouzevitch, P. Govoni, D. Gray, M. Grazzini, N. Greiner, A. Greljo, J. Grigo, A.V. Gritsan, R. Gröber, S. Guindon, H.E. Haber, C. Han, T. Han, R. Harlander, M.A. Harrendorf, H.B. Hartanto, C. Hays, S. Heinemeyer, G. Heinrich, M. Herrero, F. Herzog, B. Hespel, V. Hirschi, S. Hoeche, S. Honeywell, S.J. Huber, C. Hugonie, J. Huston, A. Ilnicka, G. Isidori, B. Jäger, M. Jaquier, S.P. Jones, A. Juste, S. Kallweit, A. Kaluza, A. Kardos, A. Karlberg, Z. Kassabov, N. Kauer, D.I. Kazakov, M. Kerner, W. Kilian, F. Kling, K. Köneke, R. Kogler, R. Konoplich, S. Kortner, S. Kraml, C. Krause, F. Krauss, M. Krawczyk, A. Kulesza, S. Kuttimalai, R. Lane, A. Lazopoulos, G. Lee, P. Lenzi, I.M. Lewis, Y. Li, S. Liebler, J. Lindert, X. Liu, Z. Liu, F.J. Llanes-Estrada, H.E. Logan, D. Lopez-Val, I. Low, G. Luisoni, P. Maierhöfer, E. Maina, B. Mansoulié, H. Mantler, M. Mantoani, A.C. Marini, V.I. Martinez Outschoorn, S. Marzani, D. Marzocca, A. Massironi, K. Mawatari, J. Mazzitelli, A. McCarn, B. Mellado, K. Melnikov, S.B. Menari, L. Merlo, C. Meyer, P. Milenovic, K. Mimasu, S. Mishima, B. Mistlberger, S.-O. Moch, A. Mohammadi, P.F. Monni, G. Montagna, M. Moreno Llácer, N. Moretti, S. Moretti, L. Motyka, A. Mück, M. Mühlleitner, S. Munir, P. Musella, P. Nadolsky, D. Napoletano, M. Nebot, C. Neu, M. Neubert, R. Nevzorov, O. Nicrosini, J. Nielsen, K. Nikolopoulos, J.M. No, C. O'Brien, T. Ohl, C. Oleari, T. Orimoto, D. Pagani, C.E. Pandini, A. Papaefstathiou, A.S. Papanastasiou, G. Passarino, B.D. Pecjak, M. Pelliccioni, G. Perez, L. Per-

BIBLIOGRAPHY

rozzi, F. Petriello, G. Petrucciani, E. Pianori, F. Piccinini, M. Pierini, A. Pilkington, S. Plätzer, T. Plehn, R. Podskubka, C.T. Potter, S. Pozzorini, K. Prokofiev, A. Pukhov, I. Puljak, M. Queitsch-Maitland, J. Quevillon, D. Rathlev, M. Rauch, E. Re, M.N. Rebelo, D. Rebuzzi, L. Reina, C. Reuschle, J. Reuter, M. Riembau, F. Riva, A. Rizzi, T. Robens, R. Röntsch, J. Rojo, J.C. Romão, N. Rompotis, J. Roskes, R. Roth, G.P. Salam, R. Salerno, M.O.P. Sampaio, R. Santos, V. Sanz, J.J. Sanz-Cillero, H. Sargsyan, U. Sarica, P. Schichtel, J. Schlenk, T. Schmidt, C. Schmitt, M. Schönher, U. Schubert, M. Schulze, S. Sekula, M. Sekulla, E. Shabalina, H.S. Shao, J. Shelton, C.H. Shepherd-Themistocleous, S.Y. Shim, F. Siegert, A. Signer, J.P. Silva, L. Silvestrini, M. Sjodahl, P. Slavich, M. Slawinska, L. Soffi, M. Spannowsky, C. Speckner, D.M. Sperka, M. Spira, O. Stål, F. Staub, T. Stebel, T. Stefaniak, M. Steinhauser, I.W. Stewart, M.J. Strassler, J. Streicher, D.M. Strom, S. Su, X. Sun, F.J. Tackmann, K. Tackmann, A.M. Teixeira, R. Teixeira de Lima, V. Theeuwes, R. Thorne, D. Tommasini, P. Torrielli, M. Tosi, F. Tramontano, Z. Trócsányi, M. Trott, I. Tsinikos, M. Ubiali, P. Vanlaer, W. Verkerke, A. Vicini, L. Viliani, E. Vryonidou, D. Wackerlo, C.E.M. Wagner, J. Wang, S. Wayand, G. Weiglein, C. Weiss, M. Wiesemann, C. Williams, J. Winter, D. Winterbottom, R. Wolf, M. Xiao, L.L. Yang, R. Yohay, S.P.Y. Yuen, G. Zanderighi, M. Zaro, D. Zeppenfeld, R. Ziegler, T. Zirke, and J. Zupan. *Handbook of LHC Higgs Cross Sections: 4. Deciphering the Nature of the Higgs Sector*. CERN Yellow Reports: Monographs. Oct 2016. 869 pages, 295 figures, 248 tables and 1645 citations. Working Group web page: <https://twiki.cern.ch/twiki/bin/view/LHCPhysics/LHCHXSWG>.

- [9] Jon Butterworth et al. PDF4LHC recommendations for LHC Run II. *J. Phys.*, G43:023001, 2016.
- [10] Georges Aad et al. Observation of a new particle in the search for the Standard Model

BIBLIOGRAPHY

- Higgs boson with the ATLAS detector at the LHC. *Phys. Lett.*, B716:1–29, 2012.
- [11] Tom W. B. Kibble. The Standard Model of Particle Physics. 2014.
- [12] N.R. Council, D.E.P. Sciences, B.P. Astronomy, and C.E.P. Physics. *Elementary-Particle Physics: Revealing the Secrets of Energy and Matter*. Physics in a New Era: A Series. National Academies Press, 1998.
- [13] Georges Aad et al. Combined measurements of Higgs boson production and decay using up to 80 fb^{-1} of proton-proton collision data at $\sqrt{s} = 13 \text{ TeV}$ collected with the ATLAS experiment. *Phys. Rev.*, D101(1):012002, 2020.
- [14] Georges Aad et al. Measurement of fiducial differential cross sections of gluon-fusion production of Higgs bosons decaying to $WW^* \rightarrow e\nu\mu\nu$ with the ATLAS detector at $\sqrt{s} = 8 \text{ TeV}$. *JHEP*, 08:104, 2016.
- [15] M. Aaboud, G. Aad, B. Abbott, O. Abdinov, B. Abeloos, D.K. Abhayasinghe, S.H. Abidi, O.S. AbouZeid, N.L. Abraham, H. Abramowicz, and et al. Measurements of gluon-gluon fusion and vector-boson fusion higgs boson production cross-sections in the $h \rightarrow ww^* \rightarrow e\nu\mu\nu$ decay channel in pp collisions at $\sqrt(s)=13\text{tev}$ with the atlas detector. *Physics Letters B*, 789:508–529, Feb 2019.
- [16] Rende Steerenberg. Lhc report: Protons: mission accomplished, 2018.
- [17] M. Aaboud, G. Aad, B. Abbott, O. Abdinov, B. Abeloos, D.K. Abhayasinghe, S.H. Abidi, O.S. AbouZeid, N.L. Abraham, H. Abramowicz, and et al. Observation of $h \rightarrow bb^-$ decays and vh production with the atlas detector. *Physics Letters B*, 786:59–86, Nov 2018.

BIBLIOGRAPHY

- [18] M. Aaboud, G. Aad, B. Abbott, O. Abdinov, B. Abelos, S. H. Abidi, O. S. AbouZeid, N. L. Abraham, H. Abramowicz, and et al. Measurement of the higgs boson coupling properties in the $h \rightarrow zz^* \rightarrow 4\ell$ decay channel at $\sqrt{s} = 13$ tev with the atlas detector. *Journal of High Energy Physics*, 2018(3), Mar 2018.
- [19] M. Aaboud, G. Aad, B. Abbott, O. Abdinov, B. Abelos, S. H. Abidi, O. S. AbouZeid, N. L. Abraham, H. Abramowicz, H. Abreu, and et al. Measurements of higgs boson properties in the diphoton decay channel with 36 fb^{-1} of pp collision data at $\sqrt{s} = 13$ tev with the atlas detector. *Physical Review D*, 98(5), Sep 2018.
- [20] M. Aaboud, G. Aad, B. Abbott, O. Abdinov, B. Abelos, D. K. Abhayasinghe, S. H. Abidi, O. S. AbouZeid, N. L. Abraham, H. Abramowicz, and et al. Cross-section measurements of the higgs boson decaying into a pair of τ -leptons in proton-proton collisions at $\sqrt{s}=13$ tev with the atlas detector. *Physical Review D*, 99(7), Apr 2019.
- [21] Search for squarks and gluinos in final states with jets and missing transverse momentum using 139 fb^{-1} of $\sqrt{s} = 13$ TeV pp collision data with the ATLAS detector. Technical Report ATLAS-CONF-2019-040, CERN, Geneva, Aug 2019.
- [22] CERN. A new schedule for the lhc and its successor, 2019.
- [23] M. Benedikt, P. Collier, V. Mertens, J. Poole, and K. Schindl. LHC Design Report. 3. The LHC injector chain. 2004.
- [24] Radiofrequency cavities. Sep 2012.
- [25] Lyndon Evans. The large hadron collider. *New Journal of Physics*, 9(9):335–335, sep 2007.

BIBLIOGRAPHY

- [26] G Aad et al. The ATLAS Experiment at the CERN Large Hadron Collider. *JINST*, 3:S08003. 437 p, 2008. Also published by CERN Geneva in 2010.
- [27] Apollinari G., Béjar Alonso I., Brüning O., Fessia P., Lamont M., Rossi L., and Tavian L. *High-Luminosity Large Hadron Collider (HL-LHC): Technical Design Report V. 0.1*. CERN Yellow Reports: Monographs. CERN, Geneva, 2017.
- [28] Early Inner Detector Tracking Performance in the 2015 data at $\sqrt{s} = 13$ TeV. Technical Report ATL-PHYS-PUB-2015-051, CERN, Geneva, Dec 2015.
- [29] Performance of the ATLAS Silicon Pattern Recognition Algorithm in Data and Simulation at $\sqrt{s} = 7$ TeV. Technical Report ATLAS-CONF-2010-072, CERN, Geneva, Jul 2010.
- [30] ATLAS Collaboration. 14(12):P12006–P12006, dec 2019.
- [31] G. Aad, B. Abbott, J. Abdallah, O. Abdinov, B. Abeloos, R. Aben, M. Abolins, O. S. AbouZeid, N. L. Abraham, and et al. Muon reconstruction performance of the atlas detector in proton–proton collision data at $\sqrt{s}=13$ tev. *The European Physical Journal C*, 76(5), May 2016.
- [32] Georges Aad et al. Measurement of the muon reconstruction performance of the ATLAS detector using 2011 and 2012 LHC proton–proton collision data. Measurement of the muon reconstruction performance of the ATLAS detector using 2011 and 2012 LHC proton-proton collision data. *Eur. Phys. J. C*, 74(CERN-PH-EP-2014-151. CERN-PH-EP-2014-151):3130. 34 p, Jul 2014. Comments: 21 pages plus author list + cover pages (34 pages total), 21 figures, 2 tables, submitted to EPJC, All figures including auxiliary figures are available at <http://atlas.web.cern.ch/Atlas/GROUPS/PHYSICS/PAPERS/PERF-2014-05/>.

BIBLIOGRAPHY

- [33] Johannes Josef Junggeburth. Muon identification and reconstruction efficiencies in full Run-2 dataset. Technical Report ATL-COM-PHYS-2019-1001, CERN, Geneva, Aug 2019.
- [34] G. Aad, B. Abbott, J. Abdallah, A. A. Abdelalim, A. Abdesselam, O. Abdinov, B. Abi, M. Abolins, H. Abramowicz, and et al. Jet energy measurement with the atlas detector in proton-proton collisions at $\sqrt{s} = 7$ tev. *The European Physical Journal C*, 73(3), Mar 2013.
- [35] Miha Zgubič, Johannes Josef Junggeburth, and K. Technical report.
- [36] Souvik Das. A simple alternative to the crystal ball function, 2016.
- [37] Jet global sequential corrections with the ATLAS detector in proton-proton collisions at $\sqrt{s} = 8$ TeV. Technical Report ATLAS-CONF-2015-002, CERN, Geneva, Mar 2015.
- [38] Morad Aaboud et al. Jet reconstruction and performance using particle flow with the ATLAS Detector. *Eur. Phys. J.*, C77(7):466, 2017.
- [39] JET ETmiss group. Public plots, 2019.
- [40] Matteo Cacciari, Gavin P. Salam, and Gregory Soyez. The anti- k_t jet clustering algorithm. *JHEP*, 04:063, 2008.
- [41] Morad Aaboud et al. Determination of jet calibration and energy resolution in proton-proton collisions at $\sqrt{s} = 8$ TeV using the ATLAS detector. 2019.
- [42] Object-based missing transverse momentum significance in the ATLAS detector. Technical Report ATLAS-CONF-2018-038, CERN, Geneva, Jul 2018.

BIBLIOGRAPHY

- [43] Morad Aaboud et al. Performance of missing transverse momentum reconstruction with the ATLAS detector using proton-proton collisions at $\sqrt{s} = 13$ TeV. *Eur. Phys. J.*, C78(11):903, 2018.
- [44] Luminosity public results. Public plots, 2019.
- [45] S. Agostinelli et al. GEANT4: A Simulation toolkit. *Nucl. Instrum. Meth. A*, 506:250, 2003.
- [46] Simone Alioli, Paolo Nason, Carlo Oleari, and Emanuele Re. A general framework for implementing NLO calculations in shower Monte Carlo programs: the POWHEG BOX. *JHEP*, 06:043, 2010.
- [47] M. Ciccolini, Ansgar Denner, and S. Dittmaier. Strong and electroweak corrections to the production of Higgs+2jets via weak interactions at the LHC. *Phys. Rev. Lett.*, 99:161803, 2007.
- [48] K. Arnold et al. VBFNLO: A parton level Monte Carlo for processes with electroweak bosons. *Comput. Phys. Commun.*, 180:1661–1670, 2009.
- [49] Paolo Bolzoni, Fabio Maltoni, Sven-Olaf Moch, and Marco Zaro. Higgs production via vector-boson fusion at NNLO in QCD. *Phys. Rev. Lett.*, 105:011801, 2010.
- [50] Torbjorn Sjostrand, Stephen Mrenna, and Peter Z. Skands. PYTHIA 6.4 Physics and Manual. *JHEP*, 05:026, 2006.
- [51] Torbjorn Sjostrand, Stephen Mrenna, and Peter Z. Skands. A Brief Introduction to PYTHIA 8.1. *Comput. Phys. Commun.*, 178:852–867, 2008.

BIBLIOGRAPHY

- [52] A. Hoecker, P. Speckmayer, J. Stelzer, J. Therhaag, E. von Toerne, H. Voss, M. Backes, T. Carli, O. Cohen, A. Christov, D. Dannheim, K. Danielowski, S. Henrot-Versille, M. Jachowski, K. Kraszewski, A. Krasznahorkay Jr., M. Kruk, Y. Mahalalel, R. Ospanov, X. Prudent, A. Robert, D. Schouten, F. Tegenfeldt, A. Voigt, K. Voss, M. Wolter, and A. Zemla. Tmva - toolkit for multivariate data analysis, 2007.
- [53] L. Bergste C. Blocker J. Chen C. Piccola G. Iakovidis C. Kitsaki G. Rosin G. Sciolla S. Stucci S. Addepalli, G. Barone and A. Tricoli. Measurements of the $h \rightarrow ww^* \rightarrow \ell\nu\ell\nu$ cross section in vector boson fusion at $\sqrt{s} = 13$ tev with the atlas detector, In preparation.
- [54] Travis Martin and W Martin. Analyzing new neutral gauge bosons at the lhc using third generation fermions. 05 2020.
- [55] Top quark mass measurement in the $e\mu$ channel using the mT2 variable at ATLAS. Technical Report ATLAS-CONF-2012-082, CERN, Geneva, Jul 2012.
- [56] W. Buttinger. Background estimation with the abcd method, 2018.
- [57] Fabio Cardillo, Otilia Anamaria Ducu, Julien Maurer, Claudia Merlassino, Joseph Reichert, Erich Varnes, Pepijn Johannes Bakker, and Marcus Morgenstern. Tools for estimating fake/non-prompt lepton backgrounds in ATLAS. Technical Report ATL-COM-PHYS-2019-1071, CERN, Geneva, Sep 1999.
- [58] Luminosity determination in pp collisions at $\sqrt{s} = 13$ TeV using the ATLAS detector at the LHC. Technical Report ATLAS-CONF-2019-021, CERN, Geneva, Jun 2019.
- [59] Wg1 scheme: meeting discussions.

BIBLIOGRAPHY

- [60] Stefano Frixione, Eric Laenen, Patrick Motylinski, Chris White, and Bryan R Webber. Single-top hadroproduction in association with awboson. *Journal of High Energy Physics*, 2008(07):029–029, Jul 2008.
- [61] Kyle Cranmer. Practical statistics for the lhc, 2015.
- [62] G. D’Agostini. A Multidimensional unfolding method based on Bayes’ theorem. *Nucl. Instrum. Meth. A*, 362:487–498, 1995.
- [63] ATLAS Collaboration. Technical Design Report for the ATLAS Inner Tracker Strip Detector. Technical Report CERN-LHCC-2017-005. ATLAS-TDR-025, CERN, Geneva, Apr 2017.

Appendix A

Inner Tracker

The Inner Tracker (ITk) is an all-silicon detector that will completely replace the current Inner Detector. While the current ID has been extremely successful during Runs 1 and 2 (and will certainly continue to be in Run 3), it does not have the capacity to withstand the radiation and pile-up conditions of the HL-LHC. The ITk is designed to operate for 10 years at an instantaneous luminosity of $7.5 \times 10^{-34} \text{ cm}^{-2}\text{s}^{-1}$ with 25 ns between proton bunches. This will result in $1,000 \text{ fb}^{-1}$ and average pile-up up to 200 [63]. The current solenoid magnet will remain in the detector providing a 2 T magnetic field. The ITk will consist of an innermost section with silicon pixels and an outermost section of silicon strips. The pixel detector will contain four barrel layers and six forward region disks, while the strip detector will contain five barrel layers and seven disks. The rapidity range matches the coverage of the Muon Spectrometer with $|\eta| < 2.7$. This layout is shown in [A.1](#).

Building ITk Strip barrel staves

At Brookhaven National Laboratory (BNL), I made key contributions to the ITk Strip barrel stave assembly effort. The goal of stave assembly is to glue silicon modules to carbon

APPENDIX A. INNER TRACKER

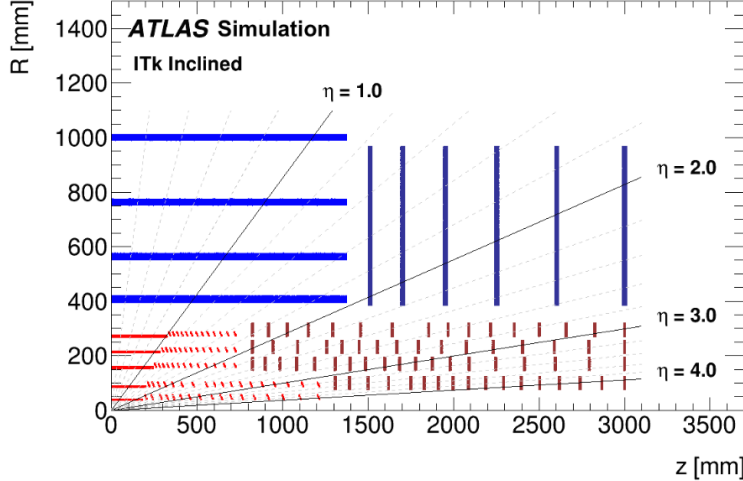


Figure A.1: ITk layout as defined in ITk Technical Design Report [63]

fiber stave cores within a $25\text{ }\mu\text{m}$ tolerance. Brookhaven is responsible for assembly of 200 ITk staves and their accurate assembly is necessary for the ITk to reduce uncertainty on track positions as well as to ensure a symmetric detector. I was tasked with co-creating a stave assembly software system through LABView to automatically calibrate required module positions, apply a layer of adhesive gel, and guide a user in accurately placing a module into its specified location. This project was highly collaborative and evolved further after I left the laboratory, but the overall process remains unchanged.

The basic design of the Inner Tracker for both barrel and endcap components is the same—a carbon fiber core (containing titanium cooling pipes) is covered on each side with co-cured kapton service tapes. The carbon fiber core is designed to reduce material inside the detector and the similar design in the barrel and endcap adds to simplicity. Silicon detector modules are glued to the stave cores. Similar silicon strip detectors have been used previously in both ATLAS and CMS, but have never covered so much fiducial area. The modules consist of one silicon sensor and one or two low-mass integrated circuit chips. Module design has optimized producibility and low cost while maintaining readout goals.

APPENDIX A. INNER TRACKER

Overall module design is the same in barrel and endcap regions, while strip lengths and geometries vary. Components of a short-strip barrel module are shown in Figure A.2. Each barrel stave core needs to be “loaded” with 14 modules, as shown in the assembled electrical prototype in Figure A.3.

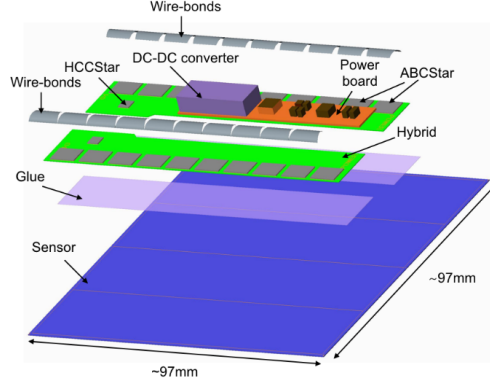


Figure A.2: Short-strip barrel module components [63]

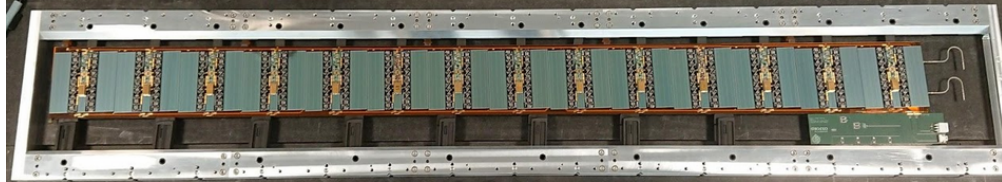


Figure A.3: Electrical stave prototype at Brookhaven National Laboratory (G. van Nieuwenhuizen)

Brookhaven National Laboratory is one of two sites responsible for assembling barrel staves. Assembly procedures are tested with the production of numerous prototypes including a thermo-mechanical double-sided stave and a fully operational electrical stave. The thermo-mechanical prototype was later used for various thermal tests, including infrared imaging. The electrical stave was used for testing the full electrical read-out. Stave assembly is composed of three main parts: system calibration, module placement, and survey of results.

APPENDIX A. INNER TRACKER

Staves at BNL are assembled on a granite table housing an Aerotech XYZ Stage accurate to the micron level. The stage is equipped with a 10-megapixel camera that gives real-time feedback to a nearby computer and a glue dispenser. The stave assembly software system is implemented by a user who interacts with a LabView graphical user interface and monitors progress. The stave is fixed to optical rails drilled into the granite table. Calibrations are completed to accurately place modules in their correct positions. These include camera calibrations to test the optimal working point, focus, and pixel-to-micron conversion. Next, the position of the stave with relation to the XYZ stage is calibrated. Transforming coordinates of the XYZ stage to that of the stave requires locating a fixed point on the stave core as well as the angle of the stave relative to the XYZ stage. Pattern matching algorithms find the exact locations of particular features on the stave core and allow calculation of required positions for all modules based on specifications. Once specified, module positions are calculated, calibrations are completed and it is time to apply glue and attach modules.

Next, an epoxy (SE4445) is loaded into the glue dispenser on the XYZ-stage which is connected to a vacuum controlled by the LABView software system. The epoxy is automatically dispensed in lines to cover $\approx 60\%$ of area under the module. Then the module is lifted with a custom-made “pick-up” tool which uses vacuum applied to module corners to hold the module in place and move it to the needed position along the optical rails. Using real-time feedback from the software system and its pattern matching algorithm, the user is directed on how to finetune module position using knobs on the “pick-up” tool. Markings etched in the silicon sensor at each corner are used to position the module accurately. The output of the module alignment GUI is shown in Figure A.4. When the module is within specifications it is lowered into position above the epoxy and held in place for 24 hours until the glue has completely dried.

APPENDIX A. INNER TRACKER



Figure A.4: GUI interface showing etched marking on module corner located in real-time to guide user on how to adjust module position (H. Herde)

After the glue has set, a final survey of module positions is recorded using pattern matching to find positions of etched markings on each module corner. These results are saved into an ITk database and checked for any biases. After module placement on the stave is complete, the loaded stave is moved to another station in the lab for wirebonding so that all data from the modules can be read-out to stave-wide electronics. The module assembly system has been successful at placing modules accurately for all prototypes, achieving specification requirements for almost all modules. Results of the first prototype stave’s module placement are shown in Figure A.5. While a few module corners are slightly out of the ideal range, the majority are well within specifications. Throughout prototype assembly issues and inefficiencies were found and corrected. New hardware, like an improved glue system and temperature monitoring, were also added. The methods described continue to be in use now and will be utilized for the production of 200 ITk staves at BNL starting in 2021.

APPENDIX A. INNER TRACKER

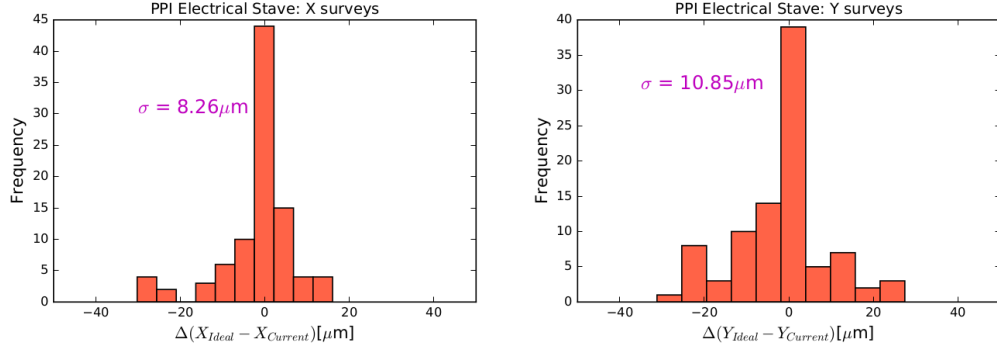


Figure A.5: Histograms show difference between ideal and final position of each module corner. Left shows difference from specification in X and right in Y (P. Bhattacharai)

IR Testing of ITk Strip barrel staves

The first full US stave prototype was the thermo-mechanical stave built in the summer of 2017. Building this stave was the first test of stave assembly procedures and the results proved that the module placement algorithm we developed worked. This stave was also used to test the thermal and mechanical properties of a fully loaded barrel stave. Multiple studies were conducted, including thermal measurements using thermistors and IR imaging, thermal cycling and thermal shock tests, mechanical studies, and bending tests. I will give a short summary of IR imaging tests, as these were another focus of my time at BNL.

The thermo-mechanical (TM) stave consists of 13 modules mounted on each side. The modules used are thermo-mechanical, which means that instead of the usual readout chips their hybrids employed copper resistors to mimic the power dissipation and location of the chips. The powerboard can vary the TM hybrid power dissipation of each module individually. Three thermistors were mounted on each TM module, one on the DC-DC converter and one on each of the two hybrids. A custom End-of-Substructure (EoS) card is attached to a RaspberryPi and Arduino to power on or off each module.

Thermal testing of barrel staves had a few main goals: to validate Finite Element Analysis

APPENDIX A. INNER TRACKER

(FEA) simulations by testing that all temperature trends are as we expect, to make sure that individual modules do not exhibit abnormal thermal behavior, and finally to check that loaded staves can cope with large changes in temperature they might face during operation. I will highlight a few key results which demonstrate that each of these goals have been accomplished.

Thermal measurements were taken both through the mounted thermistors on each module and through IR imaging. IR imaging provides information about the entirety of the loaded stave, rather than at just a few module positions so provides a more complete picture. The loaded stave was spray-painted black with a high emissivity, low conductivity black paint since silicon is transparent to the IR camera spectrum ($8\text{--}14\ \mu\text{m}$). In order to image the entire stave core, the IR camera was attached to rails above and pulled at a constant speed with an external motor as it recorded a video. The frames were then stitched together into one image. A section of the painted stave is shown in Figure A.6.

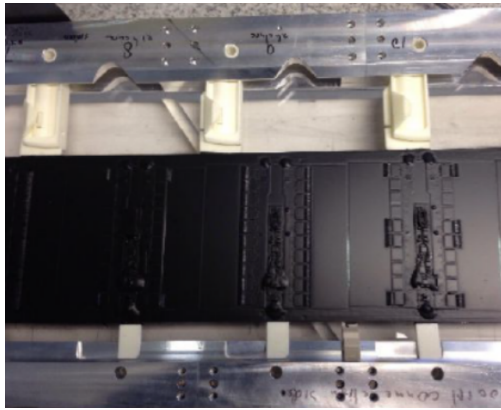


Figure A.6: Portion of the thermo-mechanical stave after being spray-painted for increased emissivity

FEA simulations for the thermal performance of a stave were completed by Prof. Graham Beck at Queen Mary University of London. These calculations quickly became intractable if convection was included so conditions of the stave and coolant were adjusted to minimize

APPENDIX A. INNER TRACKER

convective contributions or make sure that the total electrical power and power absorbed into the coolant were identical. At BNL we adjusted the coolant temperature until we obtained the convective power minimization and then recorded module temperatures under these conditions. These results were compared to the FEA simulations by averaging hybrid temperatures recorded through IR imaging and recording thermistor readings. These comparisons are shown in Figure A.7. The measurements show very good agreement with FEA calculations, within 5% of the expected values.

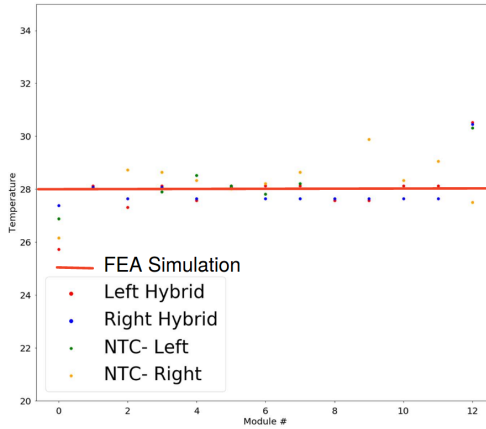


Figure A.7: IR measurements, thermistor measurements, and FEA simulations for the TM stave are compared. Agreement with FEA simulation within 5%.

During module assembly some slight variations were tested, including varying glue thickness below modules, glue curing time, and DC-DC converter types. Modules with and without these variations were compared at varying coolant temperatures and output power settings. Overall, no significant difference in module temperature change was observed for any of these assembly modifications. Stave thermal properties are thus robust to such assembly modifications. Figure A.8 shows a full IR image of the fully loaded stave. It is clear that there are no obvious module-to-module variations in silicon, hybrid, or DC-DC converter temperature. The module sensors increase in temperature as they get closer to the EoS,

APPENDIX A. INNER TRACKER

which is expected since it dissipates power to the stave.

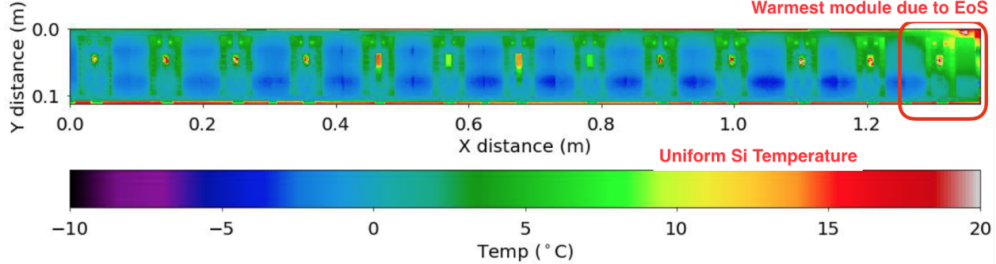


Figure A.8: IR image of fully loaded thermo-mechanical stave

The thermo-mechanical stave was pushed to limits beyond what we would expect loaded staves to encounter during operation and never exhibited unexpected behavior. Thermal cycles, thermal shocks and bend tests showed the loaded stave to be robust against temperature variation and that the carbon fiber core is as stiff as it was prior to loading. Another test was how neighboring modules would perform if one module malfunctioned and was powered off. Figure A.9 (top) shows the temperature of each module when one of them (fourth to the left) is turned off. The rest of the modules continue to operate normally and temperature changes from the unpowered module do not propagate very far. The bottom image in the figure shows the reverse of the stave when a module is powered off (fourth from the right). The temperature effects are greater on the module directly below than those adjacent to, which is expected due to material differences.

My experiences on ATLAS detector upgrades for the HL-LHC provided context for the bulk of my thesis research. This project provided me with in depth and hands-on knowledge of the ATLAS detector and its component parts, as well as the scale of effort required to build new detector components. I have an abiding appreciation for the people and technology necessary for data-taking at the LHC, both of which make measurements like the Higgs cross-section detailed in this thesis possible.

APPENDIX A. INNER TRACKER

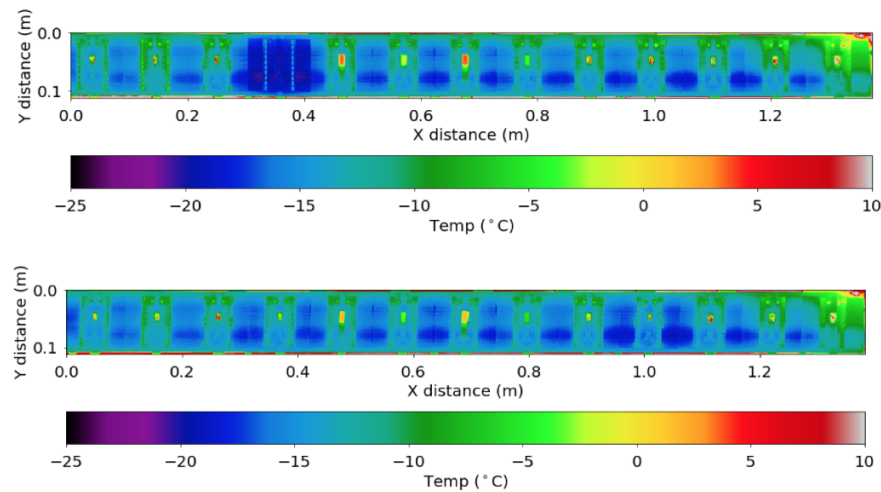


Figure A.9: IR image of fully loaded thermo-mechanical stave